Sede Amministrativa: Università degli Studi di Padova
Dipartimento di Fisica e Astronomia *"G. Galilei"*

Scuola di Dottorato di Ricerca in Fisica
XXVI Ciclo

Search for the Dynamical Dipole in the mass region of ^{192}Pb nucleus in fusion-evaporation and fission heavy-ion reactions at E_{lab} = 11MeV/nucleon

Direttore della Scuola
Ch.mo Prof. Andrea Vitturi

Supervisore
Ch.mo Prof. Cosimo Signorini
Co-Supervisore
Dott.ssa Dimitra Pierroutsakou

Dottorando
Concetta Parascandolo

Abstract

The *Dynamical Dipole* mode is a pre-equilibrium collective dipole oscillation predicted to be excited in charge asymmetric heavy-ion collisions. It decays emitting prompt γ–rays and gives important information on the reaction dynamics. Its study could allow us to probe the density dependence of the symmetry energy in the Equation of State at sub-saturation densities, where this oscillation is active. Furthermore, its prompt radiation could be of interest for the synthesis of super-heavy elements in hot fusion reactions as it cools down the formed nucleus on the fusion path through emission of prompt γ–rays .

We investigated the Dynamical Dipole in fusion-evaporation and fission reactions for a composite system in the mass region of lead, a mass region never studied before. For this research the reactions ^{40}Ca + ^{152}Sm and ^{48}Ca + ^{144}Sm have been performed at E_{LAB} = 11 MeV/nucleon at the Laboratori Nazionali del Sud, (LNS, Italy). The γ–rays and the light charged particles were detected by using the MEDEA apparatus, made of 180 BaF_2 scintillators and 6 Parallel Plates Avalanche Counters for fission fragments and evaporation residues.

Any difference in the γ–ray multiplicity spectra and the γ–ray angular distributions of the two investigated reactions constitutes the signature of a pre-equilibrium process, i.e. the Dynamical Dipole mode excitation and its subsequent γ decay. From the study of these observables in the two reactions it was shown, in a model independent way, that the Dynamical Dipole survives in such a heavy composite system with similar features in both evaporation and fission events. Our results were compared with theoretical calculations performed within a BNV transport model, based on a collective bremsstrahlung analysis of the entrance channel reaction dynamics.

Riassunto

Il *Dipolo Dinamico* è un'oscillazione dipolare collettiva di pre-equilibrio che si instaura in una reazione asimmetrica in carica fra ioni pesanti. Tale oscillazione decade emettendo raggi γ dipolari di pre–equilibrio e può fornire importanti informazioni sulla dinamica delle reazioni. Il Dipolo Dinamico consente di avere informazioni sulla dipendenza dell'equazione di Stato della materia nucleare dalla densità, per densità al di sotto di quella di saturazione, dove questa oscillazione è attiva. Inoltre, la sua emissione "pronta" potrebbe essere utile per la formazione di nuclei superpesanti in processi di fusione "calda", come possibile meccanismo di raffreddamento del sistema composito tramite l'emissione raggi γ di pre–equilibrio.

Il Dipolo Dinamico è stato studiato nella regione di massa del Pb, una regione di massa mai investigata finora, sia in reazioni di fusione–evaporazione che di fissione. A tale scopo sono state realizzate le reazioni ^{40}Ca + ^{152}Sm e ^{48}Ca + ^{144}Sm ad un'energia incidente E_{LAB} = 11 MeV/nucleone presso i Laboratori Nazionali del Sud, (LNS, Italy). I raggi γ e le particelle leggere cariche sono state rivelate usando il setup sperimentale MEDEA, composto da 180 scintillatori BaF_2 e 6 rivelatori *Parallel Plates Avalanche Counters* per i frammenti di fissione e i residui di evaporazione.

Le differenze negli spettri di molteplicità γ e nelle distribuzioni angolari dei raggi γ delle due reazioni studiate indicano la presenza di un processo di pre-equilibrio, ovvero del Dipolo Dinamico e del suo conseguente decadimento tramite raggi γ. Dal confronto di queste osservabili nelle due reazioni è stato dimostrato, in maniera indipendente dai modelli, che il Dipolo Dinamico sopravvive in un sistema composto così pesante con caratteristiche simili sia in eventi di evaporazione che di fissione. Tali risultati sono stati confrontati con calcoli teorici effettuati nell'ambito di un modello di trasporto di tipo

BNV, basato su un approccio di emissione bremsstrahlung collettivo della dinamica di reazione del canale d'ingresso.

Contents

Introduction

The atomic nucleus is a complicated quantum system with many degrees of freedom, where different excitation modes can develop, such as the collective ones involving the majority of the nucleons.

A well-known result of nuclear physics is the possibility to excite a giant resonance in nuclei. A giant resonance is a highly collective nuclear excitation of small amplitude and high frequency ($\sim 10^{21}$ Hz). Among all possible modes of collective excitation, the Giant Dipole Resonance (GDR) was the first to be observed experimentally. The GDR can be described macroscopically as a highly collective oscillation of all protons against all neutrons of the atomic nucleus with a dipole spatial pattern.

The GDR can be excited by using electromagnetic fields associated to photons or produced by fast charged particles. It is also possible to excite the GDR in heavy-ions fusion reactions, as demonstrated experimentally from many studies (see for instance [1, 2]). In this case the γ decay spectrum of the compound nucleus is dominated by the dipole γ–rays coming from the GDR, in an energetic region between ∼8 and ∼20 MeV.

Many experimental results demonstrated that the GDR is a useful tool to probe the bulk properties of the nuclei of the ground state as well as at finite temperature. The γ–ray emission following the GDR decay is sufficiently fast to compete with other decay modes with a sizable branching ratio and therefore to probe the characteristics of the nuclear system prevailing at that time. In fact the GDR couples to the nuclear states of the compound nucleus in a very short time ($\sim 10^{-22}$ s), lower than the half-life of the compound nucleus itself ($\sim 10^{-18}$ s at a temperature T = 1 MeV and $\sim 10^{-21}$ s at T = 3 MeV).

Therefore the dipole emission can provide information on the first stages of the nuclear decay, like the nuclear deformations and fluctuations and the evolution of the shape induced by temperature and spin [3]. On the other hand, it is possible to perform a study of the resonance with increasing excitation energy of the nuclei, in order to probe its existence and its properties in extreme conditions.

It has been proposed in [4–13] the possibility that pre-equilibrium dipole *strength* can be excited during the charge equilibration in dissipative heavy-ion collisions between interacting ions with a very different N/Z ratio, with N (Z) being the neutrons (protons) number. This out of phase collective oscillation of protons against neutrons of the system, called *pre–equilibrium* GDR or *Dynamical Dipole* (DD) mode, can be excited if there is a non-vanishing dipole moment between the colliding ions and develops along the symmetry axis of a deformed system, the *dinucleus*. It decays giving rise to a prompt radiation, the so-called *pre–equilibrium* dipole γ–ray emission, that appears as an extra strength in the energy region of the statistical γ–rays coming from the excitation of the statistical GDR in the compound nucleus.

The first experimental evidences for the existence of the DD mode were obtained in heavy-ion deep-inelastic collisions [14–16, 19, 20, 23] and in heavy-ion fusion reactions [21–26]. In the latter case, the DD was studied in a model independent way: by probing the same compound nucleus at identical conditions of excitation energy and angular momentum from two entrance channels having different charge asymmetry. The comparison of the associated γ–ray spectra evidenced an extra yield in the compound nucleus GDR energy region for the charge asymmetric reaction that was related to the predicted DD decay.

From the theoretical studies performed during the last years, the DD γ yield is expected to have a centroid energy lower than that of a GDR in a spherical nucleus of similar mass because of the large deformation of the dinuclear system at the emission moment and a corresponding anisotropic angular distribution pattern. Furthermore, a dependence of its intensity on the beam energy was foreseen in [9, 27], with a maximum value in an energy region situated between the low incident energies near the Coulomb barrier and the higher ones near the Fermi energy domain, namely between 8 and 14 MeV/nucleon.

At the moment very few data exist on the DD absolute γ yield and on its angular distribution that can be directly compared with theoretical calculations. Furthermore, calculations are not able to simultaneously reproduce all the existing experimental findings, like the DD yield evolution with the beam energy [25, 26] or to reproduce with the same nucleon-nucleon cross section the DD γ yield obtained at the same incident energy in [25, 26] and in [28] where the same compound nucleus was formed employing different entrance channels. It is clear thus, that more experiments should be performed, to shed light on the interplay of the different reaction parameters on the DD features and to provide severe constraints to the theoretical models.

The study of the pre–equilibrium dipole emission is interesting because it can provide valuable information on the charge equilibration mechanism of the compound nucleus before reaching the thermal equilibrium. Moreover, the DD prompt radiation can probe the density dependence of the symmetry energy in the nuclear matter Equation of State at sub-saturation densities, which is acting as a restoring force for the oscillation developed in the dilute dinuclear system [29].

Another aspect that can be addressed by taking advantage of the DD γ decay is to investigate whether this kind of pre-equilibrium mechanism can represent an efficient cooling mechanism of the composite system in the fusion path, to facilitate the super-heavy element (SHE) formation. In fact, we know that the composite system survival probability against fission and the shell structure stabilization effects increase by decreasing the composite system excitation energy. However, it is predicted in [7] that the DD yield should decrease in collisions involving heavy mass partners due to the fact that the reactions with small nuclei are less damped than those involving more nucleons. Therefore, the existence of the DD in heavier systems than those studied previously was necessary as a first step.

In this framework, the ^{40}Ca + ^{152}Sm and ^{48}Ca + ^{144}Sm reactions were studied at an incident energy of 440 and 485 MeV, respectively, by using the previously described, difference technique. The two entrance channels, that have a similar mass but a different charge asymmetry, lead to the formation of the same compound system, ^{192}Pb , at the same excitation energy E* and and with identical spin distribution. The observation of any difference in the dipole γ emission between the two reactions can be safely related to the different entrance channel charge asymmetry and thus, it can be ascribed to the DD excitation and subsequent decay. In the same experiment both fusion-evaporation and fission events were studied for the first time. The aim of this study was twofold: 1) to verify the existence of the Dynamical Dipole in a mass region never investigated before adding information on the scarce body of existing data and giving more constraints to the theoretical models; 2) to shed light on the opportunity to use its prompt γ radiation to cool down the composite system on the way to fusion, favoring the formation of super-heavy elements.

This thesis presents the data analysis of this experiment and it is organised as explained in the following. In **Chapter 1** a brief overview of the main studies on the GDR and its features, for both the ground state and the excited states, are presented. Experimental evidences and theoretical studies, performed during the last years, are shown. In the same chapter it is introduced the subject of the thesis, the dynamical dipole mode, drawing the state of the art of the related studies.

As mentioned before, our observables are the energy spectra and the angular distribution of the γ–rays , emitted in fusion–evaporation and fission events. The reaction channel was selected by detecting the γ–rays in coincidence with the specific reaction products (evaporation residues or fission fragments). The chosen detectors for particles and radiation are described in **Chapter2**.

The experimental details are reported in **Chapter 3**: the experimental setup, the electronics and the trigger scheme. Moreover, it is explained the technique used to discriminate and identify particles and radiation detected during the measurement. All the collected data are suitably reduced, as explained in detail in section **Chapter 3**, in order to obtain the γ–ray multiplicity spectra and angular distribution for fusion–evaporation (**Chapter 4**) in the two reactions.

For fission events, as explained in **Chapter 5**, we are able to reconstruct the mass of the fission fragments and then we can obtain the γ–ray multiplicity spectra for a certain mass partition.

In **Chapter 6**, the data obtained for our system are compared to those found in a different mass region [25,26]. Furthermore, the experimental results are compared with theoretical calculations performed in the framework of *Boltzmann-Nordheim-Vlasov* transport model [9,27]. Finally the conclusions and the future perspectives are drawn.

Chapter 1

The physics case

1.1 Giant Dipole Resonance

The Giant Resonance (GR) is a highly collective nuclear excitation of small amplitude and high frequency ($\sim 10^{21}$ Hz) induced by the interactions between nuclei and an external perturbation, due to, for example, electromagnetic fields.

There are different types of giant resonances, classified according to the multipolarity, the spin S and the isospin T quantum numbers. The multipolarity is defined as 2^L, where $\vec{L}$ is the angular momentum of the emitted γ.

The emission of multipole radiation, however, is related to the selection rules that take into account the conservation of parity and angular momentum.

Let us consider a nucleus in an excited resonant state of total angular momentum $\vec{J}_i$, parity π_i and z component of the angular momentum M$_i$, decaying through γ–rays to a final state characterized by a total angular momentum $\vec{J}_f$, parity π_f and z component of the angular momentum M$_f$. From the conservation laws it follows:

$$|J_i - J_f| \leq L \leq J_i + J_f \qquad M_i = M_f + m \tag{1.1}$$

$$\pi = \pi_i \cdot \pi_f$$

Denoted by ΔS the variation of Spin from the initial state to the final one, the parity of the emitted radiation is equal to $\pi = (-1)^{L+\Delta S}$. Fixed the multipolarity, the transition is defined electric in case of ΔS = 0 and magnetic when ΔS = 1.

In the isospin formalism the distinction between nucleons is done according to the eigenvalue of the t_3 component of the isospin operator $\vec{t}$, assuming the following values $t_3 = -\frac{1}{2}$ for protons and $t_3 = +\frac{1}{2}$ for neutrons. In a nucleus consisting of Z protons and N neutrons, the total isospin operator $\vec{T} = \sum_{i=1}^{A} \vec{t}_i$, projected along the quantization axis, has eigenvalue $T_3 = \frac{N-Z}{2}$. The collective motions in which neutrons and protons move in phase are referred as isoscalar resonances (ΔT = 0), while those in which neutrons move against protons are called isovector resonances (ΔT = 1).

The giant dipole resonance (GDR) is defined as a collective motion with $L^{\pi} = 1^{-}$, pure isovector (ΔT = 1) and electric (ΔS = 0). In a macroscopic view, the GDR can be described as a collective oscillation of protons against neutrons in a dipole spatial configuration.

The first experimental evidence of GR appears in the work of *Bothe and Gentner* [30] in 1937, bombarding different targets with 17.6 MeV photons, produced in the ^{7}Li(p,γ) reaction. It was noticed an unexpected increase in the γ capture probability in some reactions. About ten years later *Baldwin and Klaiber* [31] confirmed the existence of the GDR in photoabsorption reactions. The photoabsorption cross section, in photo-fission measurements of uranium and thorium, around 15 MeV had a resonant behaviour, similar to that shown in figure 1.1.

The first theoretical treatment of the GDR was presented in 1948 with a macroscopic hydrodynamic model where the nucleus is treated as a two-components drop of ideal fluid. In the description of *Steinwedel - Jensen* [32] the total density of the nucleus is fixed and the external surface remains unchanged, while neutrons and protons are compressible fluids which oscillate in opposite phase within the nucleus. In this case, the restoring force is proportional to the volume coefficient of the relative term in the nuclear mass formula of *Bethe – Weizsacker* [33] and the energy of the oscillation varies as $A^{-1/3}$; in the version proposed by *Goldhaber – Teller* [34] neutron

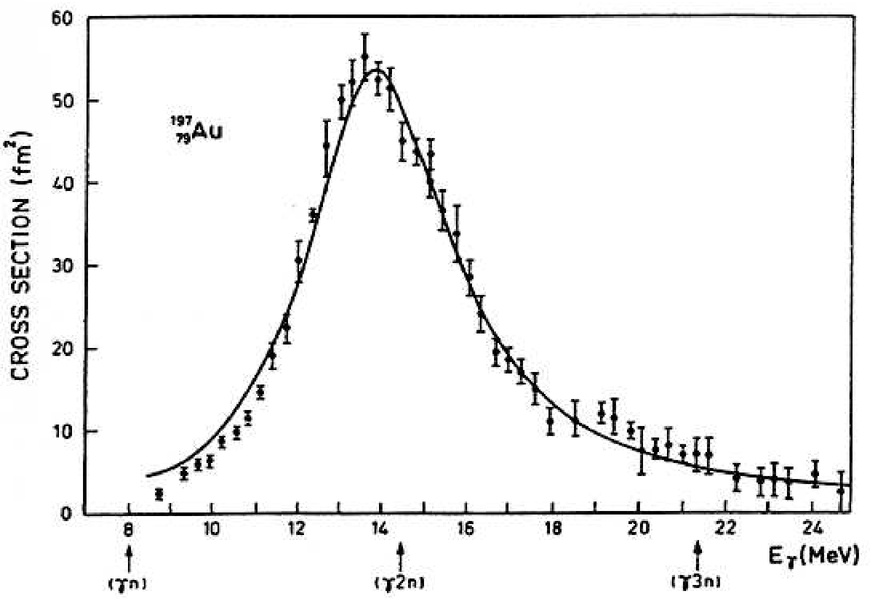

Figure 1.1: *Photoabsorption cross section for* ^{197}Au *nucleus.*

and proton fluids behave as two interpenetrating hard spheres in an out of phase oscillation causing a deformation of the nucleus. In this case the restoring force is proportional to the surface coefficient of the nuclear mass and the energy of the oscillation varies as $A^{-1/6}$. In figure 1.2 it is shown a schematic view of the models, mentioned above.

The evolution of the energy of the resonance as a function of mass number could not be explained exactly with any of the proposed models. Then a theoretical description [35] was developed treating the GDR as a superposition of the two above-mentioned mechanisms, which reproduces well the experimental data through an intermediate dependence of the resonance energy on the nuclear mass A in the following way:

$$E_{GDR} = 31.2 \cdot A^{-1/3} + 20.6 \cdot A^{-1/6} \quad (MeV) \tag{1.2}$$

From a microscopic point of view the GDR is a coherent superposition of 1p–1h (1 particle – 1 hole) excitations [33]. In the shell model the separation

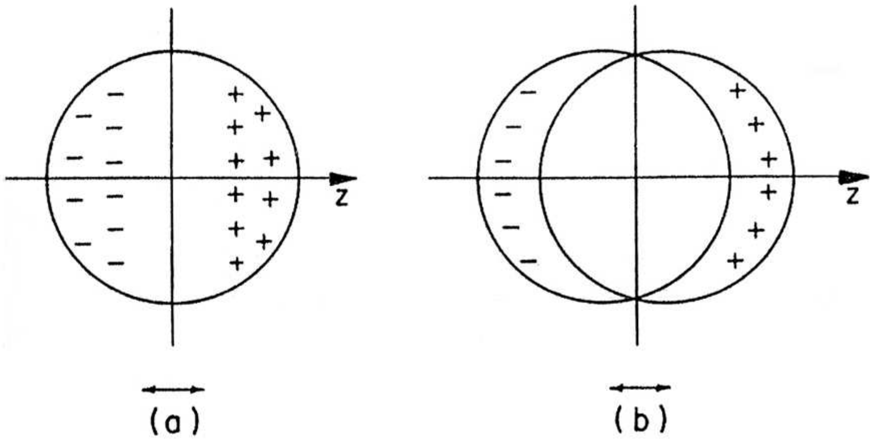

Figure 1.2: *Schematic representation of dipole oscillation in a nucleus, according to the Steinwedel – Jensen model (a) and Goldhaber – Teller one (b).*

between two adjacent major shells is equal to $1\hbar\omega$ and therefore we would expect to observe the GDR to an energy equal to $1\hbar\omega \sim 41 \cdot A^{-1/3}$ MeV. This expression is derived from the modified harmonic oscillator potential, which was introduced to describe the nucleon–nucleon potential [36]. However, due to the repulsive nature of the residual interaction between particles and holes in an isovector excitation, the GDR was found at an energy equal to $\sim 80 \cdot A^{-1/3}$ MeV for heavy and intermediate mass nuclei.

1.1.1 Features of the GDR

The GDR is characterized by the following features:

1. Frequency ω_{GDR};
2. Width Γ_{GDR};
3. Strength function S_{GDR}.

In order to better understand the behaviour of these parameters, they are described more in detail in the following.

Frequency, ω_{GDR}

An estimation of the energy ($E_{GDR} = \hbar\omega_{GDR}$) [37], and thus of the oscillation frequency of the GDR, can be obtained starting from the fundamental hypothesis that the electric field (associated to the radiation) that excites the nucleus is approximately uniform over the entire nuclear volume. This is confirmed by the fact that the wavelength of the radiation λ is one or two orders of magnitude larger than the nuclear radius R as shown in the expression below, where the typical energies E_γ are equal to few MeV:

$$\frac{\lambda}{R} = \frac{2\pi \cdot \frac{\hbar c}{E_\gamma}}{1.2 \cdot A^{1/3}} \approx 10 \div 200 \tag{1.3}$$

With this assumption, then, taking into account the fact that the restoring force of the nuclear vibration is proportional to the symmetry coefficient of the nuclear mass formula, is:

$$E_{GDR} = \hbar\,\omega_{GDR} = \sqrt{\frac{3\,\hbar^2\,b_{sym}}{m\,\langle r^2\rangle}} \cong 80\,A^{-1/3} MeV \tag{1.4}$$

where $\langle r^2\rangle = \frac{\int r^2\,\rho(r) d^3r}{\int \rho\,(r) d^3r} = \frac{3}{5}\,R^2$ and m is the nucleon mass.

From (1.4) it follows that the oscillation frequency of the resonance ω_{GDR} is inversely proportional to the length of the oscillation axis. This information allows not only to estimate the linear dimensions of the nucleus along the electric field vector, but also to determine its shape.

In nuclei characterized by a static deformation there are three axes of vibration and therefore the photoabsorption cross section is divided into three components: the lower frequency component corresponds to an oscillation along the major axis of the nucleus. To describe the deformation of a nucleus not very far from spherical symmetry, in general, a parametrization in spherical coordinates is used:

$$R(\theta, \phi) = R_0 \left\{ 1 + a_{00} + \sum_{\lambda=1}^{\infty} \sum_{\mu=-\lambda}^{\lambda} a^*_{\lambda\mu} Y_{\lambda\mu}(\theta\;\phi) \right\} \tag{1.5}$$

where R_0 is the radius of a spherical nucleus with similar mass.

If $\lambda = 2$, the deformation is quadrupolar and only two of the five parameters $a_{2\mu}$ are independent. According to the notation:

$$a_{20} = \beta\, cos\gamma \tag{1.6}$$

$$a_{22} = \frac{1}{\sqrt{2}}\, \beta\, sin\gamma \tag{1.7}$$

it is possible to describe all nuclear shapes through two polar coordinates and its orientation through the Euler angles, where β describes the nuclear deformation, and γ can vary from 0 to 2π. From the liquid drop model, it follows that the frequency of the dipole oscillation along each nuclear axis can be derived by:

$$\omega_k(\beta,\gamma) = \omega_{GDR} \cdot exp\left[-\sqrt{\frac{5}{4\pi}}\,\beta\, cos\left(\gamma - \frac{2\pi k}{3}\right)\right] \qquad k = 1,2,3 \tag{1.8}$$

where ω_{GDR} is the GDR frequency for a spherical shape [38].

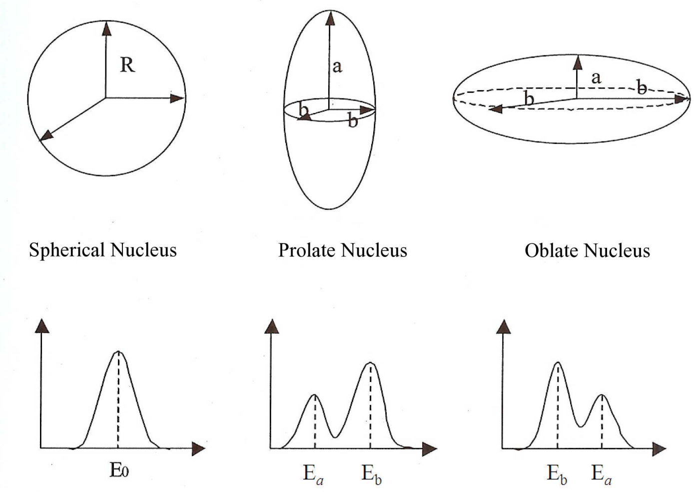

Figure 1.3: *Schematic representation of the relationship between the photoabsorption cross section and the nuclear shape.*

In case of an axial symmetry deformation, the three components of the photoabsorption cross section are reduced to two, since two of them are degenerate. From the relative intensity of the two components the shape of the nucleus (see figure 1.3) can be determined, and then the deformation parameter.

For a prolate shape, indeed, the low energy component E_a, associated with oscillation along the major axis of the ellipsoid, corresponds to about a third of the cross section, while the high energy component E_b corresponds to the remaining two-third, since it is twice degenerate. The situation is reversed in the case of an oblate shape.

An exact calculation [39] shows that the ratio between the energies corresponding to oscillations along the a and b axes is deduced, in good approximation, from the following relationship:

$$\frac{E_b}{E_a} = 0.911\,\frac{a}{b} + 0.089 \tag{1.9}$$

where:

$$\frac{a}{b} \approx \frac{3}{2}\left(\frac{4\pi}{5}\right)^{-\frac{1}{2}}\beta \tag{1.10}$$

The fact that the photoabsorption cross section is divided into more components in the case of a GDR excited in a deformed nucleus provides evidence of the coupling of the GDR to the deformations of the nuclear surface.

Width, Γ_{GDR}

The total width of a GDR, Γ_{GDR}, can be decomposed into the sum of four contributes [1] that take into account the different mechanisms that can lead to the damping of the resonance:

$$\Gamma_{GDR} = \Gamma^{\uparrow} + \Gamma_{\downarrow} + \Gamma_{Landau} + \Gamma_{\gamma}. \tag{1.11}$$

Let us describe their properties:

- $\Gamma^{\uparrow}$: the *escaping width* is associated to the decay of the resonance through light particles emission. This mechanism is due to the fact that the energy of the resonance is greater than the average nucleon separation energy. In light nuclei the $\Gamma^{\uparrow}$ is the dominant contribution to the total width, since the direct processes are the most probable. The energy of such emitted particles is high and their energy distribution is different from that of evaporated particles. In heavy nuclei $\Gamma^{\uparrow}$ is of the order of 100 keV.

- $\Gamma^{\downarrow}$: the *spreading width* is related to the time necessary to rearrange the energy and the angular momentum of the GDR among all nucleons. This width takes into account the nuclear "thermalization" process, i.e. the process in which the GDR decays into a chaotic state typical of a high–temperature nucleus, favoring the emission of low energy particles. In heavy nuclei the $\Gamma^{\downarrow}$ is more than 80% of the total width and is of the order of some MeV.

- Γ_{γ} is related to the lifetime of the resonance with respect to the dipole photon emission. For both heavy nuclei than light ones its value is of the keV order.

- Γ_{Landau}: this component has been observed experimentally only in nuclei with $A \leq 60$ [40] and it seems that they do not contribute significantly in heavier nuclei. It is due to the coupling of the collective motion to the single particle motion and thus to the fragmentation of the dipole strength into 1p–1h excitations due to the shell effects. This phenomenon is known as *Landau damping*, since explained by Landau [41] for the damping of sound waves in infinite quantum fluid systems. Its contribution to the total width is around 100 keV.

The Γ_{GDR} is strongly influenced by the shell structure of nuclei: for magic nuclei, typical values are of the order of 4÷5 MeV; in case of nuclei with not completely closed shells, the total width of the GDR can reach values around 8 MeV [42]. In deformed nuclei the width of each component can be calculated as described in [43, 44]

$$\Gamma_i = \Gamma_0 \left(\frac{E_i}{E_0} \right)^{\delta} \tag{1.12}$$

where $\delta \sim 1.8$ and Γ_0 and E_0 are the width and the centroid of a GDR excited on a spherical nucleus of the same mass.

In heavy nuclei the GDR width is dominated by the *spreading width.* For these nuclei, experimentally it was observed that the GDR is damped mostly by the emission of low-energy neutrons [45]. The percentage of Γ_γ to the total GDR width is about $\frac{\Gamma_\gamma}{\Gamma_{GDR}} \approx \frac{\Gamma_\gamma}{\Gamma^{\downarrow}} \approx 10^{-4} - 10^{-5}$.

Strength function, S_{GDR}

The total strength of the GDR is defined as the experimental photoabsorption cross section integrated in the energy range between 0 and 30 MeV:

$$S_{GDR} \equiv \sigma_{tot} = \int\limits_{0}^{30MeV} \sigma_{abs}^{exp}\left(E_\gamma\right) dE_\gamma \tag{1.13}$$

The dipole strength is of fundamental importance in the study of the resonances. In fact, it allows to estimate the degree of collettivity of the excitation, namely the percentage of nucleons participating in the oscillation, when compared to its theoretical upper limit given by the *Thomas - Reiche - Kuhn* (TRK) sum rule [33]:

$$\int\limits_{0}^{30MeV} \sigma_{abs}\left(E_\gamma\right) dE_\gamma = 60\,\frac{NZ}{A} \quad (MeV \cdot mb) \tag{1.14}$$

This sum rule is model independent and is expressed in terms that reflect the general properties of the nuclei, neglecting the exchange terms and the velocity ones. In order to deduce the TRK sum rule, it should be noted that the cross section for the excitation of a nucleus from an initial state $|0\rangle$ to a final state $|\nu\rangle$ after the absorption of a dipole photon with energy E_γ is given by [46]

$$\sigma_\nu(E_\gamma) = \frac{4\pi^2 e^2}{\hbar c}\left(E_\nu - E_0\right)\,\left|\langle\nu\left|D\right|0\rangle\right|^2\,\delta(E_\gamma - E_\nu + E_0) \tag{1.15}$$

where E_0 and E_ν are the energies of the initial and final states, respectively. The operator D is the dipole operator for the E1 radiation along the z axis and is given by the relation [46]

$$D = \frac{NZ}{A}\left(\frac{1}{Z}\sum_{p=1}^{Z}\vec{z}_p - \frac{1}{N}\sum_{n=1}^{N}\vec{z}_n\right) = \frac{NZ}{A}\left(\vec{R}_Z - \vec{R}_N\right) \tag{1.16}$$

where $\vec{z}_p$ ($\vec{z}_n$) is the position vector of each proton (neutron) and $\vec{R}_Z$ ($\vec{R}_N$) is the position vector of the center-of-mass of protons (neutrons). The operator E1 is defined as:

$$E1 = \sqrt{\frac{3}{4\pi}}\, e \sum_{i=1}^{Z} \vec{r}_i \tag{1.17}$$

and excites only the protons ($\vec{r}_i$ denotes the position of proton i). However, in the center-of-mass reference frame the total linear momentum is zero, therefore the effective motion of a proton is $\vec{r}_i - \vec{R}$, where $\vec{R}$ is the position vector of the center-of-mass, $t^{(i)}{}_3$ is the third component of isospin of nucleon i and then we can write:

$$\sqrt{\frac{4\pi}{3}}\, E1 = e\, D = \sum_{i=1}^{Z}(\vec{r}_i - \vec{R}) = -e\sum_{i=1}^{A} t_3^{(i)}\,(\vec{r}_i - \vec{R}) = e\,\frac{NZ}{A}\left(\vec{R}_Z - \vec{R}_N\right). \tag{1.18}$$

The operator D is equivalent to E1, but with an effective charge equal to $\frac{eN}{A}$ for each proton and $-\frac{eZ}{A}$ for each neutron [46].

Integrating the equation (1.15) over E_γ and summing over all final states $|\nu\rangle$, we obtain the total photoabsorption cross section:

$$\sigma_{tot} = \sum_{\nu}\int_{0}^{\infty}\sigma_\nu(E_\gamma)dE_\gamma = \frac{4\pi^2 e^2}{\hbar c}\sum_{\nu}(E_\nu - E_0)\,\left|\langle\nu\,|D|\,0\rangle\right|^2 \tag{1.19}$$

and hence the TRK sum rule is obtained (1.14). In the case of a spherical nucleus, the photoabsorption cross section σ_{abs} can be described, with the exception of very light nuclei, by a Lorentzian function with a centroid energy E_{GDR} and a total width Γ_{GDR}:

$$\sigma_{abs}\left(E_{\gamma}\right) = \sigma_0 \, \frac{E_{\gamma}^2 \, \Gamma_{GDR}^2}{(E_{\gamma}^2 - E_{GDR}^2)^2 + E_{\gamma}^2 \, \Gamma_{GDR}^2} \tag{1.20}$$

with σ_0 equal to the maximum value of the distribution observed for $E_{\gamma} = E_{GDR}$.

The TRK sum rule is obtained in a description of the nucleus interacting with an impulsive electric field in the case in which all the nucleons participate collectively.

The degree of collectivity of the resonance can be expressed through an index *I*, defined as follows:

$$I \equiv \frac{\int_{0}^{30MeV} \sigma_{abs}^{exp}\left(E_{\gamma}\right) dE_{\gamma}}{\int_{0}^{30MeV} \sigma_{abs}\left(E_{\gamma}\right) dE_{\gamma}} = \frac{S}{60\frac{NZ}{A}} \tag{1.21}$$

namely, expressing the integrated cross section in unit of $60\frac{NZ}{A}$ $(MeV \cdot mb)$.

Experimentally, by detecting neutrons emitted by a nucleus after absorbing a photon, it has been observed that for nuclei of mass A $\leq$ 80 the GDR does not exhaust the 100% of the sum rule if the integration is carried out up to 30 MeV. This result can be explained observing that in this measurement some processes have been neglected, because of the integration limit, like the effect of quasi – deuteron (a high-energy γ–ray absorbed by a correlated pair neutron – proton) and the $T=T_0+1$ transition, where T_0 and T are, respectively, the isospin of the initial and final states. Moreover, a part of the GDR strength is lost since protons have not been detected in these measurements and because the considered integration limit is too low for light nuclei where the GDR is fragmented and its centroid energy is situated at relatively large energies.

As the mass and charge of the nuclei increase, the increase of the Coulomb barrier inhibits the proton emission while the GDR centroid energy moves toward lower energies; for nuclei of mass around 100, indeed, the GDR fulfills 100% of the TRK sum rule. For heavier nuclei, the experimental data exceed

(1.14) of $\sim$ 30% the TRK sum rule, since the exchange terms have been neglected.

1.2 GDR built on excited states

In the early '60s [47, 48], it was suggested that the GDR can be built on all nuclear levels without a change of the energy dependence of its cross section.

The first experimental observation in favor of this idea was obtained in 1974, studying the γ spectrum from the spontaneous fission of ^{252}Cf [49]. The observed increase in the γ spectrum above 10 MeV was not immediately understood, but then it was correctly attributed to the excitation of a GDR built on the excited states of the nucleus. In 1981 another experiment [50] confirmed the existence of GDR built on the continuum states, observing the γ–rays emitted in the decay of compound nuclei formed in fusion reactions induced by heavy ions (^{40}Ar on ^{82}Se, ^{110}Pd and ^{124}Sn targets).

The decay of the compound nucleus (CN) through particle evaporation and γ–ray emission can be represented in the excitation energy (E^*) vs Angular Momentum (J) plane (fig.1.4) which is divided into two parts by the Yrast line representing the minimum energy of a nucleus with a given spin. On Yrast line the excitation energy of the nucleus is purely rotational. The γ transitions of energy less than 2 MeV take away a large amount of angular momentum from the nucleus; they are of electric quadrupole type (E2, L = 2) or magnetic dipole (M1, S = 1) one. These transitions occur almost parallel to the Yrast line at the end of the nucleus decay cascade. L = 2 transitions can also have a collective character in the case of deformed nuclei in their ground state (rotational bands).

The region extending up to energies of the order of $\sim$8 MeV corresponds to electric dipole transitions (E1, L = 1), just below the energy threshold for particle emission. These transitions are responsible for the exponential form of the γ spectrum and take away few units of angular momentum. The energy transitions greater than 8 MeV are due to dipole photons, produced from the GDR decay. This contribution, as mentioned in paragraph 1.1.1, has a Lorentzian evolution (1.20), and it is predominant in the energy re-

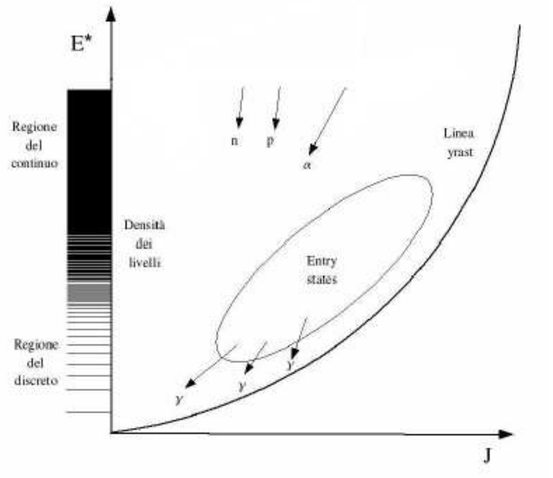

Figure 1.4: *Excitation Energy (E*) vs Angular Momentum (J).*

gion between 8 and ∼20 MeV. According to the statistical model predictions at high excitation energy, the nucleus decays mainly through particle emission, which carries away an average energy of 12 MeV, few units of angular momentum if the particle is a neutron and more angular momentum units if it is an α particle. The probability for the nucleus to decay through γ emission instead of particle emission increases by increasing the excitation energy. That means that the nucleus has a high probability to emit γ rays at the first step of the decay, before any particle emission. To give an idea of the relative probability to decay by γ emission in the first step, we remind that the ratio Γ_γ over Γ_{tot} is of the order of 10^{-4}. The energy transitions greater than ∼25-30 MeV originate from the interactions between nucleons, belonging to the projectile and to the target, in the early stages of the reaction (nucleon – nucleon Bremsstrahlung). This contribution presents an exponential behaviour.

1.2.1 Evolution of the GDR features as a function of excitation energy

Let us consider briefly how the GDR features vary as a function of the excitation energy.

$\underline{\mathrm{E}_{GDR}}$

Several theoretical calculations [51–54] predicted that the energy of the resonance, E_{GDR}, is only weakly dependent on the excitation energy; indeed its value at a temperature T = 3 MeV nuclear is about 4-6 % less than that for the ground state. The experimental results ([55] and internal references) confirmed these theoretical predictions although the experimental errors are often large, of the order of 0.5 or 1 MeV.

$\underline{\Gamma_{GDR}}$

A considerable variation in the GDR width, Γ_{GDR}, was observed for the first time by studying the γ spectra of $^{108}\mathrm{Sn}^*$ decay, populated up to an excitation energy $\mathrm{E}^* = 60$ MeV and angular momentum J$\sim 40\hbar$ [56]. Thanks to the reproduction of the data with the computer code CASCADE [57], it was found an increase of Γ_{GDR} with increasing excitation energy. Several systematic studies following [55, 58–60] led to the same observations.

However, there are two different theoretical ideas on the reason of of the observed enlargement of the GDR width Γ_{GDR}. On one side, the increase of the Γ_{GDR} with the excitation energy is attributed to the effect of the deformation caused by the high angular momentum and by the thermal fluctuations of the nuclear shape [61–64]. This hypothesis is in agreement with the theoretical calculations [65] asserting that the break of the correlations between particles at high excitation energy and high angular momentum causes a transition to an oblate shape. On the other side, this increase is attributed to a higher damping of the resonance at high excitation energies [66, 67], namely a strong increase in the *spreading width* $\Gamma^{\downarrow}$ with the nuclear temperature. This effect is due to two-body collisions, becoming more and more important with increasing temperature, due to the suppression of the Pauli blocking.

Currently there are several experimental observations [59, 60, 68–70] that confirm the first hypothesis about the reasons of the GDR enlargement and the GDR width behaviour can be described reasonably well within the Thermal Shape Fluctuation Model (TSFM) [71].

$\underline{\mathrm{S}_{GDR}}$

The first work aimed to investigate the persistence of collective motion at high excitation energy, i.e. above 300 MeV, was done by studying the reaction ^{40}Ar + ^{70}Ge [72]. The data obtained from the analysis showed the disappearance of the GDR at these excitation energies, in contrast with what predicted by the statistical model. Subsequently, other experiments observed that the γ decay of the GDR decay was suppressed, resulting in a saturation of the corresponding dipole strength [69, 72–75].

From the theoretical point of view, there are two different approaches to explain this unexpected behaviour with respect to predictions of the statistical model: a suppression of the GDR at high excitation energy [63, 76] or a rapid increase of the width with the excitation energy of the nucleus due to an increase in the *spreading width* [66,67] or/and the fact that it is necessary to include in the Γ_{GDR} also the evaporation width of the CN, that increases with increasing excitation energy [77].

In the first case we have to consider the equilibration time of the GDR on the states of the CN and the existence of a critical value of the excitation energy E$_c$. For energies higher than E$_c$ the CN begins to decay through particle evaporation, before the GDR can reach the equilibrium upon the CN states; in this case the dipole photons are emitted from a colder nucleus.

When the excitation energy reaches its critical value, E$_c$, $\Gamma^{\downarrow} \sim \Gamma_v$ [63], where Γ_v is the width relative to particle evaporation.

At E* ∼250 MeV, the evaporation width is ∼5 MeV and the $\Gamma^{\downarrow}$ of a GDR excited on the ground state of a nucleus is ∼4.5 MeV; hence we can conclude that, according to this hypothesis, the $\Gamma^{\downarrow}$ is essentially independent of the excitation energy.

In the second case it is predicted a strong increase of the $\Gamma^{\downarrow}$ with the excitation energy due to the damping through two-body collisions. The disappearance of the GDR above a critical excitation energy would be, therefore, due to a great enlargement of the GDR itself.

According to what said before on the evolution of $\Gamma^{\downarrow}$ with the temperature, we can conclude that the saturation of the GDR at high excitation energies should be related to the first hypothesis.

1.3 Angular distributions

The measurement of the angular distribution of the GDR photons provide a complementary method for studying the GDR in hot nuclei that have an alignment due to rotation. The angular distribution in the center-of-mass reference frame for statistical emission of high-energy γ rays is expected to be nearly isotropic as a result of averaging over final state spin. An exception to the above statement however occurs if the system possesses a definite deformation, in which case one expects anisotropies that depend on the sense of the deformation (prolate or oblate) and on the orientation of the deformed shape with respect to the rotational axis (see [1, 2] for more details).

The angular distribution of the emitted photons can be expressed as:

$$M_\gamma(E_\gamma, \theta) = M_0[1 + a_2(E_\gamma)P_2(cos(\theta)] \tag{1.22}$$

where P_2 is a Legendre polynomial in the polar angle θ between the direction of the emitted γ–rays and the beam axis and $a_2(E_\gamma)$ is the anisotropy coefficient. The $a_2(E_\gamma)$ coefficients are sensitive both to the magnitude of the deformation and to the shape and orientation of the density distribution.

For example, in a prolate nucleus rotating collectively, the direction of the total angular momentum, J, is perpendicular to the nuclear symmetry axis. The angular momentum associated with the low energy GDR component, corresponding to a vibration along the symmetry axis, is therefore parallel to J and couples to J. The associated transition corresponds to $\Delta \mathrm{J} = \pm 1$ (stretched transitions). The two degenerate high energy GDR components, associated with vibrations along the short axes, that are parallel and perpendicular to J, correspond therefore to a mixture of $\Delta \mathrm{J} = 0$ (unstretched transitions) and $\Delta \mathrm{J} = \pm 1$. The angular distribution of these components in the laboratory reference frame has $a_{2,low}$ = -0.25 and $a_{2,high}$ = +0.125. For oblate collective rotation, where J is perpendicular to the nuclear symmetry axis as in the prolate case, the situation is just reversed: $a_{2,low}$ = +0.125 and $a_{2,high}$ = -0.25. Fynally in the case of an oblate nucleus rotating non-collectively, the rotation is along the symmetry axis. The two longer axes give rise to the two degenerate components at lower energy, both with ΔJ = ±1, while the shorter symmetry axis, parallel to J, corresponds to an unstretched transition, ΔJ = 0. Hence, in the latter case, $a_{2,low}$ = -0.25 and $a_{2,high}$ = +0.50. However, the amplitude of a_2 can be attenuated, due to: 1) the overlap of the split GDR components due to their finite width 2) the required averaging at finite temperature over K values, K being the projection of the angular momentum along the symmetry axis and 3) rotational splitting for collective rotations [1, 78].

It seems clear from the above discussion that the behaviour of the anisotropy coefficient, a_2, as function of the energy, can be useful to differentiates between prolate and oblate nuclei rotating collectively, but it is more difficult to distinguish between the collective prolate and non-collective oblate shape. Moreover, this anisotropy is more pronounced for γ–ray angular distributions measured with respect to the spin axis of the CN than with respect to the beam axis, since the latter averages over all possible CN directions.

In case of fission of the system, the CN spin direction can be determined from the fission fragment velocities direction. In the classical limit, the spin is perpendicular to the reaction plane defined by the fission fragments velocities and the beam axis. The a_2 coefficients for γ ray-fragment angular correlations with respect to the spin axis have opposite signs and are twice as large as those obtained with respect to the beam axis, because there hasn't been an average over CN spin directions (for more details see [79]).

1.4 Pre–equilibrium GDR

During the studies on the GDR, it has been proposed the possibility [4–9] that, in heavy ion fusion reactions, a significant dipole *strength* could be excited in the early moments of the nuclear interaction, called *pre–equilibrium* GDR or *Dynamical Dipole*(DD) mode. This pre-equilibrium oscillation decays giving rise to a prompt radiation that appears as an extra strength in the energy region of the statistical γ–rays coming from the thermal excitation of the GDR in the CN.

In [4] it was suggested that this pre–equilibrium emission is due to the charge asymmetry between the two colliding ions, $\Delta = \left| \left(\frac{N}{Z}\right)_{projectile} - \left(\frac{N}{Z}\right)_{target} \right|$

(with N (Z) equal to the number of neutrons (protons)). In this case, at the beginning of the reaction (when the distance between the center-of-mass of the two colliding ions is equal to the sum of their radii), along the collision axis that coincides with the Oz axis of the beam, there is a non vanishing dipole moment between the two ions, described as:

$$D(t=0) = \frac{NZ}{A}\,|R_Z(t=0) - R_N(t=0)| = \frac{r_0(A_p^{1/3} + A_t^{1/3})}{A} Z_t Z_t\,\Delta \quad (1.23)$$

where R_Z and R_N are the center-of-mass coordinates of protons and neutrons, respectively, $A = A_p + A_t$ is the CN mass, $N = N_p + N_t$ ($Z = Z_p + Z_t$) is its number of neutrons (protons) while the indices p and t refer, respectively, to projectile and target.

From the experimental point of view, during the last years several studies were devoted to the comprehension of this pre–equilibrium emission and its dependence on the charge asymmetry of the input channel. Our group observed in [14, 15] a pre–equilibrium dipole strength in the dissipative reactions ^{35}Cl + ^{64}Ni and ^{35}Cl + ^{92}Mo performed at incident energies of 7 ÷ 8 MeV/nucleon. Later on, we presented an experimental evidence of the dependence of the pre–equilibrium dipole strength on the collision centrality for dissipative heavy ion collisions. The studied reactions, ^{32}S + ^{58}Ni and ^{32}S + ^{64}Ni at incident energies of $\sim 9 \div 10$ MeV/nucleon [17], that differed in the initial dipole moment, were performed at the Laboratori Nazionali di Legnaro (LNL, Italy). The γ–ray spectra taken in coincidence with complex fragments emitted in the above reactions, if compared with each other, presented a net difference in the energy region between $\sim$ 10 and $\sim$ 18 MeV where it is expected the decay of the GDR in the dinucleus created in the charged asymmetric system, ^{32}S + ^{64}Ni . In the same experiment it was noted that, for quasi–elastic reactions, no pre-equilibrium γ–ray emission was observed within error bars. This result was associated with the short dinucleus lifetime, as fragmentation occured before complete relaxation of the charge degree of freedom between the colliding ions. The obtained result constituted an experimental proof of the fact that the dipole γ emission from the dinucleus decreases with decreasing the centrality of the reaction. For very peripheral reactions, the dipole radiation disappears rapidly since the interacting system has not time to organize a dinuclear mean field in order to trigger the oscillation. These observations were in good agreement with theoretical calculations in the framework of *Boltzmann-Nordheim-Vlasov* (BNV) transport model presented in [17].

The DD mode has been investigated also in heavy ion fusion reactions [21–26]. The chosen observable is the γ–ray multiplicity spectra of the CN formed at the same excitation energy and with the same spin distribution, from input channels having different charge asymmetry. Thanks to this method, the DD mode evidenced a γ–rays excess in the more charge asymmetric reaction.

The DD mode could be a powerful probe of the reaction dynamics, since its features depends on the symmetry term of the nuclear matter equation of state (EOS) that acts as a restoring force and on the interplay between different reaction parameters: impact parameter, collision energy, mass of the colliding ions, mass and charge asymmetry in the entrance channel. Thanks to its pre–equilibrium nature, the DD γ decay carries out relevant information about the first stages of the collision, in particular on the charge equilibration mechanism between the two interacting nuclei. This collective response develops in the low density neck region between projectile and target [7, 9, 27]. Therefore the DD emission is expected to be sensitive to the density dependence of the EOS symmetry term below saturation. Presently, a particular effort is made to study the symmetry term of the equation of state [9, 29] also because of its implications in nuclear astrophysics problems such as neutron stars and the elements burning in supernovae [80].

Besides the observation of a γ–ray excess in the charge asymmetric reaction spectrum, the study of its angular distribution completes the scenario of the DD mode and gives important piece of information about the early stages of fusion dynamics. The angular distribution, indeed, is a further signature of the dipole nature of this emission mechanism and is also sensitive to the timescale of DD oscillation and therefore of the charge equilibration process [29].

The DD oscillation is expected to occur along the dinuclear system symmetry axis, which for central and near-central collisions forms a relatively small angle with the beam axis at the very early moments of its formation. For a dipole oscillation just along the beam axis we expect an angular distribution of the emitted photons with a_2 = -1. In the case of a larger mean inclination of the DD axis, because rotation of the system has taken place meanwhile, we would expect a widening of the angular distribution and an anisotropy coefficient of $a_2 > -1$. Thus the a_2 coefficient could provide us information on the DD γ emission timescale (more details in sec. 4.2.3).

1.4.1 Incident energy dependence and dynamical dipole γ ray angular distribution

The first systematic study of the DD features (centroid energy, width, intensity) as a function of the incident energy was performed in our previous campaign of experiments [23–26] where compound nuclei in the ^{132}Ce mass region were created. In those measurements, the ^{132}Ce CN was formed through different charge asymmetry entrance channels at identical excitation energy and with identical spin distribution by using two reaction pairs: ^{36}S + ^{96}Mo (D(t = 0) = 1.7 m) and ^{32}S + ^{100}Mo (D(t = 0) = 18.2 fm) at 6 and 9 MeV/nucleon and ^{40}Ar + ^{92}Zr (D(t = 0) = 4.0 fm) and ^{36}Ar + ^{96}Zr (D(t = 0) = 20.6 fm) at 16 MeV/nucleon.

The above studied reaction pairs form a CN in the same mass region and they are characterized by the same initial dipole moment difference and a very similar initial mass asymmetry. This can be seen in table 1.1, where we summarize the entrance channel relevant quantities for all the studied reaction pairs leading to compound nuclei in the Ce mass region.

In the last column of the table 1.1 the values of the mass asymmetry, Δ_m, of the corresponding reaction are shown, where Δ_m is given by:

$$\Delta_m = \frac{R_t - R_p}{R_t + R_p} \tag{1.24}$$

where R$_p$ and R$_t$ are the radii, respectively, of projectile and target.

To better evidence details in the GDR energy region the experimental γ–rays multiplicity spectra were linearized, dividing them by the same theoretical spectrum calculated using the code CASCADE. This code allows to analyze the decay of a CN with the statistical model [57]. The theoretical

Table 1.1: *Reaction pair, incident energy, CN excitation energy, initial dipole moment D(t=0), initial mass asymmetry Δ and percent increase of the intensity in the 90° linearized γ-ray spectra for the charge asymmetric system (the energy integration was done from 8 to 21 MeV), obtained as described in the text.*

Reaction	E_{lab} (MeV/n)	E^* (MeV)	D(t=0) (fm)	Δ	Increase (%)
^{32}S+^{100}Mo	6.125	117	18.2	0.19	1.6 ±2.0
^{36}S+^{96}Mo	5.95	117	1.7	0.16	
^{32}S+^{100}Mo	9.3	174	18.2	0.19	25 ±2
^{36}S+^{96}Mo	8.9	174	1.7	0.16	
^{36}Ar+^{96}Zr	16	285±9	20.6	0.16	12 ±2
^{40}Ar+^{92}Zr	15.1	284±9	4.0	0.14	

spectrum calculated has been adjusted to take into account the response function of the experimental apparatus using the code GEANT [81].

The figure 1.5 shows a comparison between the linearized multiplicity γ spectra obtained for the charge symmetric and charge asymmetric reactions at the three different incident energies. The ordinate shows the following quantity:

$$F_{GDR}(E_\gamma) \propto \frac{S\,\Gamma_{GDR}\,E_\gamma}{\left(E_\gamma^2 - E_{GDR}^2\right)^2 + E_\gamma^2\,\Gamma_{GDR}^2} \tag{1.25}$$

where a lorentzian function is used to parameterize a photoabsorption cross section and S is the percentage of the TRK sum rule exhausted by the GDR (1.14 et seq.).

These results show that there is an increase in the dipole strength in the charge asymmetric reaction of each reaction pair. The γ–ray excess becomes maximum at the incident energy of 9 MeV/nucleon and decreases for higher and lower values of incident energy.

The percentage increase of the dipole γ emission in the linearized spectra

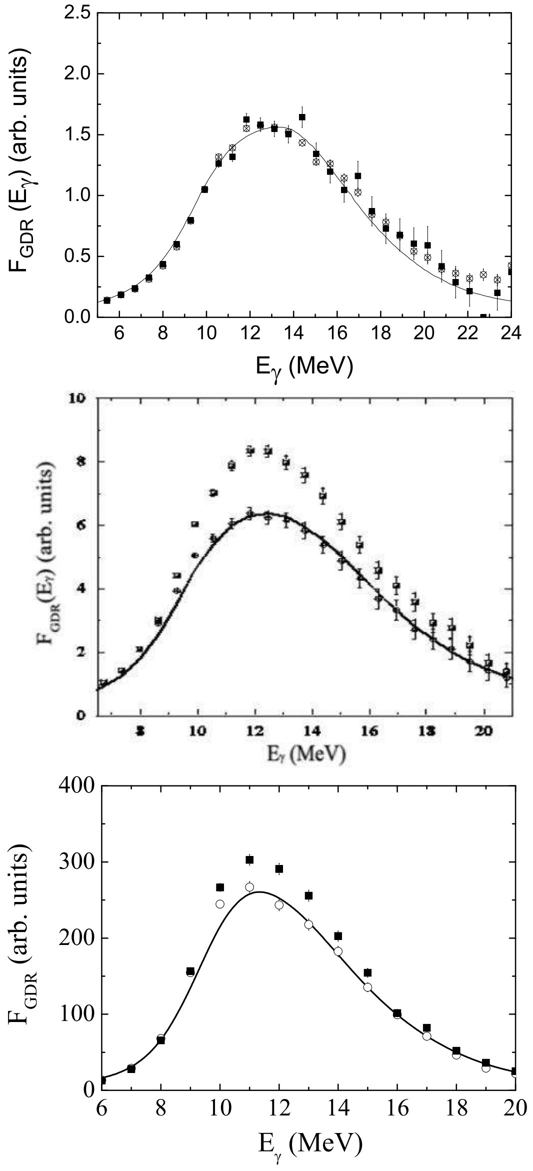

Figure 1.5: *γ spectra for the N/Z symmetric (circles) and for the N/Z asymmetric (squares) reactions, performed at 6 MeV/nucleon (top), at 9 MeV/nucleon (middle) and at ∼ 16 MeV/nucleone (bottom), linearized as described in the text. The solid line is obtained with the CASCADE code.*

was calculated as follows:

$$Increase(\%) = \frac{a-b}{b} \times 100 \tag{1.26}$$

where a and b are equal to the integral $\int_{E_1}^{E_2} F_{GDR}(E_\gamma)dE_\gamma$ for the N/Z asymmetric reaction and N/Z symmetric one, respectively (E_1 = 8 MeV and E_2 = 21 MeV).

The experimental DD absolute γ-ray multiplicities, integrated over energy, were compared with theoretical predictions presented in [9, 27] according to which the dipole emission depends on the incident energy through its dependence on the initial isospin asymmetry, on the time of formation of the CN and on the *spreading width* of the GDR. According to these calculations, the prompt dipole emission assumes its maximum value in the energy range between values around the Coulomb barrier and the Fermi energy domain. However, the predicted energy dependence of the DD γ–ray yield within these calculations showed a smoother behaviour with respect to that displayed by the experimental results (for more details see [26]), as displayed in picture 1.6. In the above picture the total prompt dipole radiation yields evaluated (absolute values) for the ^{36}Ar+^{96}Zr and ^{32}S+^{100}Mo reactions, together with the available data (points in the figure) obtained integrating the γ–ray excess over energy and over solid angle and by taking into account the corresponding experimental set up efficiency are presented. In the integration of the data over solid angle an $a_2 = -1$ anisotropy coefficient for the DD yield was considered. There are different sets of calculations done with in-medium reduced nn cross sections corresponding to nuclear densities that change locally during the reaction dynamics at each time step of the collisional procedure and with different parametrizations of the EOS, Asystiff and Asysoft.

Furthermore, in these works [23–26], the DD centroid energy was found to be lower than that of the CN GDR, in agreement with theoretical predictions for an oscillation along the symmetry axis of a deformed dinuclear shape. In [25, 26] the first DD angular distribution data were presented supporting its pre-equilibrium nature. In this work, a large anisotropy of the DD γ–ray angular distribution with respect to the beam direction was found, much

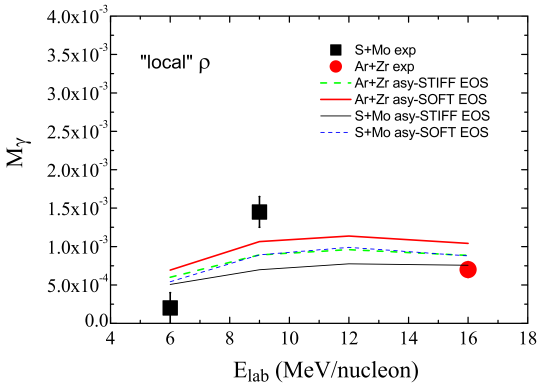

Figure 1.6: *Experimental multiplicity of the observed γ–ray excess for the reactions* $^{32,36}S$ + $^{100,96}Mo$ *and* $^{36,40}Ar$ + $^{96,92}Zr$ *integrated over energy and over solid angle corrected by the experimental setup efficiency and theoretical calculations obtained for a local density and in-medium reduced nn cross sections.*

larger than that corresponding to emission of statistical high-energy dipole γ–rays from a deformed hot CN. This anisotropy was interpreted as the signature of a preferential oscillation axis of the DD triggered at the early stage of the fusion path along an axis that has not rotated much with respect to the beam axis.

In [28] the DD was investigated in the same composite system in the vicinity of ^{132}Ce by employing a different entrance channel, the ^{16}O+^{116}Sn reaction at E_{lab} = 8A and 15.6A MeV and by using a different technique: the DD γ decay was evidenced by subtracting from the experimental γ–ray spectrum the statistical spectrum calculated by means of the code CASCADE at an excitation energy that was evaluated from the charged particle energy spectra. The comparison of the two data sets [25, 28] with each other and with the theoretical predictions [27], proves that further investigation is needed, from both the theoretical and the experimental point of view, to shed light on the interplay between the different parameters that influence the DD features. However, it is worth noting that at the moment, there are very few data of the DD γ–ray absolute multiplicity and on its angular distribution.

Therefore, more systems should be studied, in a systematic way, in order to provide severe constraints to the existing theoretical models.

1.4.2 Mass asymmetry dependence

To isolate the dependence of the DD emission on the incident energy, it is important to choose the mass asymmetry values in the proper way, as mentioned in the previous paragraph, since it could influence the emission of pre–equilibrium dipole γ–rays .

The mass asymmetry between the two colliding ions plays a fundamental role in the dynamics of a fusion reaction, as explained in a dynamic model [82]. This model predicts that the time scale of the fusion process should also depend on the fissility parameter of the system. The fissility parameter, X_0, can be expressed as:

$$X_0 = \frac{Z^2\, e^2}{16\, \pi\, \gamma\, R^3} \tag{1.27}$$

where γ is the surface coefficient of the liquid drop model. In picture 1.7 the behaviour of the mass asymmetry δ_m in function of X_0 is shown for some reactions.

In this picture, the solid line shows the critical curve $x = x_c$, where x refers to the effective fissility:

$$x = X_0 \cdot \frac{1 - \Delta_m^2}{1 + 3\Delta_m} \tag{1.28}$$

The x quantity can be seen as a line of demarcation of the influence of dissipative effects on the dynamics of fusion process. For systems with $x < x_c$ dissipative effects are expected to be small and the system fuses and equilibrates rapidly, while for $x > x_c$ dissipative effects impede fusion and the dynamical evolution toward an equilibrated system should be slower. The experimental results presented in [83, 84] show that with different combinations of projectile and target, leading to the same CN, located to the left and above the $x = x_c$ line, dissipative dynamical effects are small. Hence it was

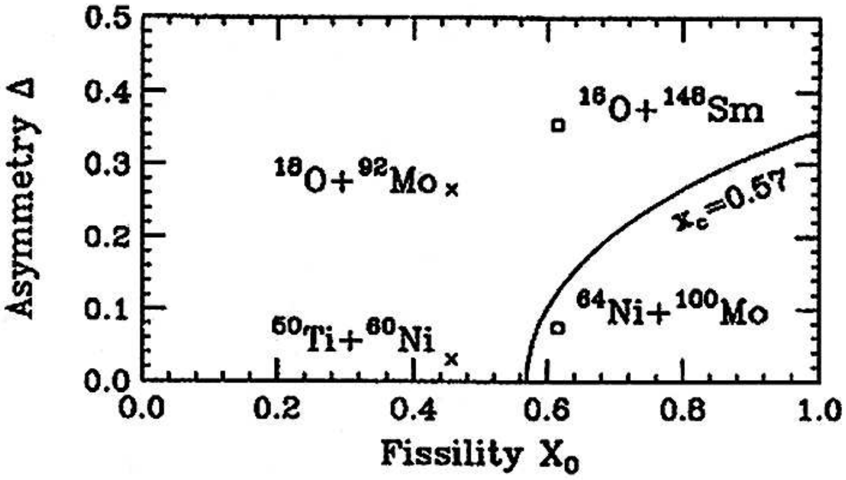

Figure 1.7: *Mass asymmetry Δ_m as a function of fissility X_0 for the compound nuclei ^{164}Yb (□) and ^{110}Sn (x).*

not observed any difference in the γ–ray emission from the GDR decay. On the contrary, choosing one of the reaction partner above the critical curve of figure 1.7, dissipation effects lead to differences in the decay of the statistical GDR.

In the experiments [24–26] mentioned previously, the colliding systems were chosen to the left and above the critical curve of figure 1.7, in such a way that dynamical dissipative effects didn't influence the GDR features. The initial mass asymmetry for the reactions ^{32,36}S + ^{100,96}Mo and ^{36,40}Ar + ^{96,92}Zr was equal to 0.19 - 0.16 and 0.16 - 0.14, respectively. Therefore the two pairs of reactions were directly comparable and the difference in the dipole γ–ray emission for each reaction pair was safely ascribed to the initial dipole moment difference and not to the mass asymmetry one.

1.4.3 Thesis project

As shown from the data obtained so far, the DD γ–ray emission, under certain conditions, becomes comparable with the γ emission from the GDR excited in the CN and could therefore be of considerable interest in the production of superheavy elements. The idea is to use this fast emission as a “cooling” mechanism of the system on the fusion path, increasing thus the survival probability of superheavy elements against fission in hot fusion reactions.

Experimentally, two approaches have been used so far for the synthesis of these elements, one utilizing closed-shell nuclei with lead-based targets (cold fusion) [85, 86], the other utilizing deformed actinide targets with ^{48}Ca projectiles (hot fusion) [87, 88]. While both methods have been successful in synthesizing new elements, the evaporation residue cross sections of the hot fusion reactions were found to be larger than those of the cold fusion ones. The excitation energy of the composite system formed in hot fusion reactions is one of the key parameters for the super-heavy element survival against fission because (1) smaller excitation energies have smaller fission probabilities and (2) the shell corrections, responsible for the stability of super-heavy nuclei, decrease with excitation energy. It was estimated in [89], in the framework of an ”hybrid” statistical model of the CN decay in which the pre-equilibrium γ–ray emission is externally introduced while the fission width evolution is given by the diffusion model for fusion-fission dynamics described in [90], that the lowering of the CN excitation energy by an amount ranging between 10 and 15 MeV, the typical energy removed by a pre-equilibrium photon coming from the DD decay, results in an increase of its survival probability against fission and thus in an increase of the evaporation residue cross section by a factor of $\sim$10. However, in order to predict evaporation residue cross sections of super-heavy elements in charge asymmetric reactions, we need a realistic theoretical model that follows the dynamical evolution of the system in the multi-dimensional potential energy landscape through quasi-fission or formation of the CN and its subsequent evaporation and fission, including the pre-equilibrium dipole γ–ray emission in the early stages of the collision. It was predicted in [7] that the DD γ yield decreases in collisions involving heavy mass partners because reactions with small nuclei are less damped than those involving more nucleons. Thus, to verify a potential usefulness of the DD in the super-heavy element formation, besides an appropriate theoretical model to predict evaporation residue cross section, its existence in heavier systems than those studied so far should be experimentally studied as a first step.

For these reasons, we decided to investigate the DD in a composite system in the vicinity of ^{192}Pb, in both fusion–evaporation and fission events for the first time. In this way, besides shedding light on the opportunity to use its prompt γ radiation to cool down the composite system on the way to fusion, information on the DD γ decay can be added on the scarce body of existing data.

The experiment was performed at the Laboratori Nazionali del Sud, (LNS, Italy) in 2007 by using the ^{40}Ca(^{48}Ca) pulsed beam provided by the Superconducting Cyclotron, impinging on a 1 mg/cm^2 thick self-supporting ^{152}SmO$_2$(^{144}SmO$_2$) target enriched to 98.4%(93.8%) in ^{152}Sm(^{144}Sm) at E$_{lab}$ = 440(485) MeV. Both entrance channels populate the same CN through a quite different initial dipole moment ranging from 30.6 fm for the ^{40}Ca + ^{152}Sm charge asymmetric reaction to 5.3 fm for the ^{48}Ca + ^{144}Sm more charge symmetric one. The mass asymmetry of the two entrance channels is very similar, namely 0.22 and 0.18, respectively, for the ^{40}Ca + ^{152}Sm and ^{48}Ca + ^{144}Sm reactions, while the fissility of the system X_0 is equal to 0.715. Furthermore, the formed CN has identical excitation energy in both reactions, as explained in section 3, and identical spin distribution: L$_{max}$ = $42\hbar$ for fusion-evaporation, while fusion-fission reactions occur at angular momenta up to L$_{max}$ = $74\hbar$, according to PACE2 calculations [91] performed by using a level density parameter a = A/10 MeV^{-1}.

All the parameters are equal or comparable to each other, except for the initial dipole moment. In this way, we are sure that any difference in the DD emission between the two reactions is only due to the different initial dipole moment.

In the present thesis the data analysis of all the statistics collected during the experiment is shown. After performing the energy calibration of the detectors, the data were suitably reduced, as explained in detail in section 3, in order to obtain the γ–ray multiplicity spectra and angular distribution (see sections 4, 5) for both fusion–evaporation and mass symmetric fission events, in the two reactions.

Chapter 2

Choice of the detectors

2.1 Scintillators

The scintillation detectors are certainly the most used detectors in the context of nuclear physics, both for the fast response and for the high detection efficiency. These are schematically constituted by a scintillator material that is optically coupled to a photomultiplier or directly or through a light guide. When a radiation (γ-rays or charged particles) interacts with the detector, it causes a shift of electrons from the valence band to the conduction one. The decay of the system to the initial state results in the emission of a light radiation that is caratheristic of the scintillator material [92]. If this emission occurs in a time of the order of 10^{-8} s, the process is called *fluorescence*, while if it is longer (metastable state) it takes the name *phosphorescence*. The light emission process presents the following behavior :

$$N = A\,exp\left(-\frac{t}{\tau}\right) \tag{2.1}$$

where τ is the decay constant. For some scintillators, as better explained in section 2.1.2, the light emission can be described by two components with different decay constants. In this case we speak of slow component (*slow*) and rapid component (*fast*) and the scintillation process follows the time evolution :

$$N = A_f \, exp\left(-\frac{t}{\tau_f}\right) + A_s \, exp\left(-\frac{t}{\tau_s}\right) \tag{2.2}$$

where τ_f and τ_s are the decay constants of the fast and the slow component respectively, while A_f and A_s are the relative intensities, which vary from material to material. As we will see later in Section 2.1.2, this feature is the basis of the *pulse shape* discrimination technique, i.e. the discrimination of the incident radiation through the shape of the emitted light pulses.

Generally scintillators detectors are linear devices, i.e. the intensity of the emitted light is directly proportional to the quantity of energy lost by the incident radiation within the scintillator material. The scintillation efficiency is defined as the fraction of energy of the incident radiation that is converted into scintillation light [92].

The scintillation detectors are generally divided into two categories: organic and inorganic. The organic scintillators generally give a quick response, within 10 ns, but have a low light output, $\sim 4{*}10^3\gamma$/MeV: they are therefore more suitable for time measurements. The inorganic scintillators, such as crystals of NaI(Tl) and CsI(Tl), are instead slower with response times of the order of $200 \div 500$ ns, but have a high light output of $\sim 4{*}10^4\gamma$/MeV in case of NaI(Tl), which makes them more suitable for energy measurements. Furthermore, these two classes of scintillators present a different mechanism of scintillation. In the case of organic scintillators, the scintillation light comes from transitions of the free electrons of valence between the energy levels of the molecules. In the case of the inorganic ones, the scintillation process has a molecular origin, since it comes from the electronic band structure present in the crystals [93].

A photomultiplier is an electronic device able to convert, by photoelectric effect, an incident radiation of wavelength between ultraviolet and infrared into an electrical signal. This signal is amplified by emission of secondary electrons, to bring it to a level such as to allow the analysis.

A photomultiplier consists of a photocathode, an electron multiplier and an anode. The sensitivity of the conversion of the photocathode is expressed in terms of quantum efficiency that is defined as the ratio between the number of electrons emitted by the photoelectric effect from the cathode and the number of incident photons, of given wavelength λ. This amount is very important for the energy resolution of the detector. In the present case, the used photomultipliers are equipped with a quartz window that allows a good transmission of wavelengths between 160 nm and 650 nm to be suitable to the characteristic wavelength of the scintillator used as we will see in section 2.1.2.

2.1.1 γ-ray detectors

The detectors which are generally used for the detection of γ-rays are semiconductor detectors (typically Germanium) and inorganic scintillators that are also able to detect neutrons. If we are interested only in the detection of the γ-rays, as in our case, neutrons are an undesired background that, therefore, must be eliminated. In our experiment a discrimination of γ from neutron background was performed using a technique of measurement of time of-flight (ToF technique: *Time Of Flight*), the time taken by the radiation of interest to cover a known distance, usually the distance between target and detector. The criterion that has determined the choice of the type of detector to use was, therefore, to have an excellent timing resolution as well as high efficiency for the detection of γ and at the same time modest for the detection of neutrons.

A Ge detector has an excellent energy resolution (~0.15 % for γ of energy equal to 1.33 MeV emitted by a ^{60}Co source), but its timing resolution (~5 ns) does not allow a good discrimination γ - neutrons. The inorganic scintillators present high density and high atomic number with a consequent high *stopping power*. Therefore, these scintillators have the best detection efficiency for γ-rays. $Bi_4Ge_3O_{12}$ (Germanate Bismuth or BGO) is characterized by a high density (7.13 g/cm^3) and a high atomic number provided by Bismuth (Z = 83). These properties would make the BGO a good γ-ray detector. However, this scintillator has a light yield of $\sim 10 \div 20\%$ of that of a NaI(Tl) and therefore, a poor energy resolution ($\sim$ 16% for γ of energy equal to 0.662 MeV emitted by a ^{137}Cs source). Furthermore, the BGO has a poor timing resolution of 5 ns. On the other hand, the NaI(Tl) scintillator, despite having a good energy resolution ($\sim$ 8% for γ of energy equal to 0.662 MeV emitted by a ^{137}Cs source), is characterized by a timing resolution of the order of 5 ns.

In this experiment we choose a particular type of inorganic scintillator: BaF_2 (barium fluoride). The crystal BaF_2 has an energy resolution of 10% for γ from 0.662 MeV, therefore worse than that of the NaI(Tl), but it becomes comparable (8%) at low temperatures ($243 \div 253$ K). In our case however, a high energy resolution is not essential because, as we will see in the next chapter, we are interested in γ-ray spectra typical of the region of the continuum. On the other hand, since its density is higher than that of the NaI(Tl) (see section 2.1.2), it is characterized by a higher detection efficiency for γ-rays which allows a reduction in the volume of the used detectors; in addition its neutron detection efficiency is lower and this is a great advantage if we are interested in detecting only γ-rays. The more important characteristic for our purposes is its excellent timing resolution ($\sim$ 300$\div$ 500 ps), which allows a very good γ–rays - neutrons discrimination.

2.1.2 BaF_2 scintillator

BaF_2 is a pure inorganic scintillator, that does not require the presence of an activator element to excite the process of scintillation. The luminescence is an intrinsic property of the crystal and the presence of impurities does not change the light yield.

The scintillation light of a BaF_2 consists of a slow component with a decay time of τ_s = 630 ns and wavelength λ_s = 310 nm, which corresponds about 80% of the total intensity, and a rapid component having a lower decay time τ_f = 0.6 ns and wavelength λ_f = 220 nm. Figure 2.1 shows the two components in the emission spectra of a BaF_2 measured at different temperatures.

The presence of a very rapid component provides an excellent timing resolution; for large detectors (diameter and length of the order of tens of cm) the measured resolution is about 400 ps and improves with decreasing the size of the crystal. It also allows to discrimate γ–rays , protons, deuterons and α particles by analyzing the shape of the signal. The two components come

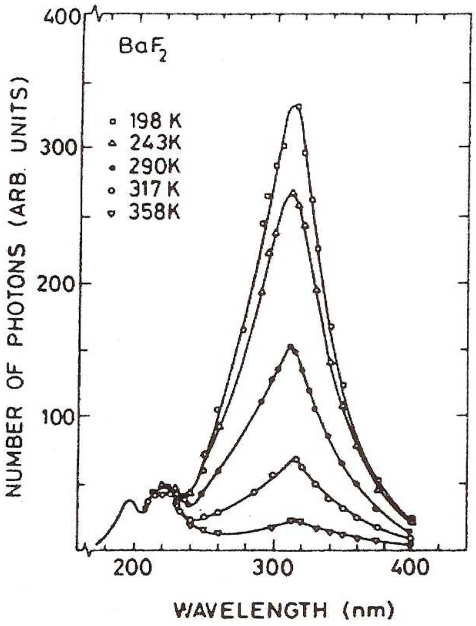

Figure 2.1: *Emission spectra of a BaF$_2$ measured at different temperatures.*

from the de-excitation of different states of the scintillator, which are populated in different proportions depending on the specific energy loss dE/dx of the incident radiation; in particular the rapid component is less intense for charged particles that for γ-rays and decreases as the charge and mass of the particles.

Thanks to its high density (4.88 g/cm^3), the BaF$_2$ is also suitable to stop very energetic particles, in particular γ-rays; indeed a thickness of about 15 cm is sufficient to achieve an efficiency of almost 100% for γ-ray energies up to 20 MeV. However, the penetration of the electromagnetic shower within the crystal, which develops from an incident photon, increases with the photon energy [94]. Because of the escape of the created secondary photons and electrons and positrons, a good part of the energy of the incident photon can not be detected.

In this experiment it was chosen a BaF$_2$ with the shape of a truncated pyramid with a height of 20 cm. This thickness is efficient for energies up to $\sim$ 300 MeV for γ-rays and $\sim$ 1 GeV for protons and α-particles.

2.2 Reaction products detectors

The energy loss of a reaction product, passing through a given material, is essentially due to inelastic collisions with the atomic electrons of the material itself, while the elastic scattering from the nuclei is a very rare process [93]. Following each collision, the incident fragment transfers part of its kinetic energy to an atom causing excitation or ionization of the latter.

The energy transferred in a single collision is generally very small, however the number of collisions per unit of length is very high so the incident particle undergoes a gradual loss of energy along its path in the material. For non-relativistic charged particles ($v \;<<$c) charge Ze, and with speed v, the average energy loss per length unit (*stopping power*) is given by the formula of Bethe–Bloch [94] :

$$-\frac{dE}{dx} = C_1 \frac{Z^2}{v^2} \, N Z_m \, ln(C_2 v^2) \tag{2.3}$$

where C_1 and C_2 are constant and N and Z_m are, respectively, density and atomic number of the material. For different particles with equal speed the only determining factor is Z^2, for which high charge particles lose a greater amount of specific energy. The energy loss of a particle in different materials depends on, finally, the product $N{\cdot}Z_m$; so when it is required a great stopping power, materials of high atomic number and high density are preferred.

The evaporation residues and fission fragments were discriminated from all other possible reaction products on the basis of their energy loss in the detector and on their ToF; thus it is necessary the choice of a detector characterized by an appropriate timing resolution.

The solid state detectors present both a good time resolution ($\sim$ 1$\div$ 3 ns for α particles and $\sim$ 2$\div$ 5 ns for heavy ions and fission fragments) and a good energy ($\sim$ 0.3% for α particles of 5.486 MeV), but in our case they are not very suitable because of their rapid deterioration due to the radiation. Alternatively, it is possible to use gas detectors which are in general not very sensitive to damage by radiation and their shape can be adapted to different experimental setups. A good response time is provided by a parallel plate avalanche detector (**P**arallel **P**late **A**valanche **C**ounter: **PPAC**); its output signal has a rise time of a few ns and allows to determine the instant of transit of the particle with a precision of the order of some hundreds of ps.

2.2.1 Parallel Plate Avalanche Counter (PPAC)

1) Evaporation events: the whole detector was made of four separated PPACs mounted in an annular configuration as shown in (figure 2.2), to have symmetry around the beam direction. Each of the four PPACs is a gas detector constituted by three electrodes arranged in parallel planes: two anodes and a central cathode between them, placed at a distance of 2.4 mm from each anode. In figure 2.2 we show the four PPACs mounted in an annular configuration for the detection of evaporation residues: front and back side of the detector in the left and right-hand side of the figure, respectively.

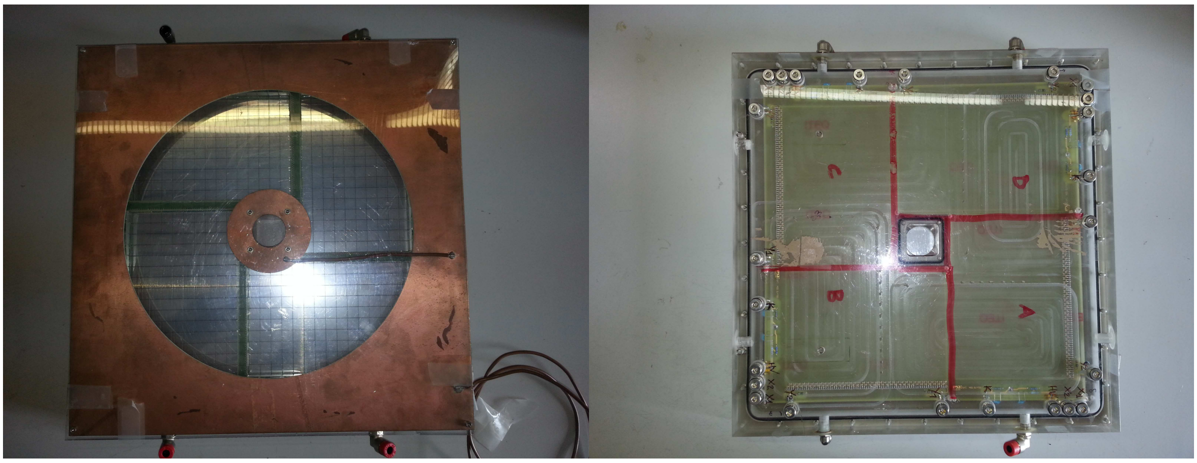

Figure 2.2: *The four PPACs mounted in an annular configuration for the detection of evaporation residues: front and back side of the detector in the left and right-hand side of the figure, respectively.*

The cathode is a unique electrode consisting of two layers of aluminized mylar (thickness of 1.5 μm), with an active area equal to 100 × 150 mm^2. The two anodes are, instead, grids having, respectively, 48 horizontal copper strips, placed at a distance of 0.1 mm apart, and 60 vertical wires, 1 mm away from one other. Each strip is 2 mm wide and 100 mm long, each wire is 150 mm long. A voltage of $\sim$ 500 V is applied to the cathode while the two anodes are grounded. It creates so a uniform electric field between the two electrodes.

The set of three electrodes is, then, placed inside a container in which the gas circulates (in our case isobutane (C_4H_{10})), at low pressure ($\sim$ 9 torr).

A charged fragment, passing through the detector, ionizes the gas leaving, along its trajectory, a certain number of electron-ion pairs. The primary electrons migrate to the anode and, due to the high electric field, acquire enough energy to ionize other gas atoms, therefore it is observed an avalanche phenomenon known as *Townsend avalanche* [93]. The number of secondary electrons collected on the anode is equal to:

$$N = N_0 \, exp(\alpha x) \tag{2.4}$$

where N_0 is the number of primary electrons, x is the distance of migration, which is the distance traveled by the electrons from the instant of creation to the anode, and α is the Townsend coefficient. Since, the final number of electrons depends on the distance x, it is not proportional to the number of primary electrons; therefore the energy loss measurement is not very precise (uncertainty of $\sim$ 15%).

The output signal consists of a fast part (short rise time), corresponding to the collection of electrons, which is used for the temporal information and a slow part produced by the collection of positive ions. The signal coming from the cathode is used to obtain the information regarding the energy loss ΔE of the incident particle within the gas and to provide its ToF.

With this type of detector it is possible to determine the position of the incident particles detected on the cathode. This information is provided by the signals collected on the anodes. The electrons, which are mostly produced in close proximity of the cathode, follow the electric field lines, head towards the anodes and induce a negative signal on the wire or strip closer to the created avalanche. In fact some parasites signals are observed on close wires (strips), but of smaller intensity. The horizontal and vertical wires are coupled to delay lines which allow to determine respectively, the horizontal (X) and vertical (Y) position of incidence. The electrons travel the delay lines in X and Y, giving rise to the signals, at the border of the lines, whose amplitude is inversely proportional to the traveled distance. At the end four signals are produced: X_1, X_2, Y_1, Y_2. The arrival times of these signals, from the instant when the nuclear reaction begins, provides the position of incidence on the cathode.

A PPAC detector can be used to detect nuclei with an atomic number Z ≥ 6 with an efficiency of $\sim 100\%$.

2) Fission events: each position sensitive PPAC used for the detection of the fission events has an active area of 62 x 62 mm. It consists of a cathode plate (unique electrode) located between two anodes. Each anode has 60 wires at a distance of 1.0 mm and the two anodes are oriented perpendicularly to each other, to allow a position resolution of 1.0 mm × 1.0 mm. The wires are connected to 2.5ns/mm delay-lines and signals are collected from each end of the delay lines (both in x and y direction) and from the cathode for an overall number of five signals for each PPAC. The cathode is 1.5 μm mylar foils with 30 nm of aluminum evaporated on both surfaces. The distance between each anode and the cathode is about 24 mm and is filled with isobutane (C_4H_{10}) at a pressure of 8-10 torr. The detector windows are made by 1.5 μm mylar foils. A voltage of $\sim$ 500 V is applied to the cathode while the two anodes are grounded. In figure 2.3 (left-hand side) we show the PPAC for fission fragments and (right-hand side) the electrodes of the detector.

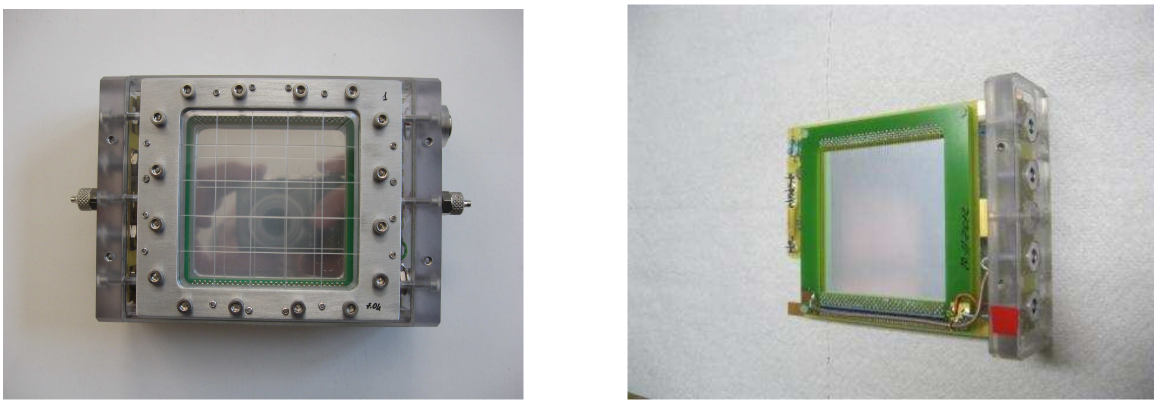

Figure 2.3: The PPAC for the detection of fission fragments (left) and its electrodes (right).

Chapter 3

^{40,48}Ca + ^{152,144}Sm at 11 and 10 MeV/nucleon

3.1 Experiment

In our experiment we investigated the ^{40}Ca + ^{152}Sm and ^{48}Ca + ^{144}Sm fusion reactions at incident energies of 440 and 485 MeV (equivalent to 11 and 10.1 MeV/nucleon), respectively. Both reactions lead to the formation of the same compound nucleus (CN), in the mass region of ^{192}Pb , from input channels having different N/Z values and therefore different initial dipole moment.

The ^{40}Ca + ^{152}Sm system is strongly asymmetric in N/Z, with a D(t=0) = 30.6 fm (Δ = 0.45), while the ^{48}Ca + ^{144}Sm one, almost symmetric in N/Z, presents D(t=0) equal to 5.3 fm (Δ = 0.08). The reactions thus have an initial difference of dipole moment equal to $\Delta D(t = 0) = 25.3$ fm. The dipole moment was calculated using the equation 1.23 with $r_0 = 1.2$ fm.

All the relevant parameters are kept constant between the two reactions, except for the initial charge asymmetry. Therefore, any difference between the experimental γ-ray spectra and angular distributions can be ascribed to this parameter. Indeed, in both cases the CN was formed at the same excitation energy E* and with the same spin distribution ($L_{max} = 74\hbar$, $L_{fus-evap} = 42\hbar$ as calculated with the code PACE2 [91]) by using a level density parameter a = A/10 MeV^{-1}, A being the CN mass. During the design of the experiment we choose the proper incident energy of the ^{40,48}Ca beams for having the same CN E* in the two reactions, by taking into account the energy loss ΔE_x due to pre-equilibrium particle emission. The ΔE_x was calculated by means of the relation given of [95]:

$$\Delta E_x\,(MeV) = 8.7\left[\frac{E_p - V_c}{A_p}\right] - 33 \tag{3.1}$$

where V$_c$ is the Coulomb barrier and E$_p$ and A$_p$ are, respectively, the incident energy and the mass of the projectile. Then, the E* was evaluated experimentally, as will be discussed in detail in section 4.1. The mass asymmetry of the two colliding ions is equal to $\Delta_m = 0.22$ for the ^{40}Ca + ^{152}Sm reaction and $\Delta_m = 0.18$ (see equation 1.24) for the ^{48}Ca + ^{144}Sm reaction. The fissility parameter X_0 (defined in 1.27) of the formed CN is equal to 0.715. Both systems are located above the critical curve in the plane (fissility X$_0$ *vs* mass asymmetry Δ_m) shown in Figure 1.7.

The reactions were performed using pulsed beams of ^{40}Ca and ^{48}Ca, provided by the *Superconducting Cyclotron* of the Laboratori Nazionali del Sud (LNS) and impinging respectively on self-supporting targets of ^{152}SmO$_2$ and ^{144}SmO$_2$ (1 mg/cm^2 thick), enriched to 98.4% and 93.8% in ^{152}Sm and ^{144}Sm, respectively. The targets have oval shape with a major axis equal to 12.0 mm and a minor axis equal to 9.0 mm, and were placed on a 0.2 mm thick ^{27}Al frame. The incident beams consisted of bunches with a FWHM of 4 and 3 ns, for the ^{40}Ca and ^{48}Ca, respectively, sent every 150 ns. The FWHM of the beam bunch was not optimal, due to the difficulty for the cyclotron to reach the chosen incident energy. Nevertheless it was sufficient to discriminate temporally different light particles and γ–rays and the different reaction products among them. The Δt between a bunch and the consecutive one was chosen in such a way as to be longer than the time of flight of the slower particle. During the whole experiment we worked with a beam current intensity of about 1 nA.

In both reactions, fusion–evaporation and fission events were selected. For the analysis of a single process, the chosen observables are the γ–rays double differential multiplicity in energy and solid angle (see formula 3.2) and the angular distribution of the observed γ–rays (for evaporation events). In case of fusion–evaporation, the events were selected detecting γ–rays in coincidence with the evaporation residues, while for fission it was requested a triple coincidence, between γ–rays and the two fission fragments.

3.2 The experimental setup

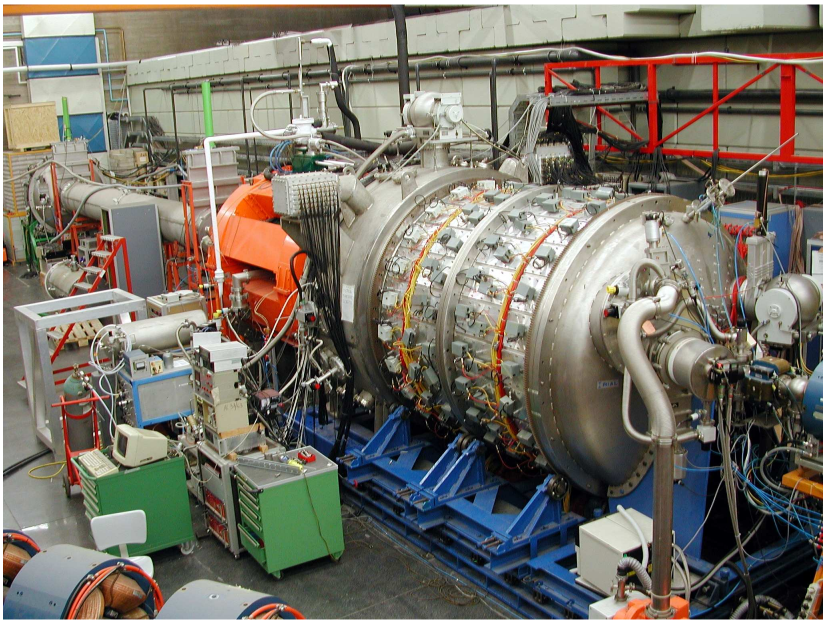

Figure 3.1: *View of the experimental hall. Inside the scattering chamber the multidetector MEDEA is placed.*

The measurement was performed with the experimental apparatus MEDEA (**M**ulti **E**lement **DE**tector **A**rray) coupled to six position sensitive **P**arallel **P**late **A**valanche **C**ounters (PPACs), four for evaporation residues in an annular configuration as mentioned previously and the remaining two for fission fragments. This system operates in vacuum (see photo in Figure 3.1) and therefore it is possible to measure not only γ–rays but also the light charged particles in coincidence with heavier reaction products.

The multidetector MEDEA [96] consists of 180 scintillators barium fluoride (BaF_2), coupled to as many photomultipliers, arranged in such a way as to form a sphere with an inner radius equal to 22 cm. The modules BaF_2 are distributed in groups of 24 on eight rings; each of them covers the whole angular range in ϕ, positioned at different polar angles θ (36°, 51.5°, 68.1°, 82.8°, 97.1°, 111.9°, 128.5°, 159.7°) relative to the incident beam direction, as shown in figure 3.2.

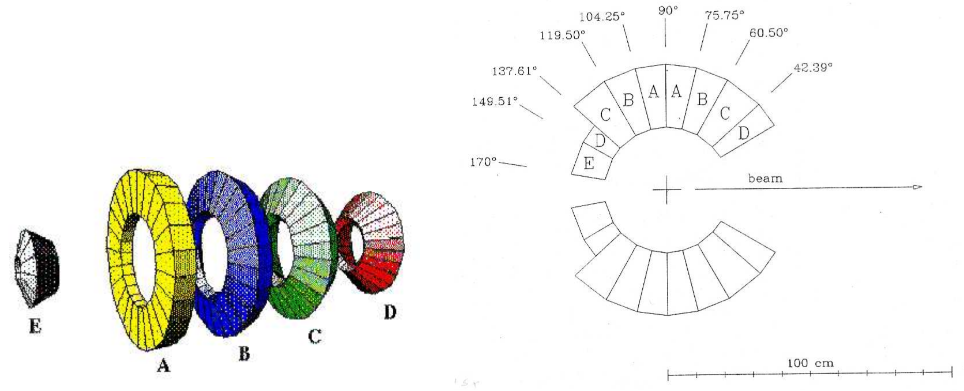

Figure 3.2: *The multidetector MEDEA is composed of 180 BaF_2 scintillators, arranged in different rings, as shown in the left-hand side. Each ring is placed at a fixed polar angle, covering the whole azimuthal angle, as shown in the vertical section (containing the beam direction) in the right-hand side.*

All the detectors subtend the same solid angle of $\sim$ 63 msr, while those belonging to the rings indicated by a letter D (see Figure 3.2) subtend a solid angle equal to 32 msr. The total geometrical efficiency of the apparatus is 3.8 π. In our experiment, however, all BaF_2 , except those belonging to type D, were used.

The evaporation residues PPACs were located at 70 cm from the target and placed symmetrically around the direction of the incident beam. This symmetry makes the angular correlation γ - evaporation residues, independent of the angle ϕ at which the γ–rays are emitted. The PPACs were centered at an angle $\theta = 7°$ subtending 7° in θ. This angle was chosen on the basis of calculations performed with the code PACE2 [91]: evaporation residues are distributed in an angular range up to 16°, presenting a maximum around 4.5° in the laboratory in both reactions. That ensures us that we selected experimentally the same compound nuclei in both reactions (about 70% of the whole evaporation residue cross section) avoiding thus any difference that could influence our results. The total solid angle subtended by evaporation-residues PPAC was equal to 0.089 sr. The PPACs gave the energy loss ΔE and the TOF of the reaction products.

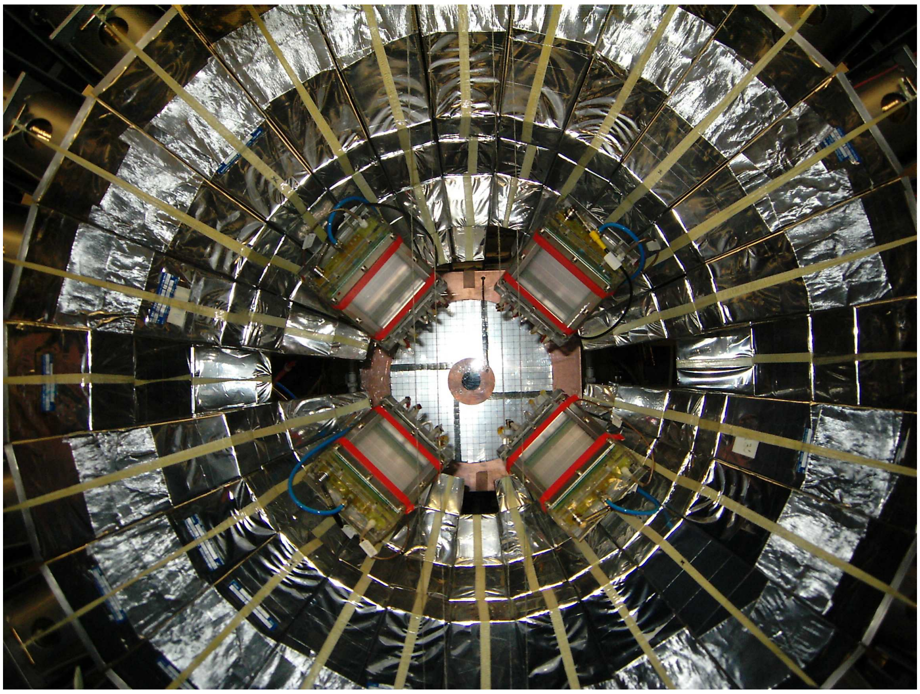

Figure 3.3: *Internal view of the scattering chamber: four PPACs for fission fragments together with the PPACs for the evaporation residues are shown.*

The detection of fission fragments was carried out with two position sensitive PPACs, positioned at 16 cm from the target symmetrically around the beam axis and centered at an angle $\theta = 52.5°$. Each PPAC subtended an angle of 22° in θ and ϕ. This setup allowed to study γ–ray - fission fragments angular correlation at different angles with respect to the spin direction of the composite system, that was taken to be perpendicular to the reaction plane at high spin values. These PPACs gave the energy loss ΔE, the TOF and the x and y positions of the fragments. From the above informations, angles, masses and velocity vectors of the fragments in the laboratory and the center-of-mass reference frame were obtained.

Down-scaled single evaporation and fission events together with coincidence events between at least one fired BaF_2 scintillator and a PPAC (two PPACs) for evaporation (fission) events were collected during the experiment. The coincidence condition avoids contamination of the γ-ray spectra due to high energy cosmic ray events. In figure 3.3 we show the PPACs for evaporation and fission fragments, inside the forward hemisphere of MEDEA. During the experiment only two from the four fission PPACs, appearing in the figure, were used.

3.3 Electronics and acquisition

The detection system, connected to an appropriate electronic chain, allows to obtain the following information:

- energy released from γ–rays and light charged particles in each BaF_2 in two different energy ranges: up to 30 MeV and up to 170 MeV;
- time of flight ToF of all radiation detected by BaF_2 scintillators;
- energy loss ΔE and time of flight of the reaction products detected by PPACs and x and y positions of the reaction products in case of fission PPACs.

Figure 3.4 shows the scheme of the electronic chains, connected to each detector, PPAC and BaF_2 , and the trigger scheme used during the experiment.

Time measurements were done in COMMON START configuration. This signal was generated by the coincidence between the cyclotron radiofrequency signal, suitably delayed, and the trigger signal. Since COMMON START signal is determined by the cyclotron radiofrequency, it is synchronized with the beginning of the reaction.

PPAC electronics

The signal from the cathode of each PPAC, for both evaporation and fission, was processed along two paths. In the first path the signal was amplified and shaped and then sent to an analog-to-digital converter (ADC)

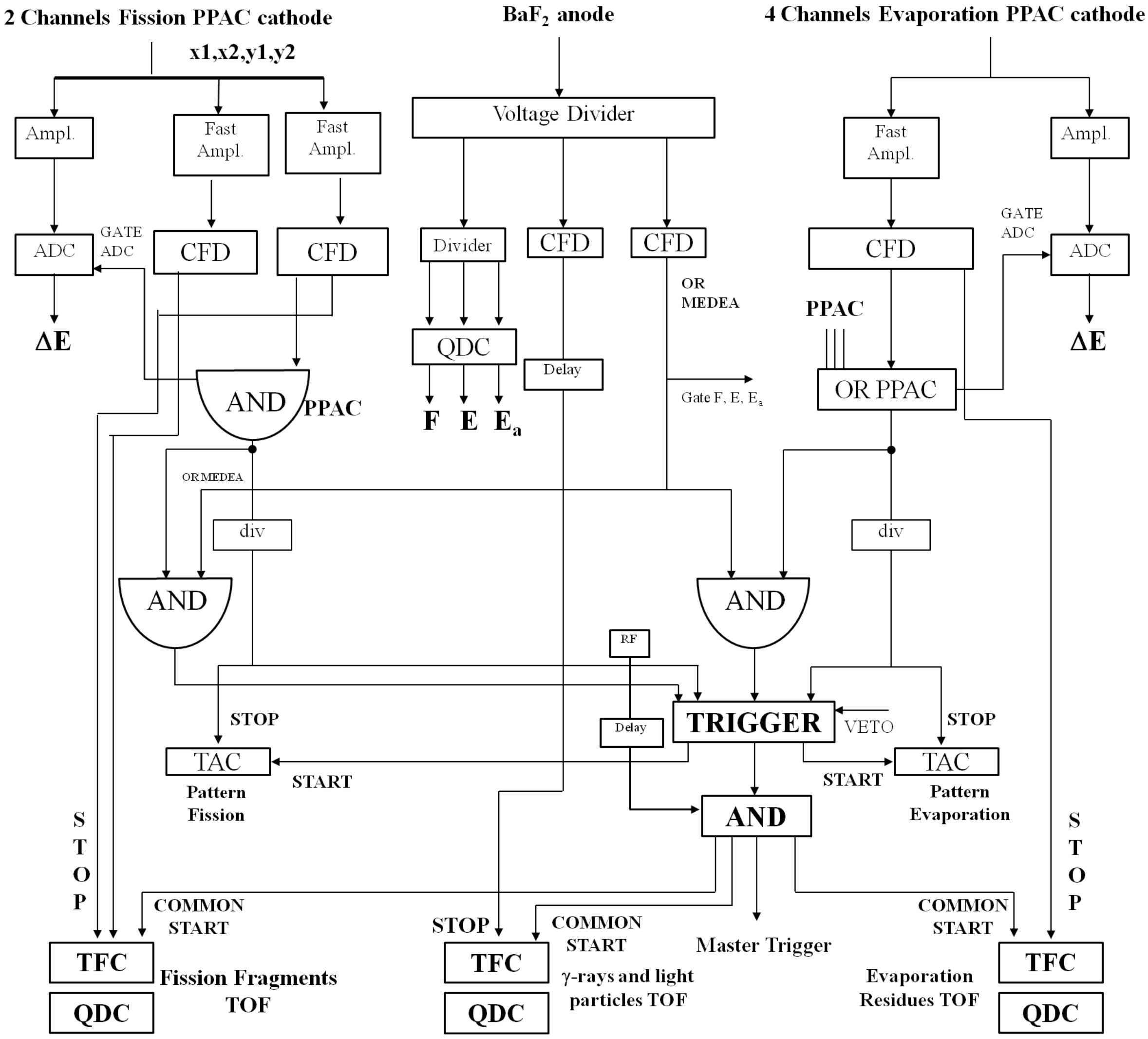

Figure 3.4: *Diagram of the electronic chain connected to the detectors and trigger scheme used for the* $^{40,48}Ca$ + $^{152,144}Sm$ *reactions.*

providing the value of ΔE parameter for each detector. In the second path the signal was sent to a fast amplifier (preserving timing information) and then processed in a constant fraction discriminator (CFD). Here, if the input signal had exceeded a fixed threshold value, CFD activated the STOP signal of a time to Fera Converter (TFC), followed by a charge integrator (FERA QDC), providing the time of flight of the fragments detected with respect to the radiofrequency signal. The logic pulses coming from the CFD of evaporation PPACs were also sent in an OR module; this provided a signal (OR-PPAC-FU) when at least one PPAC recorded a fusion–evaporation event. Regarding fission process, the output signals coming from the CFD were sent to an AND gate, in order to obtain the coincidence between the two kinematic fission fragments (AND-PPAC-FI). Both signals, OR-PPAC-FU and AND-PPAC-FI, were sent to the trigger. While during the experiment, we did not use the x1, x2, y1 and y2 signals of the evaporation residue PPACs giving the position of the reaction products, these signals were used in the case of fission PPACs. The x1,x2, y1 and y2 signals of the fission PPACs were sent to a fast amplifier and then processed in a constant fraction discriminator (CFD). Here, if the input signals had exceeded a fixed threshold value, CFD activated the STOP signal of a time to Fera Converter (TFC), followed by a charge integrator (FERA QDC), providing the time difference between the COMMON START and the time of arrival of the signals (x1,x2, y1 and y2) at each end of the PPAC delay lines (in the orizzontal and vertical direction).

BaF$_2$ electronics

The anode signal of the photomultiplier coupled to each BaF$_2$ of MEDEA was sent to a voltage divider and divided into three parts. The first two partitions were sent to a respective CFD located in the experimental hall close to the scattering chamber. The logic pulse generated by the first CFD was appropriately delayed and sent as STOP in a TFC followed by a QDC in order to get the time of flight of the detected radiation with respect to the radiofrequency. The second one produced a logic signal, called OR-MEDEA, that was sent to the trigger; this signal indicates that at least a BaF$_2$ of the sphere has been fired with a signal larger than the relative electronic threshold.

The third signal, produced by the voltage divider, was, instead, used for energy integration. This signal was split into three outputs with different relative weights:

- **F** (fast) represents 60% of the initial signal and is used for the conversion of the fast component;
- **E** (energy) represents 35% of the original signal and is used for energy conversion in the lower dynamic range (up to 30 MeV);
- $\mathbf{E}_a$ (attenuated energy) constitutes the 5% of the input signal and allows the energy conversion in the higher dynamic range (up to 170 MeV).

These signals were charge integrated with a QDC by adopting two different gates: a *fast* gate 30 ns long for **F** signal and a *total energy* gate 700 ns long for **E** and $\mathbf{E}_a$ conversion. The gate signal integration **F**, **E**, $\mathbf{E}_a$ were provided by the signal OR-MEDEA.

Trigger diagram

The trigger signal was generated after the following events:

1. AND (OR–PPAC–FU – OR–MEDEA): a logic signal generated by the coincidence between an evaporation residue, detected by one PPAC, and a γ or a light particle, detected by a BaF_2 ;
2. OR–PPAC–FU/div: a logic signal coming from one evaporation PPAC, which corresponds to the number of events in single, scaled by a factor using a divider;
3. AND (AND–PPAC–FI – OR–MEDEA): a logic signal generated by the coincidence of two fission fragments detected by PPACs, in coincidence with a BaF_2 signal;
4. AND–PPAC–FI/div: a logic signal coming from the coincidence between two fission PPACs, scaled by a factor by means of a divider.

Lines 1) and 3) enable the acquisition of coincidence events between a BaF_2 and one(two) PPAC for evaporation (fission) events, while lines 2) and 4) are used to acquire single events for both evaporation and fission. The acquisition of single events allows to obtain the double differential multiplicity in energy and solid angle of the γ–rays , avoiding any normalization factor between the spectra. This is a very great advantage for exclusive measurements, as in our case. In the following it is shown the multiplicity expression:

$$\frac{d^2 M_\gamma}{dE_\gamma \, d\Omega_\gamma} = \frac{d^3 N_\gamma}{dE_\gamma \, d\Omega_\gamma \, d\Omega_{ppac}} \cdot \left(\frac{dN_{lib,ppac}}{d\Omega_{ppac}} \right)^{-1} \tag{3.2}$$

where dN_γ is the number of γ–rays detected in fusion–evaporation or fission events, $\frac{dN_{lib,ppac}}{d\Omega_{ppac}}$ represents the number of evaporation or fission events (depending on the considered process) per solid angle, $d\Omega_\gamma$ is the solid angle covered by the BaF_2 and $d\Omega_{PPAC}$ the solid angle covered by the PPAC.

The expression 3.2 gives the number of γ–rays emitted in the solid angle dΩ_γ with an energy between E_γ and $E_\gamma + dE_\gamma$ for an event of fusion-evaporation or fission.

The rate of single events was very high compared to those of coincidence. To avoid increasing of dead time during data acquisition, only a fraction (1/div) of the detected events was acquired. For both reactions ^{40,48}Ca + ^{152,144}Sm , we set div = 999 for evaporation and div = 50 for fission. Once an event was accepted, the acquisition system sent a VETO signal to the trigger, preventing it from accepting other input signals till the end of the acquisition.

The trigger signal was also used to define the PATTERN spectra, useful to calculate the number of single events for PPACs. For this purpose, two *Time to Analog Converter* (TAC) modules (one for the evaporation and one for the fission) were used and received the trigger signal as START. The STOP signal was supplied by OR–PPAC–FU/div to the first TAC (for evaporation), while AND–PPAC-FI/div was sent to the second one (for fission); both signals were appropriately delayed. If the acquisition was triggered by OR–PPAC/div or AND–PPAC–FI/div, a count was incremented in the peak of the corresponding process; while in the case of PPAC-BaF_2 coincidence event, the TAC produced an *overflow* in the PATTERN spectra, since it had not received a STOP signal. The number of PPAC single events divided by the factor div corresponds to the sum of counts present under the peak.

3.4 Data reduction

The data acquisition had a total duration of 10 days for each of the two reactions. The acquisition was divided into several runs, about 100 for each reaction. The data analysis presented in this thesis was carried out with the help of the *framework* **ROOT** [97].

3.4.1 Calibration of BaF_2 detectors

The energy calibration of each BaF_2 detector was done with three different γ–ray sources in order to cover a reliable energy range: a ^{241}Am + ^{9}Be source, whose γ–rays, of energy equal to 4.43 MeV are emitted by the de-excitation of carbon in the reaction ^{9}Be (α, n) ^{12}C*; a ^{238}Pu + ^{13}C source, which provides the point at an intermediate energy of 6.13 MeV thanks to the reaction ^{13}C (α, n) ^{16}O* and finally, the high-energy point, 15.1 MeV, from the decay of ^{12}C* produced in the reaction p + ^{12}C, with a proton beam impinging on a 200μg thick target of ^{12}C at an incident energy E_p = 25 MeV.

The energy spectra of the γ–ray sources were fitted in order to find the energy calibration of BaF_2 . In order to fit the spectra of the γ of the low-enery sources, corresponding to 4.43 and 6.13 MeV, we used a combination of functions: an exponential curve for neutron emission and three gaussian curves, one for the photopeak (4.43 MeV or 6.13 MeV) and the remaining two for the first and the second escape peaks ((4.43(6.13) -0.511) and (4.43(6.13) - 2$*$0.511) MeV respectively). For the high-energy point 15.1 MeV, the spectrum was fitted only with the sum of an exponential function and a gaussian photopeak. Figure 3.5 shows the spectrum of the 4.43 MeV source detected by a BaF_2 ; in this case there is also a contribution (depicted by a magenta line) produced by neutrons and γ pile–up. Once the energy spectra of the γ–ray sources were fitted, the energy calibration, i.e. the relation between the energy lost by the incident radiation on the BaF_2 and a channel of QDC

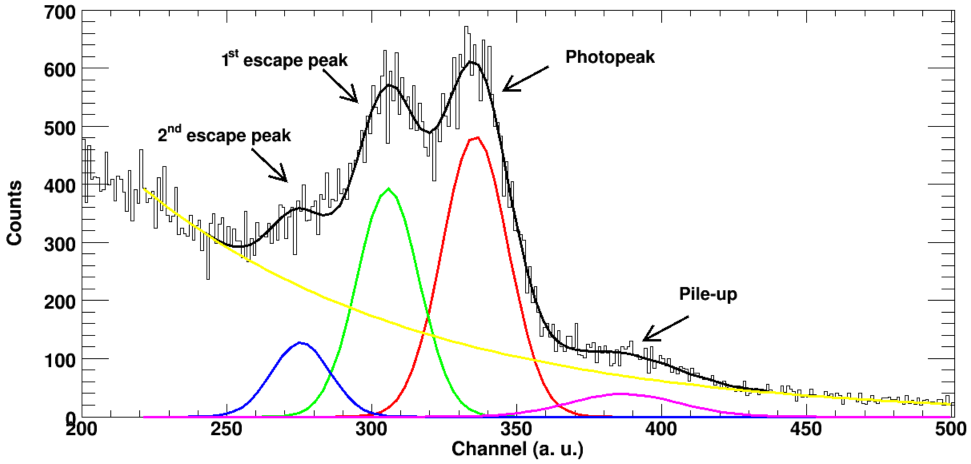

Figure 3.5: *γ–ray spectrum of the ^{241}Am + ^{9}Be source detected by a BaF$_2$. The lines describe the performed fit; more details are avalaible in the text.*

where this information is recorded, was derived with a linear fit, as shown in figure 3.6.

The calibration for the low-energy dynamic range, **E**, was extended to the $\mathbf{E}_a$ one with a simple prescription [98]: $A = (slope \cdot a)$ and $B = (off \cdot a + b)$, where a, b and A, B are the calibration coefficients for **E** and $\mathbf{E}_a$ dynamic ranges, rispectively, while *slope* and *off* are coefficients that connect the two dynamic ranges with this relation $ch = (slope \cdot cha + off)$. This expression was determined from the (ch, cha) bidmensional plot, where ch and cha stand for channels where energy centroids of the sources were observed for **E** and $\mathbf{E}_a$ dynamic range, respectively. The light charged particle calibration was deduced from the γ–ray one by adopting the prescriptions described in [98]. During the experiment the calibration procedure was repeated several times, so as to check and evaluate any change in time.

3.4.2 Signal Identification

BaF$_2$ scintillators are able to detect γ–rays , neutrons and light particles, therefore it is important to clearly distinguish among them. The discrimination between γ–rays , neutrons and light particles detected by the BaF$_2$

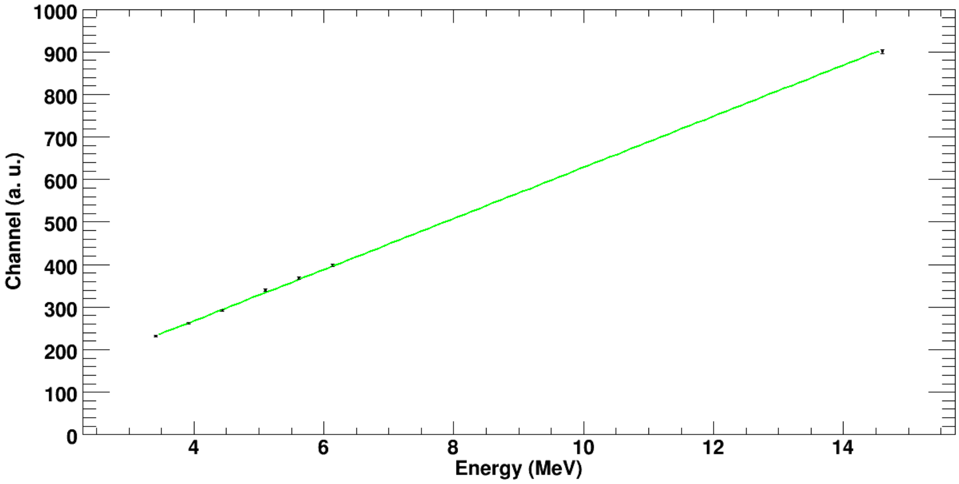

Figure 3.6: *Linear fit for the energy calibration of a* BaF_2 *scintillator.*

was performed by combining a pulse shape analysis of the BaF_2 signal with a ToF measurement of the detected radiation.

Regarding events detected by PPACs, the reaction products were identified, even in this case, thanks to the ToF technique. The time calibration of the spectra was obtained from the distance between the peaks corresponding to the elastic scattering of the projectile from the target caused by two beam bunches separated by 150 ns, in selected runs where the electronic threshold of the ΔE signal was set very low.

3.4.3 Analysis of the BaF_2 detectors

As previously written, the discrimination between γ and the light charged particles was carried out through an off-line analysis of the shape of the output signal of each BaF_2 . This method is based on the integration of each of these signals through two separate gates (see section 3.3) which allows to distinguish between the output signal of the total (**E**) and the fast component (**F**) of the signal itself.

In figure 3.7 “Fast component vs Total energy” bidimensional plot is shown, obtained in the low-energy dynamic range **E** for a BaF_2 placed at θ=97°, with respect to the beam direction, in the reaction ^{48}Ca + ^{144}Sm .

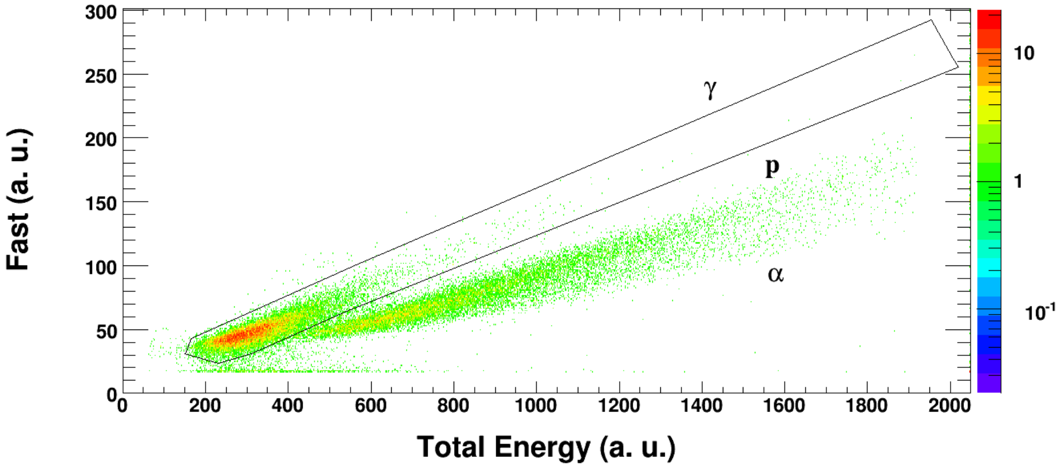

Figure 3.7: *Fast component vs Total energy bidimensional plot for a BaF_2 placed in the ring centered at $\theta = 97°$ for the reaction ^{48}Ca + ^{144}Sm .*

The relative amount of these two components of the signal is a function of the incident radiation (see Section 2.1.2). This relation assumes the maximum value for γ–rays and decreases for light charged particles, as their charge Z increases. Applying a contour, as shown in Fig. 3.7, it is possible to obtain for each crystal a clear separation between γ and light charged particles.

Regarding neutrons, one has to take into account that their interaction with the scintillating material changes as their energy varies. The neutrons interact with the BaF_2 crystals through (n,γ), (n, n'γ) and (n,p) reactions. The first two processes are dominant for low-energy neutrons ($E_n \leq 20$ MeV) and produce γ–rays [99], while high-energy neutrons ($E_n > 20$ MeV) give signals similar to those of protons. So for energies $E_n \leq 20$ MeV neutron signals are within γ–rays contour, while for energies $E_n > 20$ MeV they populate the same zone as protons.

Fast neutrons are discarded by simply selecting the events belonging to the γ contour defined in Fig. 3.7. Slow neutrons, however, are separated from γ–rays through a measurement of their time of flight. At the top of figure 3.8 (top) the "ToF vs Total energy" bidimensional plot for a BaF_2 belonging to the 97° ring in the reaction ^{48}Ca + ^{144}Sm is shown, while in the bottom there

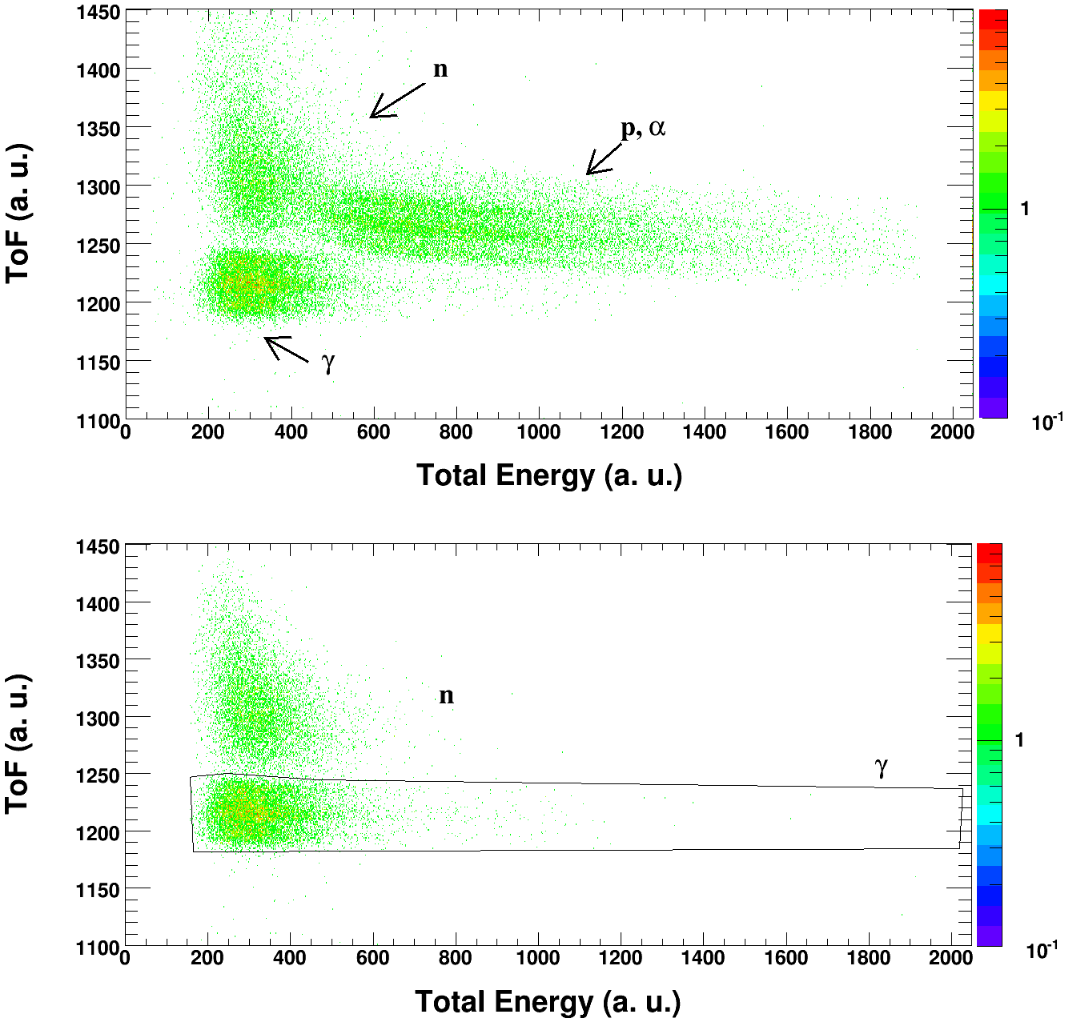

Figure 3.8: *(Top) Time of fligth vs Total energy bidimensional plot obtained for a BaF$_2$ placed at θ=97° for the reaction ^{48}Ca + ^{144}Sm ; (bottom) the same plot as on the top, after conditioning with the γ contour plotted in 3.7. Here it is also drawn another contour to discriminate γ–rays from slow neutrons.*

is the same plot, conditioned by the γ contour drawn in figure 3.7. In this way, it is possible to make a contour around the γ–rays area to discriminate them from slow neutrons, after discarding charged particles and fast neutrons with the contour in the Fast component vs Total energy bidimensional plot. It seems clear then the great advantage obtained by carrying out a division of the BaF$_2$ signal into three components (see section 3.3).

In order to identify γ–rays , only those events that fell simultaneously within the corresponding contours, show in figures 3.7 and 3.8, were considered in the analysis. This technique was applied to all BaF$_2$ detectors of MEDEA apparatus to select, not only γ, but also proton and α events for both energy ranges ($\mathbf{E}$ and $\mathbf{E}_a$), as shown in the following.

3.4.4 Analysis of the PPAC detectors

PPAC detectors for fusion–evaporation

Figure 3.9 shows the energy loss ΔE vs ToF bidimensional plot, for one of the four PPAC used for the reaction ^{48}Ca + ^{144}Sm to detect evaporation residues.

In this plot both down scaled single and coincidence events with BaF$_2$ signals are shown. We can use some simple physical considerations to identify and distinguish different reaction mechanisms, that will be discussed below.

Let us consider the reaction ^{48}Ca + ^{144}Sm where a ^{48}Ca beam is impinging on the ^{144}Sm oxide target with an incident energy of E_{lab} = 485 MeV, with the hypothesis that the reaction takes place at the middle of the target. First, we evaluated the energy of the projectile, after passing through the first middle of the target, with **LISE++** program [100] : E_{pr} = 481.1 MeV, which corresponds to a velocity of 4.4 cm/ns. Events due to the elastic scattering of the projectile were detected at $\theta = 7°$, after travelled a distance d = 70 cm between the target and detector in a time of 15.2 ns; their energy loss inside the gas of the PPAC detector (iso-C_4H_{10} P = 9.2 Torr, d = 2.400μm) is ΔE = 0.12 MeV. These events are therefore characterized by short time of flight and low energy losses and therefore they are located in the lower, left-hand site of the plot in Fig. 3.9. These events are cut by the electronic threshold of the ΔE signal, however, at the relative ToF position we observe pile up events

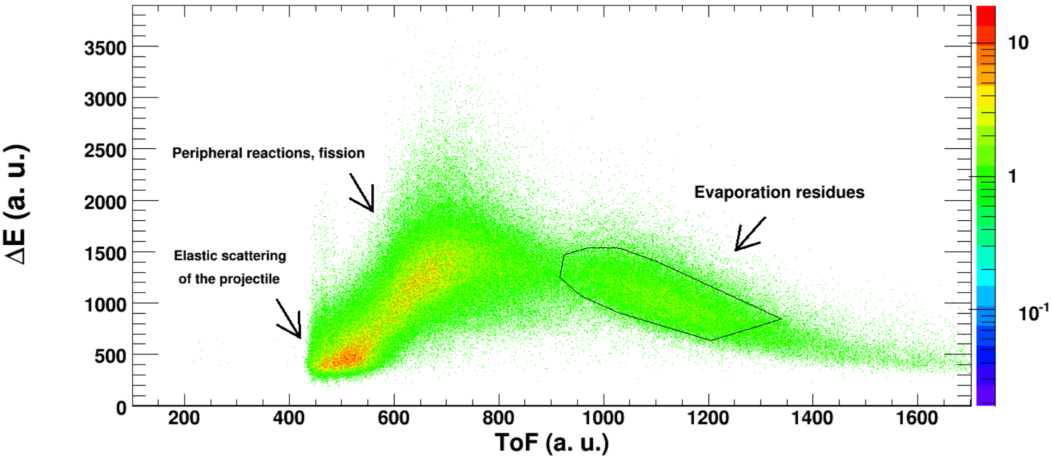

Figure 3.9: ΔE - *ToF bidimensional plot for fragments detected in one of the PPAC fusion–evaporation (single and coincidence events) for the reaction* $^{48}Ca + ^{144}Sm$ *at* E_{lab} *= 10.1 MeV/nucleon.*

due to the high counting rate of elastically scattered projectiles. Also the elastic scattering of ^{144}Sm events were detected: they arrived to the gaseous detectors after 32.9 ns and, due to their heavier mass and charge, with higher energy loss in the gas, ΔE = 0.8 MeV. Hence these events are located in the upper part of the figure 3.9 and at the right of the elastic scattering of ^{48}Ca. In our target there is also ^{16}O, but, in case of scattering, its energy loss is very low, below the energy threshold chosen for ΔE; therefore these events are completely excluded.

After a fusion reaction, the evaporation residues of the ^{192}Pb CN can be detected by PPACs. Supposing that the particle evaporation doesn't change much the velocity and the direction of the residue, we can calculate its kinetic energy as:

$$E_{residue} \approx E_{CM} = \frac{A_p}{A_p + A_t} \cdot E_{pr} = 120.3\ MeV \tag{3.3}$$

where A$_p$ and A$_t$ are the mass number of projetcile and target, respectively. Hence the CN has a velocity equal to 1.1 cm/ns, corresponding to a time of flight of 63.6 ns.

For evaporation residues produced after fusion reaction, one must take into account the non-negligible energy loss inside the target, due to the high value of their charge and mass. Let us consider the most probable evaporation residue, ^{172}Os, calculated with PACE4; it has an average energy E_{res} = 107.8 MeV (equivalent to a velocity of 1.1 cm/ns), therefore its energy loss before reaching the detector is E_{loss} = 13.9 MeV. At the exit from the target, the evaporation residue then presents an energy equal to 93.9 MeV. Its velocity is equal to 1.03 cm/ns, so the time taken to travel the distance target - PPAC is equal to 68.0 ns. It is expected, therefore, to observe the events corresponding to the two different mechanism reaction (elastic scattering and fusion–evaporation) at an average temporal distance of $\sim$ 52.8 ns.

The intermediate region, with time of flight between that of elastic scattering of ^{48}Ca and those of evaporation residues, is populated by peripheral reactions (like ^{144}Sm scattering) and/or fusion–fission reactions. Considering the kinematics of the process, symmetric fission fragments are emitted, at the exit of the target, with a velocity of v_{FF} = 2.25 cm/ns, equivalent to a time of flight of 31.2 ns. Hence these events are temporally located before the elastic and inelastic scattering of ^{144}Sm, with a lower energy loss, ΔE = 0.55 MeV. After taking into account the time calibration (see section 3.4.2), we found that fusion-evaporation events reach the maximum yield for high energy loss, while as time of flight becomes longer, as the percentage of transferred linear momentum decreases.

During the analysis only the evaporation residues included within the contour drawn in Figure 3.9 were considered. Their average velocity is about 96% of the center-of-mass velocity for the ^{48}Ca + ^{144}Sm reaction and 98% for the ^{40}Ca + ^{152}Sm one.

PPAC detectors for fission

In picture 3.10 it is shown the ΔE vs ToF bidimensional plot for one of two PPACs, placed at $\theta = 52.5°$, for the detection of fission fragments for the reaction ^{48}Ca + ^{144}Sm. Thanks to simple arguments, as done for fusion–evaporation, we can characterize the different reaction mechanisms presented in this plot.

Let us consider again the reaction ^{48}Ca + ^{144}Sm (E_{lab} = 485 MeV). The

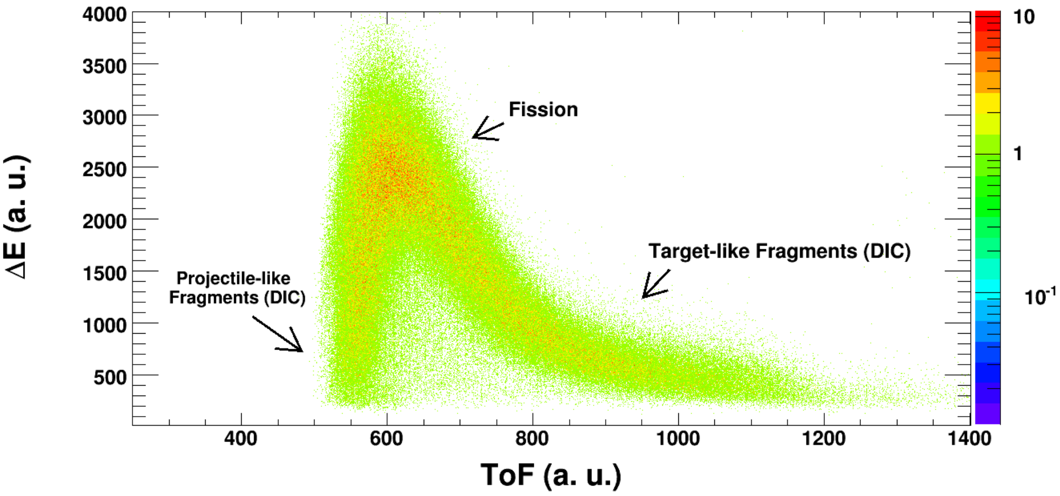

Figure 3.10: *ΔE -ToF bidimensional plot of one of the two PPACs used to detect fission fragments, in the reaction $^{48}Ca + ^{144}Sm$ $E_{lab} = 10.1$ MeV/nucleon. Both singles and coincidence events are considered.*

projectile was elastically scattered at an energy of 7.55 MeV/nucleon, equivalent to a velocity 3.8 cm/ns and thus arrived to PPAC, at 16 cm from the target, after 4.2 ns; its energy loss in the gas (iso-C_4H_{10} P = 9.2 Torr, d = 2400μm) inside the PPAC was 0.14 MeV. These events were cut with the electronic threshold of the ΔE signal. At low energy losses and small time of flight, there are, not so far from the elastically scattered ^{48}Ca, fragments with charge and mass similar to those of the projectile *Projectile - like fragments*, scattered inelastically from the target. Going to higher energy losses, there are other fragments similar to the projectile, produced by deeply inelastic processes (**D**eep **I**nelastic **C**ollisions, DIC).

Events corresponding to the elastic scattering of ^{144}Sm were detected at $\theta = 52.5°$ after 13.1 ns from the beginning of the reaction. Its energy loss was 0.61 MeV in the gas contained in the detector, so these events are located in the upper and right-hand side of the plot. In the bottom and right of the picture 3.10 there are ions with mass and charge close to those of the target, *Target - like Fragments*, originating from a deep inelastic collision and having a very low velocity, i.e. with very long time of flight. The events corresponding to an interaction with ^{16}O of target are excluded, as for fusion–

evaporation PPAC, due to their very low energy loss.

Fission fragments, coming from both symmetric and asymmetric fission process, exited from the target at an average velocity of 1.5 cm/ns and reached the detector in 10.6 ns, loosing about 0.5 MeV inside the gas. These events are so placed in the upper part of the ΔE-ToF plot.

In order to select fission fragments, we used a contour as shown in Figure 3.11 for both fired PPACs. During the analysis only those events that fell within the contour drawn in figure 3.11 of both PPACs simultaneously were considered. In this way it has been possible to avoid any contribution due to other processes, such as the elastic scattering of the target, which is placed not far away from fission products, or other direct and less dissipative processes.

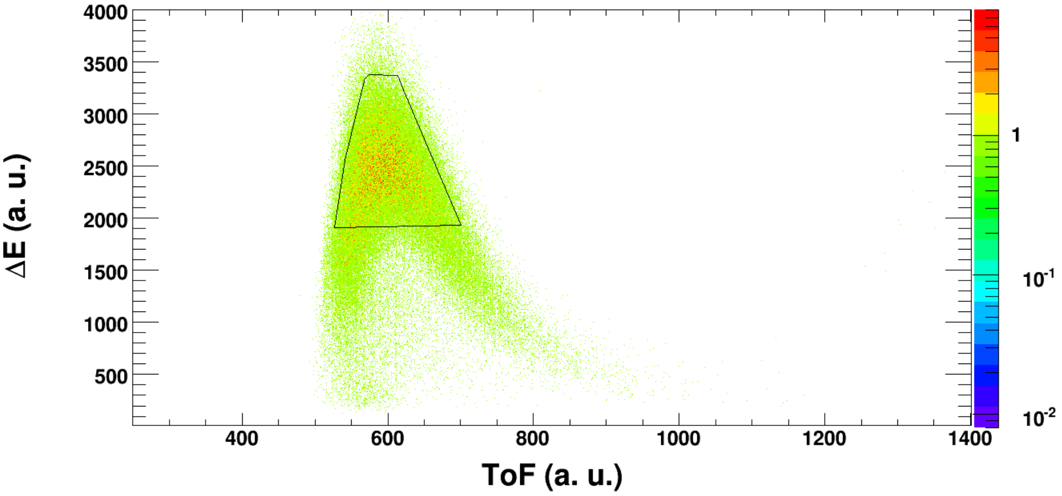

Figure 3.11: ΔE - *ToF bidimensional plot for events with multiplicity 2 (i.e. events in coincidence between two PPACs), detected in a PPAC at* $\theta = 52.5°$*, for the reaction* ^{48}*Ca +* ^{144}*Sm at* E_{lab} *= 10.1 MeV/nucleon. It is also shown a contour, used to select fission fragments events.*

Chapter 4

Fusion–evaporation: data analysis and results

4.1 Pre–equilibrium particle emission

In the design phase of the experiment, the incident energies were chosen in such a way as to obtain the same excitation energy of the compound system in both reactions, after taking into account the energy loss, due to the emission of pre–equilibrium particles, as shown in section 3.1. This emission takes place before the system has reached the thermodynamic equilibrium, leading to a decrease in excitation energy, mass and charge of the CN. Inclusive measurements of light particles, carried out within a wide range of incident energies and with different combinations projectile - target, have shown that the emission of pre-equilibrium particles does not depend on the detailed structure of the two colliding ions, but on the excess of incident energy compared with the Coulomb barrier ([101] and references therein).

The experimental setup MEDEA allowed, however, to verify experimentally the validity of this assessment through the detection of light charged particles. Therefore we evaluated the excitation energy of the CN by analysing the double differential multiplicity in energy and solid angle spectra of protons and α-particles detected by the BaF_2 scintillators in coincidence with the evaporation residues detected by PPACs in both reactions, while the pre-equilibrium neutron emission was estimated from our proton data and from existing neutron emission studies ([102] and references therein).

4.1.1 Charged particle energy spectra

The double differential multiplicity in energy and solid angle of the emitted protons and α-particles following the two fusion reactions can be calculated, in analogy to (3.2), as:

$$\frac{d^2 M_{particle}}{dE_{particle}\, d\Omega_{particle}} = \frac{d^3 N_{particle}}{dE_{particle}\, d\Omega_{particle}\, d\Omega_{ppac}} \cdot \left(\frac{dN_{lib,ppac}}{d\Omega_{ppac}} \right)^{-1} \tag{4.1}$$

after selecting events corresponding to the detection of a light charged particle from the plot of discrimination of each BaF_2 (as described in section 3.4.3) and the detection of evaporation residues from the plot ΔE-ToF of each PPAC (Section 3.4.4).

These spectra measured in coincidence with the evaporation residues for both systems were extracted for several polar angles, ranging from 51° to 160°, with respect to the incident beam direction.

In general, the emission of light particles in fusion reactions is mainly due to three distinct processes: 1) the statistical evaporation from the CN, 2) the statistical evaporation from the remaining *projectile - like*, 3) non-statistical emission resulting from nucleon - nucleon collisions that takes place in the very early stages of the reaction [103] and/or pre–equilibrium particles emitted before a full thermalization of the composed system.

It is possible to evaluate the contribution of each source in the total particle spectra with a moving source fit in which the particles are assumed to be emitted isotropically from three moving sources.

The first and the last contribution are generally fitted respectively with a *slow* source having $v = v_{CN}$ and an *intermediate velocity* source with a velocity between $v = v_{CN}$ and v_{beam}; the *projectile - like*, however, is moving at a velocity close to that of the projectile and is characterized by a low apparent temperature and, therefore, gives a contribution to the multiplicity of particles preferentially at very forward angles, in an angular range that was not investigated in this experiment. Therefore our charged particle spectra

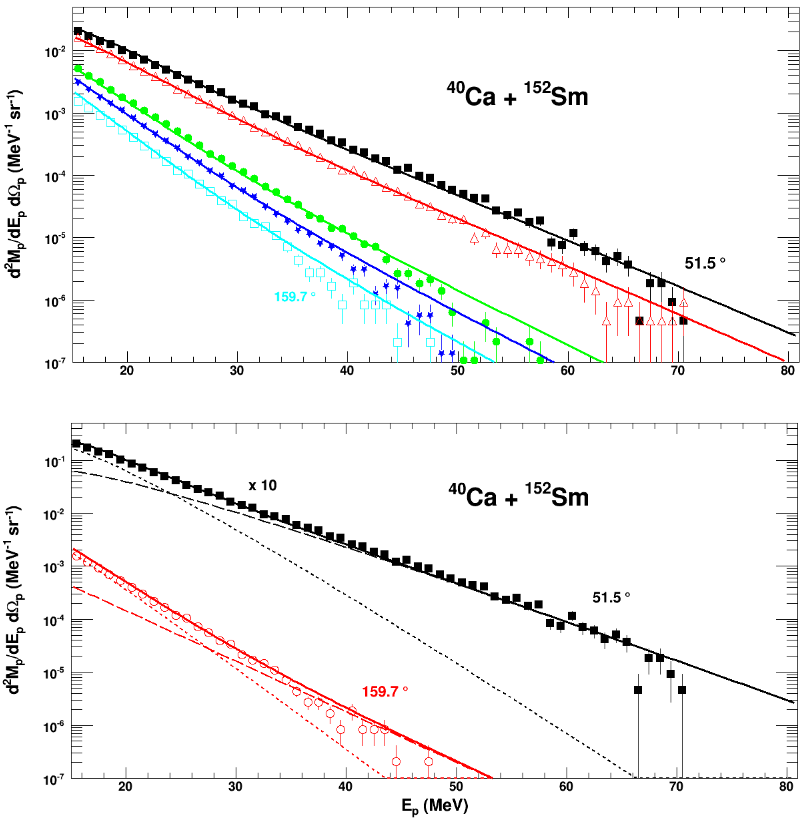

Figure 4.1: *(Top) Laboratory proton energy spectra obtained at various angles in coincidence with the fusionlike residues for the reactions* $^{40}Ca + {}^{152}Sm$ *. The angles are* 51.5°, 68.1°, 111.9°, 128.5° *and* 159.7°*. The solid lines show the results of the simultaneous fits described in the text. (Bottom) Laboratory proton energy spectra at two angles. The solid lines are the results of the fits with two sources. The long-dashed and dotted lines represent the intermediate-velocity source and the slow source components, respectively.*

can be fitted using only two sources: the CN and the intermediate velocity source.

The energy distribution of the evaporated particles was parameterized, in the source rest frame, adopting a surface-type Maxwellian distribution given by:

$$\left(\frac{d^2M}{d\Omega dE}\right)_{sl} = \frac{M_{sl}}{4\pi T_{sl}^2}\,(E - E_c)\,exp\left[-\frac{(E-E_c)}{T_{sl}}\right] \tag{4.2}$$

while the distribution of the pre-equilibrium particles was taken to be that for volume emission from a thermal source:

$$\left(\frac{d^2M}{d\Omega dE}\right)_{int} = \frac{M_{int}}{2(\pi T_{int})^{3/2}}\,\sqrt{E-E_c}\,exp\left[-\frac{(E-E_c)}{T_{int}}\right] \tag{4.3}$$

where E is the particle energy, E_c is the Coulomb barrier for particle emission, T_i (i is for sl or int) is the apparent source temperature, and M_i is the multiplicity of the particles emitted from the i source. Both Maxwellian distributions were transformed in the laboratory reference frame using the relation:

$$\left(\frac{d^2M}{d\Omega dE}\right)_{lab} = \sqrt{\frac{E_{lab}}{E'}}\left(\frac{d^2M}{d\Omega dE}\right)_{E\equiv E'} \tag{4.4}$$

where the particle energy E' in the source reference frame is given by:

$$E' = E_{lab} + E_s - 2\,\sqrt{E_{lab}\;E_s}\,cos\theta_{lab} \tag{4.5}$$

with E_s equal to the kinetic energy of a particle moving with the source velocity, assumed to be parallel to the beam axis and θ_{lab} is the observation angle of the particle.

The evaporative source velocity was fixed to a value equal to 98% and 96% of the center-of-mass velocity, namely v_{sl} = 0.94 cm/ns and 1.06 cm/ns for the system ^{40}Ca + ^{152}Sm and ^{48}Ca + ^{144}Sm , respectively, as determined by the calibration of the PPAC's TOF spectra. The remaining five parameters were considered as free variables in the fitting procedure. It was found that

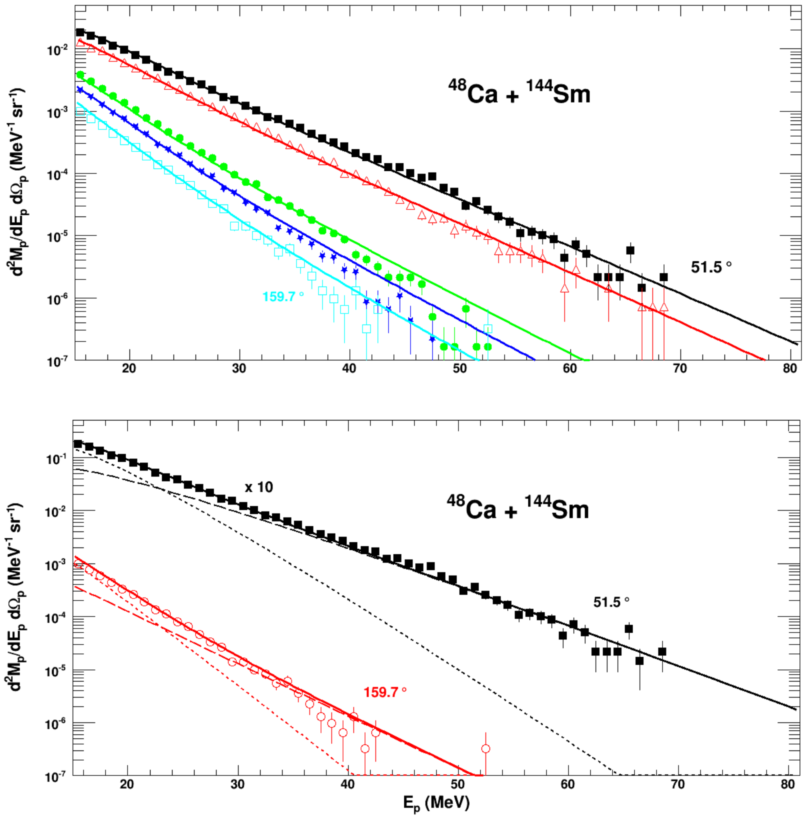

Figure 4.2: *Same as in Figure 4.1 for* ^{48}Ca + ^{144}Sm *reaction.*

the data could be fitted with the same value of the Coulomb barrier E_c for both sources. It was fixed E_c=6 MeV for protons and E_c=15 MeV for α particles. However, the sensitivity of the fit to reasonable changes of the Coulomb barrier is small.

The results of the simultaneous fit are shown with solid lines in the top of Figure 4.1 and Figure 4.2 for protons and Figure 4.3 and Figure 4.4 for α particles, respectively. Rings placed at 82.8° and 97.1° were not used since low-energy particles emitted at $\theta_{lab} = 90°$ are largely stopped in the target which was oriented normal to the beam axis. The relative contributions of the two sources are reported in the bottom of the same pictures for a backward and a forward ring, with the *slow* (*intermediate-velocity*) source component represented with a long-dashed (dotted) line. The pre-equilibrium source gives a relevant contribution, as expected, especially at forward angles at high energy.

The parameters extracted from the fit, multiplicity and temperature of the *slow* source and multiplicity, temperature and velocity of the *intermediate-velocity* source are reported in Table 4.1 and Table 4.2 for protons and α particles, respectively.

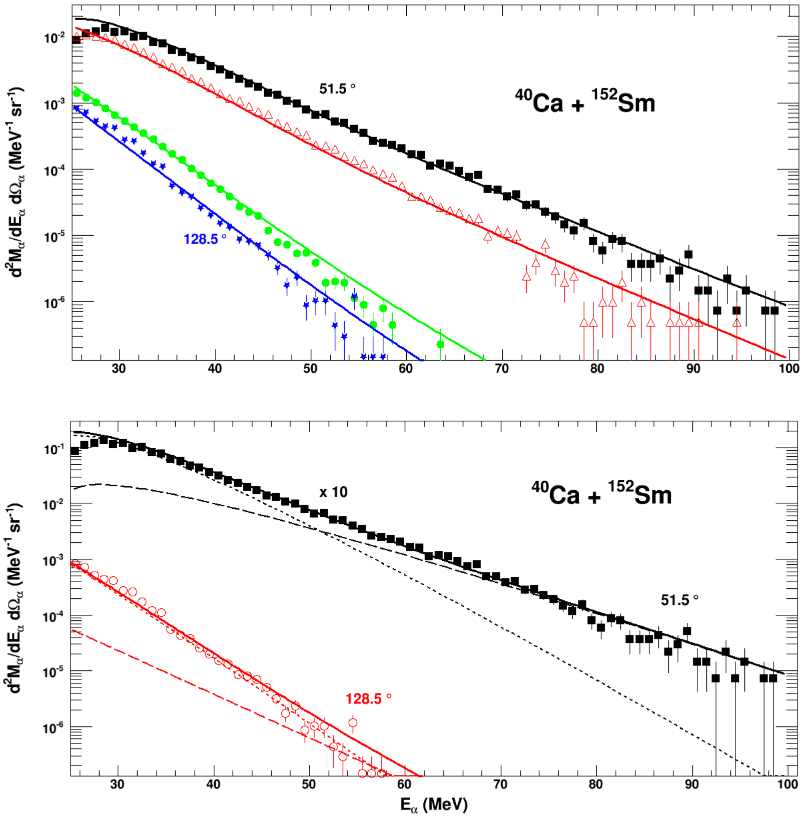

Figure 4.3: *(Top) Laboratory α-particle energy spectra obtained at various angles in coincidence with the fusionlike residues for the reactions $^{40}Ca + ^{152}Sm$. The chosen angles are* 51.5°, 68.1°, 111.9° *and* 128.5°. *The solid lines show the results of the simultaneous fits described in the text. (Bottom) Laboratory α-particle energy spectra at two angles. The solid lines are the results of the fits with two sources. The long-dashed and dotted lines represent the intermediate-velocity source and the slow source components, respectively.*

To evaluate the average energy taken away by pre-equilibrium neutrons, not detected in this experiment, we assumed that their energy spectra were very similar to the proton ones, apart from the Coulomb barrier. Then, the average kinetic energy of a pre-equilibrium neutron was taken to be that of a pre-equilibrium proton minus the Coulomb barrier while the pre-equilibrium neutron multiplicity was deduced by that of pre-equilibrium protons multiplied with the N/Z ratio of the CN. The adopted pre-equilibrium neutron multiplicity, 1.05 ± 0.25 for the^{40}Ca + ^{152}Sm and 1.02 ± 0.25 for the ^{48}Ca + ^{144}Sm reaction, is in agreement within errors with neutron emission studies performed at similar center-of-mass incident energy above the Coulomb barrier [102].

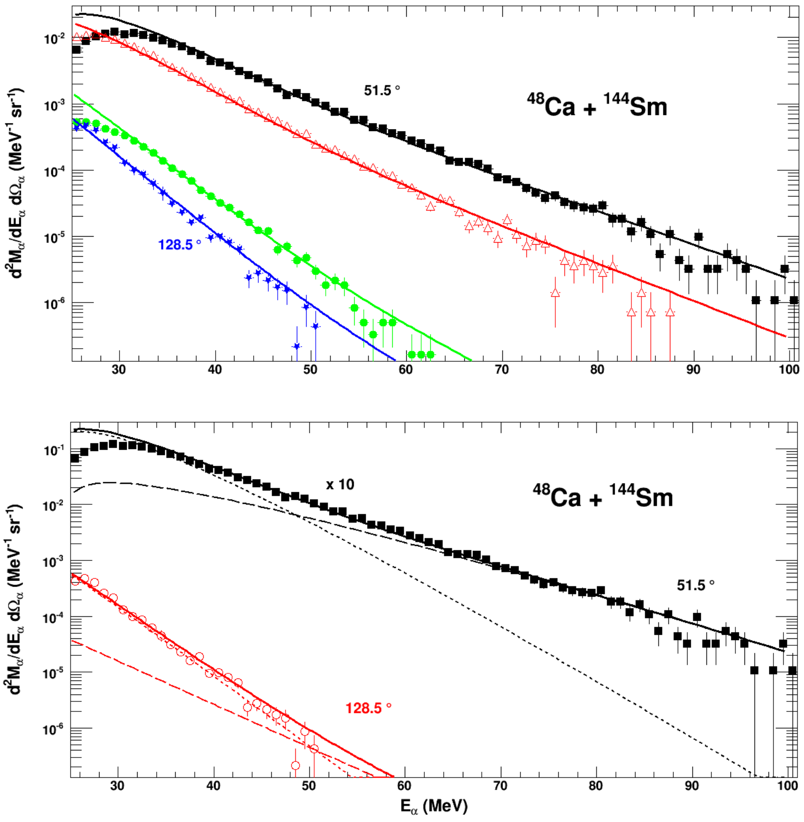

Figure 4.4: *Same as in Figure 4.3 for* ^{48}*Ca* + ^{144}*Sm reaction.*

The values of average kinetic energy, binding energy and energy lost for each pre-equilibrium particle can be seen for the ^{40}Ca + ^{152}Sm and ^{48}Ca + ^{144}Sm reactions in Table 4.3 and Table 4.4, respectively. The average excitation energy of the composite system after pre-equilibrium particle emission E^{*}=E_{CM}+Q_{gg}-E_{lost} with E_{CM} the energy available in the center-of-mass reference frame, Q_{gg} the reaction Q-value and E_{lost} the total energy lost, was deduced to be E^{*}=(220.60 ± 4.76) MeV for the ^{40}Ca + ^{152}Sm and E^{*}=(219.80 ± 4.75) MeV for the ^{48}Ca + ^{144}Sm reaction (see Table 4.5), while its average mass was found to be A = 189 for both reactions. The maximum error in A is less than one unit. Therefore, as the average excitation energy and the average mass of the composite system after pre-equilibrium particle emission are the same within errors for the two reactions, we can proceed in the comparison of their γ–ray spectra, being confident that any difference between them is due to an entrance channel effect.

Table 4.1: Multiplicities, temperatures and velocities of the *slow* and the *intermediate-velocity* sources extracted from the moving source fit for protons emitted in the ^{40}Ca + ^{152}Sm and ^{48}Ca + ^{144}Sm fusion reactions.

Reaction	E$_c$ (MeV)	v_{sl} (cm/ns)	M_{sl}	T_{sl} (MeV)
^{40}Ca + ^{152}Sm	6	0.94	2.25 ± 0.05	2.89 ± 0.03
^{48}Ca + ^{144}Sm	6	1.06	1.84 ± 0.06	2.80 ± 0.04

Reaction	v_{int} (cm/ns)	M_{int}	T_{int} (MeV)
^{40}Ca + ^{152}Sm	1.76 ± 0.05	0.78 ± 0.06	5.10 ± 0.08
^{48}Ca + ^{144}Sm	1.74 ± 0.06	0.76 ± 0.08	4.93 ± 0.10

Table 4.2: Same as in Table 4.1 for α particles.

Reaction	E_c (MeV)	v_{sl} (cm/ns)	M_{sl}	T_{sl} (MeV)
^{40}Ca + ^{152}Sm	15	0.94	1.86 ± 0.09	3.79 ± 0.05
^{48}Ca + ^{144}Sm	15	1.06	2.15 ± 0.08	3.62 ± 0.04

Reaction	v_{int} (cm/ns)	M_{int}	T_{int} (MeV)
^{40}Ca + ^{152}Sm	1.62 ± 0.10	0.28 ± 0.05	6.29 ± 0.21
^{48}Ca + ^{144}Sm	1.91 ± 0.08	0.33 ± 0.04	6.59 ± 0.16

Table 4.3: Average kinetic energy E_k, binding energy E_{bind}, pre-equilibrium particle multiplicity M_{int} and average energy lost E_{lost} for the ^{40}Ca + ^{152}Sm reaction.

Particle	E_k(MeV)	E_{bind}(MeV)	M_{int}	$E_{lost}=M_{int}*[E_k+E_{bind}]$ (MeV)
Proton	13.64 ± 0.11	3.56	0.78 ± 0.06	13.48 ± 0.98
Neutron	7.64 ± 0.11	10.56	1.05 ± 0.25	19.14± 4.56
α	24.43 ± 0.31	-5.0	0.28 ± 0.05	5.53 ± 1.01

Table 4.4: Same as in Table 4.3 for the ^{48}Ca + ^{144}Sm reaction.

Particle	E_k(MeV)	E_{bind}(MeV)	M_{int}	$E_{lost}=M_{int}*[E_k+E_{bind}]$ (MeV)
Proton	13.39 ± 0.16	3.56	0.76 ± 0.08	12.84 ± 1.32
Neutron	7.39 ± 0.16	10.56	1.02 ± 0.25	18.24± 4.49
α	24.89 ± 0.23	-5.0	0.33 ± 0.04	6.61 ± 0.83

Table 4.5: Center-of-mass energy E_{CM}, reaction Q-value Q_{gg}, total energy lost E_{lost} and E^*, obtained after pre-equilibrium emission for both reactions.

Reaction	E_{CM} (MeV)	Q_{gg} (MeV)	E_{lost} (MeV)	E^* (MeV)
^{40}Ca + ^{152}Sm	345.81	87.06	38.15 ± 4.76	220.60 ± 4.76
^{48}Ca + ^{144}Sm	361.12	103.63	37.69 ± 4.75	219.80 ± 4.75

4.2 Analysis of the γ–ray spectra

The results presented in section 4.1.1 ensure that the present experiment was designed properly, since we demonstrated that the CN is formed in both reactions with the same average excitation energy and average mass. The only parameter that differentiates the two reactions is the initial charge asymmetry ($\Delta = 0.45$ for ^{40}Ca + ^{152}Sm and $\Delta = 0.08$ for^{48}Ca + ^{144}Sm). Therefore we can compare safely the results of both reactions and understand how important is the role of the charge asymmetry in the evolution of reaction dynamics.

The γ–ray were selected thanks to the contours applied on the *fast component* - total energy and ToF - total energy bidimensional plots of BaF$_2$ scintillators (as shown in the pictures 3.7 and 3.8) while fusion–evaporation events were selected with the countors applied to the ΔE - ToF bidimensional plot of evaporation PPACs (as in picture 3.9). Then the double differential multiplicity in energy and solid angle was calculated for γ–rays emitted during the fusion–evaporation reactions from the relation (3.2), reported below :

$$\frac{d^2 M_\gamma}{dE_\gamma\, d\Omega_\gamma} = \frac{d^3 N_\gamma}{dE_\gamma\, d\Omega_\gamma\, d\Omega_{ppac}} \cdot \left(\frac{dN_{lib,ppac}}{d\Omega_{ppac}}\right)^{-1} \tag{4.6}$$

4.2.1 Doppler Effect

γ–rays , detected by BaF$_2$ scintillators, are emitted in the laboratory reference frame (LAB) from a source (the CN or an evaporation residue) moving relative to the detectors (considered as observer).

To take into account the Doppler effect, that alters the energy measured in the LAB, γ–rays energy spectra have to be transformed in a reference frame where the emitter nucleus is at rest or in the center of mass reference frame (CM).

Based on kinematic considerations, it is simple to verify the existence of the following expressions :

$$E_{CM} = E_{LAB} \frac{(1 - \beta \cos\theta_{LAB})}{\sqrt{1-\beta^2}} \tag{4.7}$$

$$\sin\theta_{CM} = \sin\theta_{LAB}\frac{\sqrt{1-\beta^2}}{(1-\beta\cos\theta_{LAB})} \tag{4.8}$$

where E_{CM} (E_{LAB}) and θ_{CM} (θ_{LAB}) refer to the energy and polar emission angle of a γ–ray from a BaF_2 , respectively, in the CM (LAB), while $\beta = \frac{v}{c}$ is the velocity v of the source expressed in units of c. From (4.7) and (4.8) follows that:

$$\left(\frac{d^2M_\gamma}{dE_\gamma\, d\Omega_\gamma}\right)_{CM} = \left(\frac{d^2M_\gamma}{dE_\gamma\, d\Omega_\gamma}\right)_{LAB} \cdot \frac{(1-\beta\cos\theta_{LAB})}{\sqrt{1-\beta^2}} \tag{4.9}$$

The expression (4.9) allows to transform the laboratory γ–rays energy spectra detected by every BaF_2 in the center of mass reference frame of the nucleus emitter. We are assuming that the CN evaporation does not alter significantly the module and the direction of the emitting source velocity; this is equivalent to consider the CN as the main nucleus emitter. This assumption is valid for γ–rays of energy greater than $\sim$ 10 MeV, while γ–rays at lower energies are emitted preferentially in the final part of the cascade decay. In this way, therefore, an uncertainty on the slope of the experimental spectrum is introduced.

In the experiment under consideration, the reactions ^{40}Ca + ^{152}Sm and ^{48}Ca + ^{144}Sm were performed at the effective incident energies of 436.81 MeV and 481.10 MeV (taking into account the energy loss in the target using (3.3) to calculate the kinetic energy of the CN); then β values were found to be equal to 0.032 and 0.037 for the ^{40}Ca + ^{152}Sm and ^{48}Ca + ^{144}Sm reactions, respectively.

4.2.2 Evaluation of the Bremsstrahlung contribution

At these incident energies it can not be neglected the contribution of the incoherent nucleon-nucleon bremsstrahlung component to the γ–ray multiplicity spectra. This component is originated primarily in neutron-proton (np) collisions and is dominant for $E_\gamma > 35$ MeV [104]. The purpose of this section is to show how to evaluate quantitatively the bremsstrahlung component and then to subtract it from the experimental γ–ray spectra.

An equal bremsstrahlung component is expected for both reactions because of their very similar beam energy and size of the reaction partners and of the same temperature of the composite system (see [105] and references therein). Because this component of the spectrum is equal in both reactions, its subtraction from the data is necessary for the study of the spectrum and angular distribution of the γ–rays emitted in each reaction, presented in the following, but it does not affect the spectrum and the angular distribution referring to the difference between the data of the two reactions.

The following expression describes the behaviour of high energy γ–rays emitted in nucleon - nucleon bremsstrahlung processes in coincidence with the evaporation residues in the nucleon-nucleon center-of-mass reference frame:

$$\frac{dM_\gamma}{dE_\gamma} = \int\limits_{4\pi} \frac{d^2M_\gamma}{dE_\gamma\, d\Omega_\gamma}\, d\Omega_\gamma = 4\pi\, \frac{A_\gamma}{E_0}\, exp\left(-\frac{E_\gamma}{E_0}\right) = N_\gamma\, exp\left(-\frac{E_\gamma}{E_0}\right) \tag{4.10}$$

The inverse slope of the spectra, E_0, for both reactions was determined experimentally by fitting simultaneously the data obtained from the rings centered $\theta_{lab} = 82.8°$ and $97.1°$ shown in figure 4.5 for energies E_γ >30 MeV. Its value was found to be $E_0 = (7.5 \pm 2.2)$ MeV, in good agreement with the systematic known for nucleon - nucleon bremsstrahlung [104]. The results of the simultaneous fits are shown with the solid line in Fig. 4.5.

The high energy γ–rays due to bremsstrahlung dominate to the experimental γ–rays spectra in the range of $E_\gamma > 35$ MeV but give also a contribution ar lower energies. From both theoretical [106,107] and experimental [108] point of view, an exponential behaviour of the bremsstrahlung component is a reasonable approximation for energies below 35 MeV, up to $E_\gamma \approx$20 MeV. For $E_\gamma < 20$ MeV the assumption of an exponential behaviour is less certain. However, as mentioned previously, the bremsstrahlung component at the present incident energy it accounts for 16% of the total yield at E_γ=20 MeV, 4% of the total yield at E_γ=15 MeV while it accounts for 1.5% at E_γ=10 MeV. The above statements show that its influence in the energy region of interest should be small. Therefore, an exponential behaviour of the bremsstrahlung component was also assumed for energies lower than 20 MeV.

The bremsstrahlung component obtained at θ_{lab} = 82.8°, 97.1°, where the Doppler correction is negligible, was deduced also at the other polar angles taking into account the Doppler effect (see section 4.2.1) and it was subtracted from the corresponding experimental spectra.

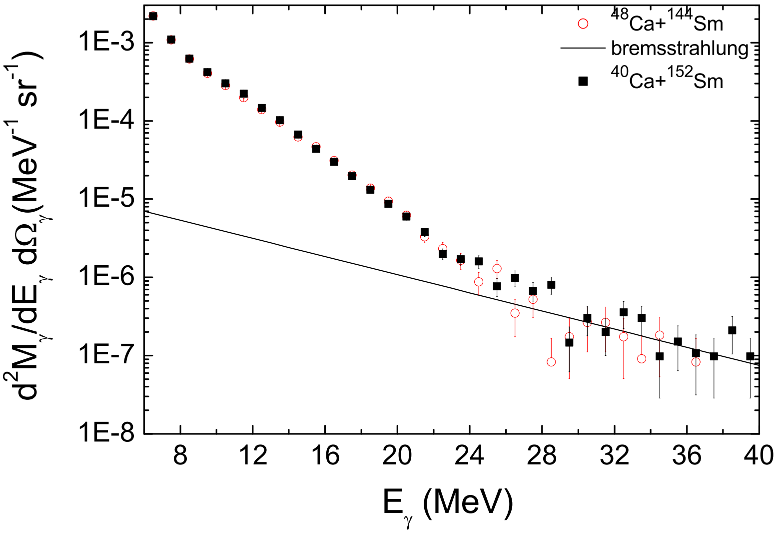

Figure 4.5: *Experimental γ–ray spectra detected at θ_{lab} = 82.8°, 97.1° emitted during the ^{48}Ca + ^{144}Sm (open circles) and ^{40}Ca + ^{152}Sm (red squares) fusion–evaporation reactions. The solid line describes the nucleon - nucleon bremsstrahlung component, obtained with the simultaneous fit of the spectra.*

4.2.3 γ–ray spectra and angular distributions

In the case of the charge symmetric reaction, ^{48}Ca + ^{144}Sm , the γ–ray spectrum at θ_{lab} = 82.8° and 97.1° can be adequately reproduced using the sum of the statistical decay code CASCADE [57] and the bremsstrahlung component, previously obtained in section 4.2.2. In figure 4.6 the fusion–evaporation γ–ray spectrum of the ^{48}Ca + ^{144}Sm reaction (squares) together with theoretical spectra (solid line) obtained with the code CASCADE for the same reaction and folded with the response function of the experimental apparatus [109] is shown. The data can be reproduced well in the whole energy region of interest by using the following parameters in the calculation: a CN mass of ^{189}Tl, E*= 220 MeV, as obtained by the charged particle spectra analysis, and a level density parameter $a = \frac{A}{10}\ MeV^{-1}$. The GDR strength function was taken to be a lorentzian curve with centroid energy E_{GDR} = 13.5 MeV, width Γ_{GDR} = 12 MeV, and strength S_{GDR} = 1 TRK = 100% of the E1 energy-weighted sum-rule strength throughout the calculation.

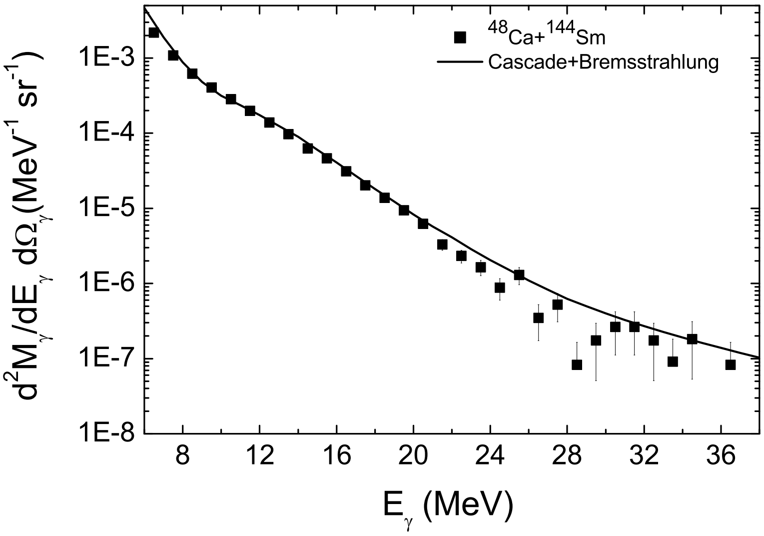

Figure 4.6: *γ–ray spectrum of the charge symmetric reaction ^{48}Ca + ^{144}Sm reaction (squares) obtained at θ = 82.8° and 97.1° and theoretical spectrum (solid line) calculated with the code CASCADE for the same reaction and the bremsstrahlung contribution as described in the text.*

In figure 4.7 the center-of-mass double differential γ-ray multiplicity of the two reactions (up) for fusion-evaporation is displayed. The solid (dashed) line in the top of the figure represents the charge asymmetric ^{40}Ca+^{152}Sm (charge symmetric ^{48}Ca+^{144}Sm) reaction. The difference between the data of the two reactions, shown in the bottom panel of the same figure, evidences an excess of γ–rays in the more charge asymmetric reaction, concentrated in the energy range E_γ=8-14 MeV. This excess cannot be ascribed to differences in the statistical GDR in the CN formed in the two reactions, being identical all the reaction parameters, except for the entrance channel charge asymmetry. Therefore, it is related to the entrance channel charge asymmetry effects and it is attributed to the dynamical dipole (DD) mode present at the beginning of the dinuclear system formation.

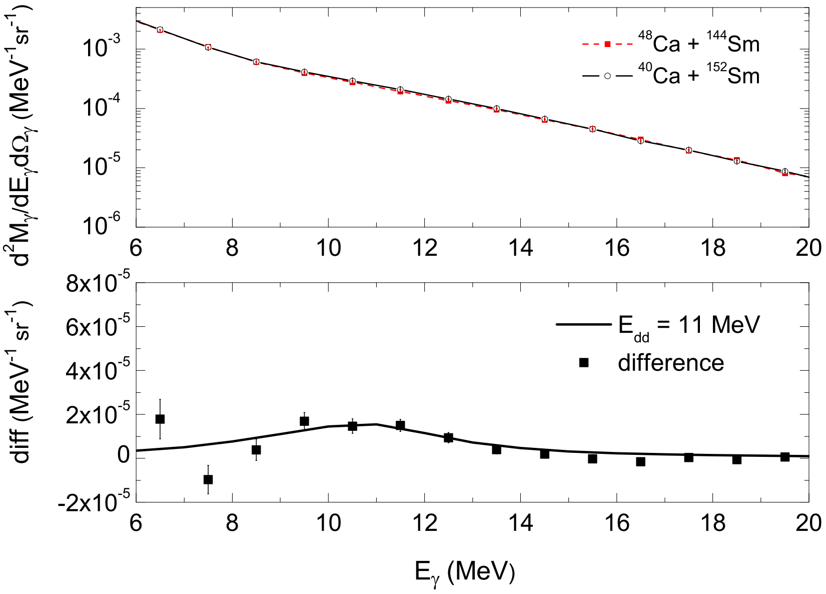

Figure 4.7: *Center-of-mass γ–ray spectra in coincidence with evaporation residues for the charge symmetric reaction ^{48}Ca + ^{144}Sm reaction (red dashed line) and for the charge asymmetric ^{40}Ca + ^{152}Sm reaction (black solide line) and their difference (bottom). The solid line in the bottom panel is described in the text.*

This excess can be reproduced by means of a lorentzian curve folded by the experimental apparatus response function (solid line in the bottom of the figure) with these features: a centroid energy E_{DD} = 11 MeV, a width Γ_{DD} = 3.5 MeV. It is important to note that E_{DD} was found to be lower than the CN GDR centroid energy E_{GDR} = 13.5 MeV of the ^{48}Ca+^{144}Sm reaction. This result confirms the high deformation of the emitting source, in agreement with expectations [7, 27] and with our previous works [23–25].

Although such γ excess constitutes one of the signatures of the DD mode radiation, the angular distribution is also an important observable since it gives information about the reaction dynamics and the lifetime of this emission. This is related to (a) the rotation angular velocity of the dinuclear system during the prompt dipole emission and (b) the instant at which this emission occurs [29].

In order to obtain the angular distribution of the γ–rays with respect to the beam direction for evaporation events, we fit the center-of-mass double differential γ–ray multiplicity spectra, obtained in coincidence with evaporation residues, after the subtraction of (nn)-bremsstrahlung component with a Legendre polynomial expansion:

$$M_\gamma(E_\gamma, \theta_\gamma) = M_0[1 + Q_2 a_2(E_\gamma) P_2(cos(\theta_\gamma)] \tag{4.11}$$

where P_2 is the 2^{nd} order Legendre polynomial, $P_2(\cos\theta) = \frac{1}{2}(3\cos^2(\theta) - 1)$, a_2 is the anisotropy coefficient and Q_2 is an attenuation factor for the finite γ–ray counter which, for the present geometry, was found to be ~0.98 [110]. In all cases, the coefficient M_0 was obtained from a best fit to the data.

In figure 4.9 we display the energy dependence of the a_2 coefficient for the ^{40}Ca + ^{152}Sm reaction (top) and the ^{48}Ca + ^{144}Sm one (bottom) for a 1 MeV energy bin. Since the γ–rays emitted in the symmetric reaction, ^{48}Ca + ^{144}Sm , originate exclusively from the statistical GDR decay, the a_2 coefficient is expected to have an energy dependence characteristic of statistical GDR γ decay in a hot rotating CN of average mass A=189 and of mean spin $I = 28\hbar$ (evaporation events), according to PACE2 calculations.

We remind that in a rotating, not collectively oblate CN, as in this case, the two low-energy GDR components (along the two longer axes) are degenerate and their angular distribution with respect to the beam axis should present a minimum $a_2 = -0.25$ (stretched dipole transitions) while the upper-energy GDR component should have an $a_2 = 0.5$ (unstretched dipole transition) with some attenuation because of the overlapping of the different GDR components and of fluctuations of the orientation of the angular frequency vector with respect to that of the density distribution [78].

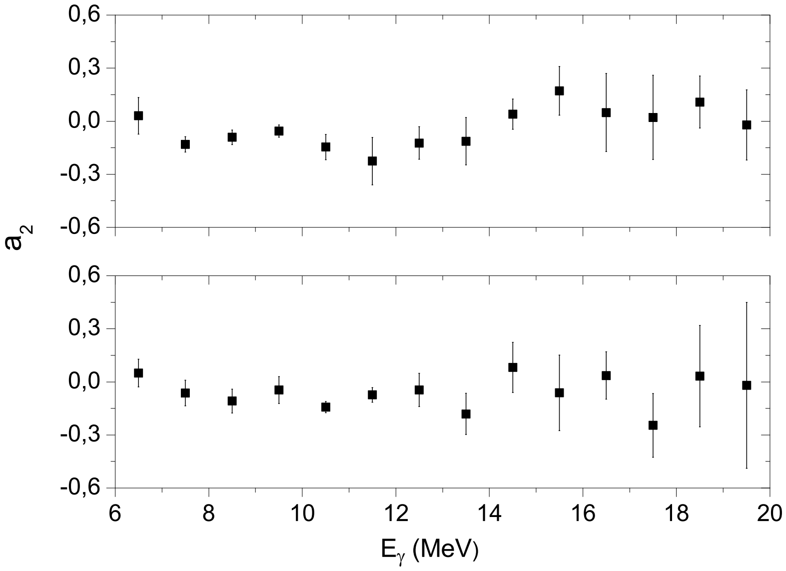

Figure 4.8: *Energy dependence of the a_2 coefficient for the ^{40}Ca + ^{152}Sm (top) and the ^{48}Ca + ^{144}Sm (bottom) reaction for evaporation events in the center-of-mass reference frame.*

Some details on the anisotropy coefficient related to GDR γ emission from a hot rotating CN are given in section 1.3. This expectation is in agreement with our data. From the figure we observe in the DD energy range a larger (in absolute value) a_2 coefficient for the charge asymmetric reaction, ^{40}Ca + ^{152}Sm (top), with respect to that of the charge symmetric reaction. Since we have selected the same CN, with the same excitation energy and angular momentum, such a difference in the γ–ray angular distributions should be ascribed to entrance channel effects namely to the DD γ decay. In picture 4.9 the center-of-mass angular distribution of the γ–rays with respect to the beam direction for the ^{40}Ca + ^{152}Sm reaction (top, squares), the ^{48}Ca + ^{144}Sm reaction (top, circles) and for their difference (bottom) integrated in the range 9 MeV$\leq$E$_\gamma$$\leq$16 MeV. The angular distributions are corrected by the experimental setup efficiency obtained from the response function of the apparatus. A best fit to the data of each reaction (top) is shown with a solid (dashed) line for the ^{40}Ca + ^{152}Sm (^{48}Ca + ^{144}Sm) reaction. The a_2 anisotropy coefficient that fits the charge symmetric reaction energy integrated data is equal to -0.05 ± 0.03, while its equal to -0.08 ± 0.06 for the charge asymmetric reaction. Also here we notice a more anisotropic angular distribution around 90° of the charge asymmetric reaction data than those of the charge symmetric reaction, showing up in a larger absolute value of the a_2 anisotropy coefficient.

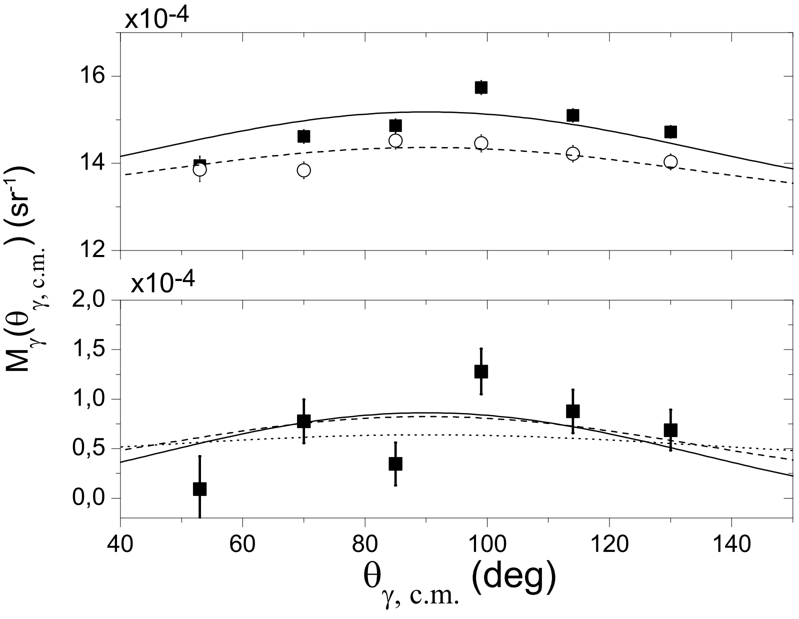

Figure 4.9: *Center-of mass angular distribution of the* γ*–rays for the* ^{40}Ca + ^{152}Sm (^{48}Ca + ^{144}Sm) *reaction with squares (circles) in the energy interval 9MeV≤*E_γ*≤16 MeV, corrected by the experimental set up efficiency (top) and center-of mass angular distribution of the difference between the data of the two reactions in the same* E_γ *interval (bottom).*

As a consequence of the above, the experimental angular distribution of the difference between the data (squares in the bottom of figure 4.9), the DD angular distribution is very anisotropic around 90°. The lines describe the expected γ–ray angular distribution for different values of the anisotropy coefficient a_2. The dotted line, obtained with a_2 = -0.25, corresponds to a more isotropic angular distribution similar to that expected for the GDR γ rays from the hot rotating CN. The solid line, corresponding to a_2 = -1, is compatible with an emission from a dipole oscillation along an axis that has performed a small rotation with respect to the beam axis. By integrating over 9 MeV$\leq E_\gamma \leq$16 MeV, the data can be reasonably fitted with a_2 = -0.63, represented by the dashed line in the bottom panel of the figure. Actually, the data can be reproduced well from both the solid (a_2 = -1) and the dashed line, but, since the large statistical uncertainties and the restricted angular range, we can not distinguish clearly between the two different values of a_2.

However, the observed anisotropy, larger than that expected for the statistical GDR γ–ray emission, confines the DD γ-emission time scale at the beginning of the reaction and proves its pre-equilibrium character. This outcome is in agreement with our previous results [25, 26] and with theoretical predictions [9, 27].

By integrating over energy (from 8 to 16 MeV) and over solid angle the difference between the γ-ray spectra of the two reactions and by taking into account the response function of the experimental setup the DD yield in evaporation events is equal to $(9.7 \pm 1.2)*10^{-4}$ with the quoted errors being statistical. A 3% error in the BaF_2 scintillator efficiency gives a $\pm 3.8*10^{-5}$ error in the above values of the DD multiplicity, smaller than the statistical error.

Chapter 5

Fission: data analysis and results

5.1 Pre–equilibrium particle emission

As done in fusion–evaporation, we evaluated the excitation energy of the CN by analysing the energy spectra of protons and α-particles detected by the BaF_2 scintillators in fission events. This procedure was applied in both reactions for BaF_2 detectors located at several polar angles, ranging from 51° to 160°, with respect to the incident beam direction. As in case of evaporation events, also here, rings placed at 82° and 97° were not used.

After selecting events corresponding to the detection of a light charged particle from the discrimination plot of each BaF_2 (as described in section 3.4.3) in coincidence with reaction products detected by two PPACs placed at $\theta_{lab} = 52.5°$, inside the graphical contours shown in figure 3.11, the double differential multiplicity in energy and solid angle of the emitted protons and α-particles following the two fusion reactions can be calculated, in analogy to (3.2), as:

$$\frac{d^2 M_{particle}}{dE_{particle}\, d\Omega_{particle}} = \frac{d^3 N_{particle}}{dE_{particle}\, d\Omega_{particle}\, d\Omega_{ppac}} \cdot \left(\frac{dN_{lib,ppac}}{d\Omega_{ppac}} \right)^{-1} . \qquad (5.1)$$

5.1.1 Charged particle energy spectra

In the case of fission, emission from the two excited fission fragments must be considered too, besides a slow source with the center-of-mass velocity simulating the statistical particle emission from the CN and an intermediate-velocity source that represents the emission of fast particles of non statistical origin, as done in fusion–evaporation (see section 4.1.1 for more details). Therefore we can again apply the multiple-source least-squares fit analysis of the experimental data using four sources, instead of only two ones as previously done in evaporation events.

The emission spectrum from the CN was assumed to be a *surface* type Maxwellian distribution, while the spectrum associated to the pre–equilibrium emission was assumed to be a *volume* type, as done in section 4.1.1. Also the light particle emission from fission fragments evaporation was described in the same way of CN with a *surface* emission, as reported below :

$$\left(\frac{d^2M}{d\Omega dE}\right)_{ff_i} = \frac{M_{ff_i}}{4\pi T_{ff_i}^2}\,(E - E_c)\, exp\left[-\frac{(E - E_c)}{T_{ff_i}}\right] \tag{5.2}$$

where E is the particle energy, E_c is the Coulomb barrier for particle emission, T_{ff_i} is the apparent source temperature and M_{ff_i} is the multiplicity of the particles emitted from a fission fragment (i indicates the 1^{st} or the 2^{nd} fragment). This Maxwellian distribution was transformed to the laboratory reference frame using the following relation:

$$\left(\frac{d^2M}{d\Omega dE}\right)_{lab} = \sqrt{\frac{E_{lab}}{E'}}\left(\frac{d^2M}{d\Omega dE}\right)_{E\equiv E'} \tag{5.3}$$

where the particle energy E' in the source reference frame is given by:

$$E' = E_{lab} + E_s - 2\,\sqrt{E_{lab}\;E_s}\;cos\theta_{lab} \tag{5.4}$$

with E_s equal to the kinetic energy of a particle moving with the source velocity and θ_{lab} is the relative angle between the direction of the emitting source and the direction of the detected particle.

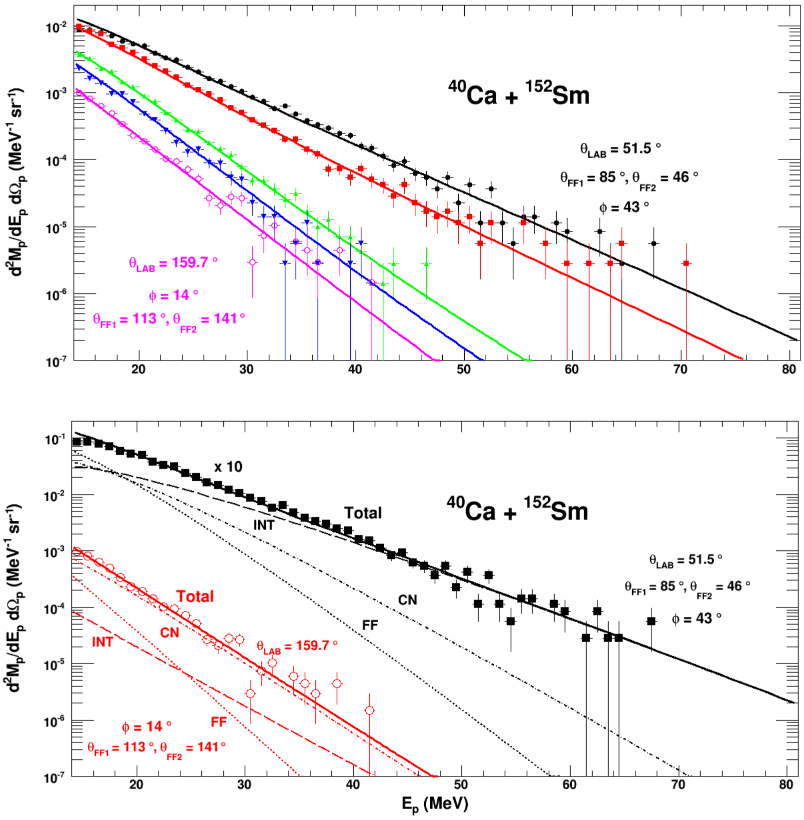

Figure 5.1: *(Top) Laboratory proton energy spectra obtained at various angles in coincidence with fission fragments for the* ^{40}Ca *+* ^{152}Sm *reaction. Here some of the spectra used are displayed, corresponding to the following* θ_{lab} = 51.5°, 68.1°, 111.9°, 128.5° *and* 159.7° *with respect to the beam direction. There are also indicated the proton emission angles with respect to the two fission fragments velocity direction,* θ_{FF1} *and* θ_{FF2}*, respectively and* ϕ *is measured from the reaction plane. The solid lines show the results of the simultaneous fits described in the text. (Bottom) Laboratory proton energy spectra at two angles with rspect to the beam direction. The solid lines (Total) are the sum of the contribution of the four sources: compound nucleus (CN), two fission fragments (FF) and pre–equilibrium (INT).*

The velocities of the two fission fragment sources were fixed to their mean velocities measured with the PPACs (see section 5.2) after taking into account the correct ion of the energy loss in the target. The evaporative source velocity was fixed to a value equal to 96% and 98% of the center-of-mass velocity, namely $v_{sl} = 0.94$ cm/ns and 1.06 cm/ns for the system ^{40}Ca + ^{152}Sm and ^{48}Ca + ^{144}Sm , respectively, as determined by the fission fragment velocities. For the *slow* and *intermediate velocity* source we used the same value of the Coulomb barrier E_c as in evaporation events: 6 MeV for protons and 15 MeV for α particles; while for fission fragments the Coulomb barrier values were fixed to 4 MeV for protons and 10 MeV for α particles. For the particle evaporation from fission fragments we assumed that $M_{ff_1} = M_{ff_2}$ and $T_{ff_1} = T_{ff_2}$, i.e. an equal number of emitted evaporated particles and equal temperatures for both fission fragments, in the hypothesis of a symmetric fission process. Anyway we checked that the parameters extracted from the fit were not very sensible to small differences of the M_{ff} value of the fission fragments.

The temperatures and the multiplicities for the evaporation from the composite system and both fission fragments, as well as the temperature, the multiplicity and the velocity for the pre–equilibrium emission were taken as free parameters, determined by the least-squares fit to the experimental particle energy spectra.

Many studies [111–115] demonstrated the existence of an azimuthal dependence of the light particles relative to the plane defined by the beam and the detected fission fragments, showing a clear preference for the emission of energetic light particles in the plane of the outgoing fission fragments. This anisotropy in the light particle emission is expected to increase with increasing mass of the particle, as well as also with both particle energy and angle. Therefore the proton azimuthal dependence should be consistent with isotropy, while the α particles should present some anisotropy.

A simple way to parametrize this behavior of the light charged particle emission is with the following relation [114] :

$$W(\phi) = 1 + amE\ sin\theta\ cos^2\phi \tag{5.5}$$

where θ is the angle from the beam, ϕ is measured from the reaction plane,

m and E are the mass and the laboratory energy of the light charged particle and a is an anisotropy coefficient. In [114] a value of 0.005 for the parameter a was found to reproduce the average trend exhibited by the experimental data. Although the statistics of the particle spectra is poor and does not allow us to clearly distinguish an effect of an azimuthal anisotropy in the light charged particle emission, we are able to fit reasonably well the data both in and out of plane without use of the azimuthal dependence, therefore we conclude that the parameter a can be taken equal to 0 within errors for both proton and α particle spectra.

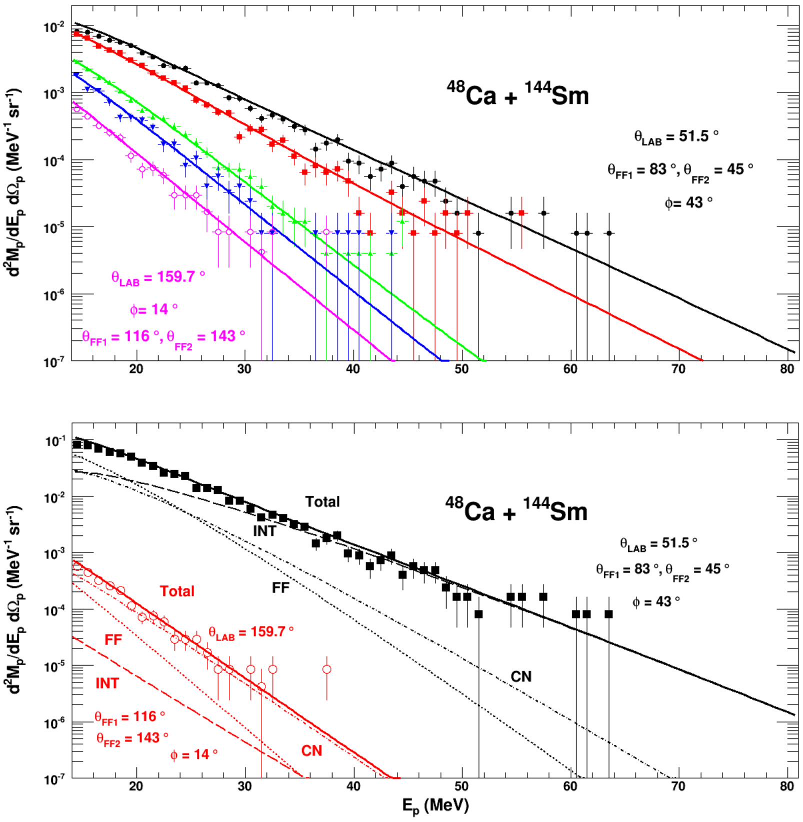

Figure 5.2: *Same as in Figure 5.1 for* ^{48}Ca + ^{144}Sm *reaction.*

Examples of some of the many fitted spectra are shown with solid lines in the top of figures 5.1 and 5.2 for protons and figures 5.4 and 5.5 for α particles, respectively. The relative contribution of the sources are reported in the bottom of the same pictures for a backward and a forward ring, with respect to the beam direction. At forward angles the pre–equilibrium component is dominant, in particular at high energy. In figure 5.3 the contribution of each fission fragment in the spectrum is highlighted: in this case the 2^{nd} fission fragment is dominant with respect to the 1^{st} one, due to the kinematic focusing of the emitted particles.

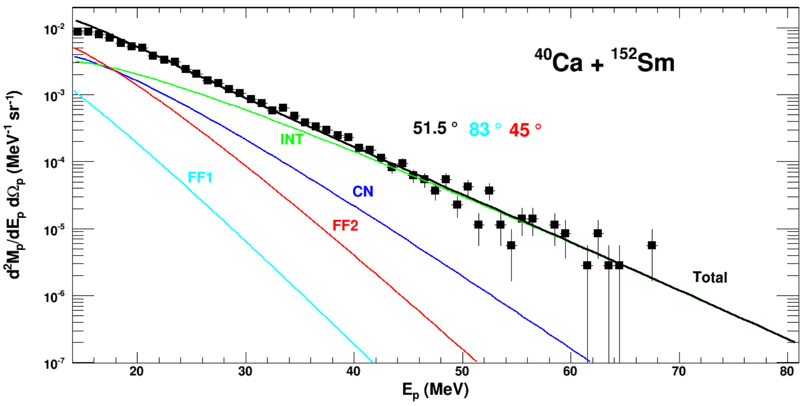

Figure 5.3: *Proton energy spectrum in the laboratory frame of a* 51.5° *BaF_2 for ^{40}Ca + ^{152}Sm reaction. The different sources are highlighted with labeled lines of different colours. The FF2 contribution is higher than FF1 one, since this detector is closer to the FF2 direction.*

The average energy taken away by pre–equilibrium neutrons was treated as done in evaporation events, assuming their energy spectra were very similar to those of proton ones, apart from Coulom barrier. Therefore the adopted pre–equilibrium neutron multiplicity are 0.45 ± 0.25 for the^{40}Ca + ^{152}Sm and 0.36 ± 0.25 for the ^{48}Ca + ^{144}Sm reaction.

The parameters extracted from the fit for all sources are reported in Table 5.1 and Table 5.2 for protons and α particles, respectively. The values of average kinetic energy, binding energy and energy lost for each pre–equilibrium particle are shown for the ^{40}Ca + ^{152}Sm and ^{48}Ca + ^{144}Sm reactions in Table 5.3 and Table 5.4, respectively. The average excitation energy of the composite system after pre–equilibrium particle emission was calculated as E^{*}=E_{CM}+Q_{gg}-E_{lost}, with E_{CM} the energy available in the center-of-mass reference frame, Q_{gg} the reaction Q-value and E_{lost} the total energy lost.

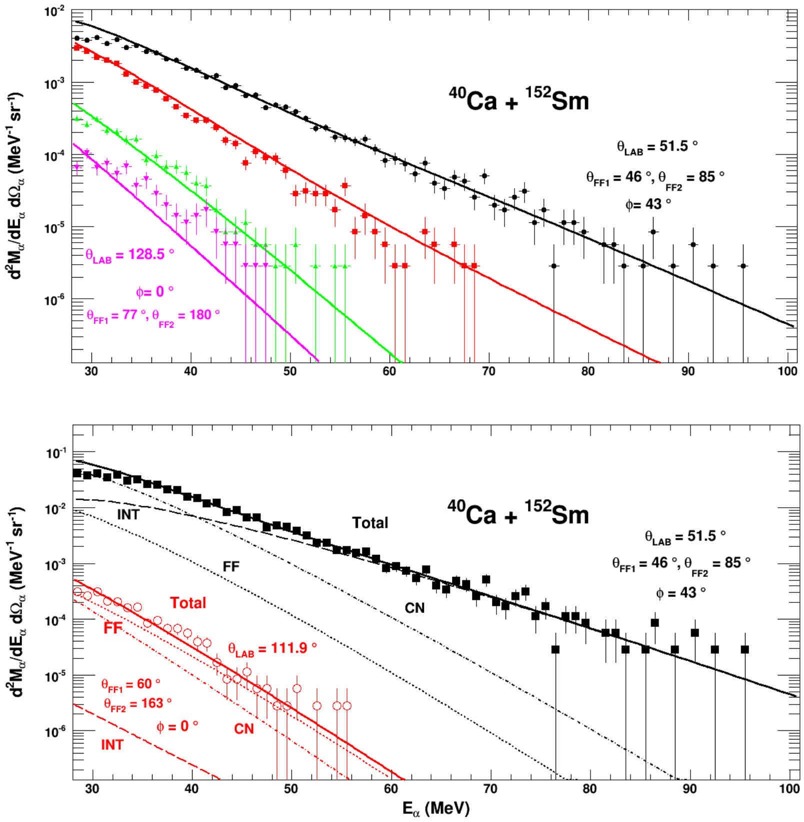

Figure 5.4: *(Top) Some examples of the multiple-moving-source fits (curves) to the experimental α-particle kinetic-energy spectra obtained at the following polar angles,* θ_{lab} = 51.5°, 68.1°, 111.9° *and* 128.5° *in coincidence with fission fragments for the* ^{40}Ca + ^{152}Sm *reaction. The solid lines show the results of the simultaneous fits described in the text. (Bottom) Laboratory α-particle energy spectra at two angles. The solid lines (Total) are the sum of the contribution of the four sources: compound nucleus (CN), two fission fragments (FF) and pre–equilibrium (INT).*

Therefore the average excitation energy was found to be E^{*}=(242.25 ± 4.55) MeV for the ^{40}Ca + ^{152}Sm and E^{*}=(244.08 ± 4.45) MeV for the ^{48}Ca + ^{144}Sm reaction (as shown in Table 4.5), with an average mass A = 191 of the compound system for both reactions. The maximum error of the average mass of the system is less than one unity. We can confirm thus, that the CN average excitation energy and average mass were found to be identical within errors for the two reactions in both evaporation and fission events. The average excitation energy and mass for fission events were found to be equal to those for evaporation ones (E*=220 ± 5 MeV, A=189; see section 4.1 for details) within 10%.

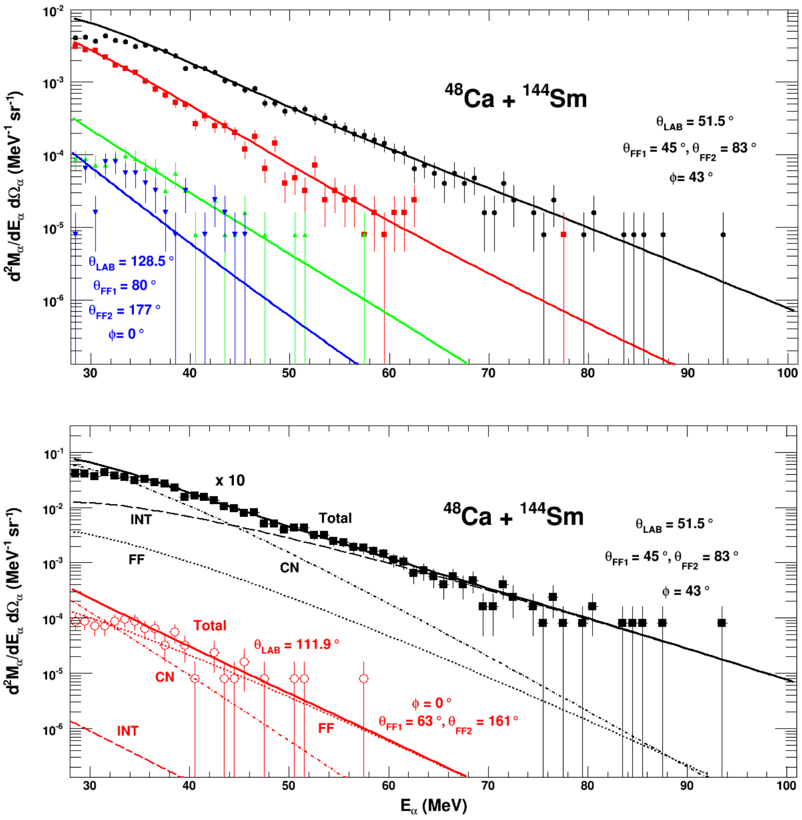

Figure 5.5: *Same as in Figure 5.4 for* ^{48}*Ca* + ^{144}*Sm reaction.*

Although the 10 % difference in the CN excitation energy observed between fission and evaporation events is not clear at the moment, a possible explanation could be due to the fact that in evaporation events we selected all the reaction planes with our PPACs (covering all azimuthal angles), while in fission only a few reaction planes were selected defined by the beam axis and the two PPACs. Therefore, only a portion of the fission events was considered, probably corresponding to events having lower energy losses taken away from pre-equilibrium particles.

Table 5.1: Parameters of the four sources extracted from the moving source fit for protons emitted in the ^{40}Ca + ^{152}Sm and ^{48}Ca + ^{144}Sm fusion reactions.

Reaction	E$_c$ (MeV)	v_{sl} (cm/ns)	M_{sl}	T_{sl} (MeV)
^{40}Ca + ^{152}Sm	6	0.94	0.45 ± 0.03	3.49 ± 0.06
^{48}Ca + ^{144}Sm	6	1.06	0.33 ± 0.03	3.40 ± 0.10

Reaction	E$_{cf}$ (MeV)	v_{ff1} (cm/ns)	v_{ff2} (cm/ns)	M_{ff}	T_{ff} (MeV)
^{40}Ca + ^{152}Sm	4	1.52	1.52	0.53 ± 0.04	2.53 ± 0.04
^{48}Ca + ^{144}Sm	4	1.63	1.60	0.45 ± 0.02	2.67 ± 0.05

Reaction	v_{int} (cm/ns)	M_{int}	T_{int} (MeV)
^{40}Ca + ^{152}Sm	2.41 ± 0.10	0.33 ± 0.02	5.01 ± 0.07
^{48}Ca + ^{144}Sm	2.76 ± 0.15	0.27 ± 0.02	4.72 ± 0.10

Table 5.2: Same as in Table 5.1 for α particles.

Reaction	E$_c$ (MeV)	v_{sl} (cm/ns)	M_{sl}	T_{sl} (MeV)
^{40}Ca + ^{152}Sm	15	0.94	0.59 ± 0.10	3.57 ± 0.13
^{48}Ca + ^{144}Sm	15	1.06	0.69 ± 0.11	3.61 ± 0.15

Reaction	E$_{cf}$ (MeV)	v_{ff1} (cm/ns)	v_{ff2} (cm/ns)	M_{ff}	T_{ff} (MeV)
^{40}Ca + ^{152}Sm	10	1.52	1.52	0.11 ± 0.05	3.00 ± 0.38
^{48}Ca + ^{144}Sm	10	1.63	1.60	0.04 ± 0.04	4.08 ± 1.13

Reaction	v_{int} (cm/ns)	M_{int}	T_{int} (MeV)
^{40}Ca + ^{152}Sm	2.46 ± 0.20	0.15 ± 0.02	5.36 ± 0.26
^{48}Ca + ^{144}Sm	2.68 ± 0.31	0.14 ± 0.02	5.50 ± 0.30

Table 5.3: Average kinetic energy E_k, binding energy E_{bind}, pre–equilibrium particle multiplicity M_{int} and average energy lost E_{lost} for the ^{40}Ca + ^{152}Sm reaction.

Particle	E_k(MeV)	E_{bind}(MeV)	M_{int}	E_{lost}=M_{int}*[E_k+E_{bind}] (MeV)
Proton	13.52 ± 0.11	3.56	0.33 ± 0.02	5.70 ± 0.34
Neutron	7.52 ± 0.11	10.56	0.45 ± 0.25	8.09± 4.52
α	23.04 ± 0.38	-5.0	0.15 ± 0.02	2.70 ± 0.41

Table 5.4: Same as in Table 5.3 for the ^{48}Ca + ^{144}Sm reaction.

Particle	E_k(MeV)	E_{bind}(MeV)	M_{int}	E_{lost}=M_{int}*[E_k+E_{bind}] (MeV)
Proton	13.08 ± 0.15	3.56	0.27 ± 0.02	4.47 ± 0.34
Neutron	7.08 ± 0.15	10.56	0.36 ± 0.25	6.36± 4.41
α	23.25 ± 0.45	-5.0	0.14 ± 0.02	2.57 ± 0.46

Table 5.5: Center-of-mass energy E_{CM}, reaction Q-value Q_{gg}, total energy lost E_{lost} and E^*, obtained after pre–equilibrium emission for both reactions.

Reaction	E_{CM} (MeV)	Q_{gg} (MeV)	E_{lost} (MeV)	E^* (MeV)
^{40}Ca + ^{152}Sm	345.81	87.06	16.49 ± 4.55	242.25 ± 4.55
^{48}Ca + ^{144}Sm	361.12	103.63	13.41 ± 4.45	244.08 ± 4.45

5.2 Fission fragments mass distribution

Fission fragments produced in the two reactions were detected using two PPACs mounted at 52.5° with respect to the beam direction, collecting the following information: energy loss ΔE, time of flight TOF and x, y positions of the fragments. From these quantities, angles, masses and velocity vectors of the fragments in the laboratory and in the center-of-mass reference frame were obtained as mentioned previously.

In this context, a systematic study of fission fragments is necessary to understand the reaction mechanism and to select mass symmetric fission events. In our experiment we wanted to favour fusion-fission events, therefore mass symmetric fission events should be considered as fusion-fission giving mainly fragments of equal mass. For that reason, we managed to have an opening angle of the two fission PPACs similar to that of Full Linear Momentum Transfer (FLMT) for mass symmetric fusion-fission events. The opening angle between the centers of the two detectors was equal to 105°, very similar to the FLMT folding angle for mass symmetric fusion-fission for the ^{40}Ca + ^{152}Sm channel ($\theta_{folding}$ = 103°) while it was larger than the same quantity ($\theta_{folding}$ = 95°) for the ^{48}Ca + ^{144}Sm channel: this resulted in a slight difference in the distribution of the composite system mass partition for the two reactions. In order to render it identical, appropriate countours in the bidimensional plot ΔE *vs* TOF of the coincident fragments were applied, as shown in the following. By considering mass symmetric partition of the fissioning system, we favoured fusion-fission reactions, without excluding however the contribution of some quasifission events.

5.2.1 Kinematics of the fission process

In fission reactions, the emitted fragments will be coplanar at 180° separation with respect to each other in the center-of-mass frame. The emission angle between the two fragments in the laboratory frame is usually referred to as the *folding angle*, which depends on the velocity of the fragments and also on the recoil velocity of the fissioning nucleus.

Let us consider the kinematics of fission process from CN, as shown in figure 5.6; for simplicity in this picture mass symmetric fission process is displayed.

$\vec{v_1}$ and $\vec{v_2}$ are the velocities of the fragments (FF_1 and FF_2 respectively) in the laboratory frame and $\vec{v_{cm}}$ is the center-of-mass velocity. $\vec{V_{rec}}$ is the recoil velocity of the CN. θ_1 and θ_2 are the fragment angles in laboratory frame with respect to the beam axis. By definition, the folding angle is given by

$$\theta_{folding} = \theta_1 + \theta_2 \tag{5.6}$$

If we know θ_1, θ_2 can be calculated and hence the folding angle. From geometry, we can find that :

$$tg\theta_2 = -\frac{v_1 sin\theta_1}{v_1 cos\theta_1 - 2V_{rec}} \tag{5.7}$$

and then

$$\theta_{folding} = \theta_1 + tan^{-1}\left[\frac{v_1 sin\theta_1}{2V_{rec} - v_1 cos\theta_1}\right]. \tag{5.8}$$

Hence from eq. 5.8, it is clear that total folding angle can be calculated if $\vec{v_1}$ and $\vec{V_{rec}}$ are known. The recoil velocity of the CN can be calculated from the recoil energy:

$$V_{rec} = \sqrt{\frac{2E_{rec}}{A_{CN}}} \tag{5.9}$$

where E_{rec} is the CN recoil energy and A_{CN} is its mass.

From the above figure it is obvious that $\vec{v_{cm}} = \vec{v_1}$ - $\vec{V_{rec}}$, than can be expressed also as

$$v_{cm}^2 = v_1^2 + V_{rec}^2 - 2v_1 V_{rec} cos\theta_1. \tag{5.10}$$

Re-arranging the equation in quadratic form and solving we get two solutions

$$v_1 = \frac{1}{2}\ 2V_{rec}cos\theta_1 \pm \sqrt{4V_{rec}^2 cos^2\theta_1 + 4(v_{cm}^2 - V_{rec}^2)}\Big] \tag{5.11}$$

We consider the positive solution only because with the increase in θ_1, v_1 becomes negative for the negative root, which is physically impossible.

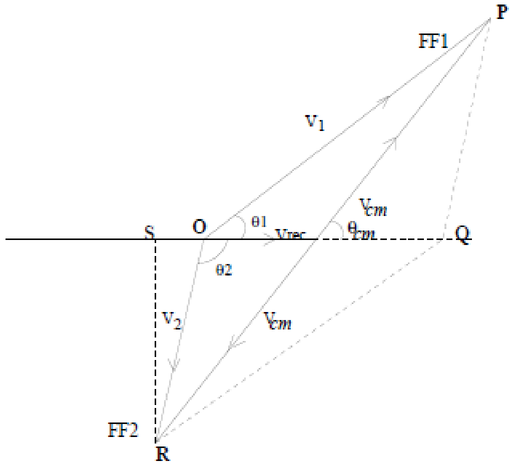

Figure 5.6: *Kinematics of symmetric fission from compound nucleus.*

The center-of-mass velocity v_{cm} of the fragment is obtained using Viola systematics [116], where the fragment kinetic energy is obtained as the result of Coulomb repulsion of two spheres in contact. Viola systematics assumes symmetric fission for calculating the average kinetic energy and is given by

$$< E_k >= \left[0.1189 \frac{Z^2_{CN}}{A^{1/3}_{CN}} + 7.3(\pm 1.5) \right] MeV \tag{5.12}$$

where Z_{CN} and A_{CN} are the atomic number and the mass of the fissioning nucleus, respectively.

To convert the values of θ_1 in laboratory frame to center-of-mass frame, a relation must be established between θ_1 and θ_{cm}. From the figure 5.6, it can be written that

$$\theta_{1cm} = tan^{-1} \left[\frac{v_1 sin\theta_1}{v_1 cos\theta_1 - V_{rec}} \right] . \tag{5.13}$$

After these simple considerations, we can proceed to evaluate the quantities useful for mass fission fragments reconstruction and distribution, namely the velocity and the position (θ, ϕ) of the detected fragments.

5.2.2 Mass reconstruction of the fission fragments

Fission PPACs, as mentioned more in detail in section 2.2, have 60 horizontal and 60 vertical wires as anodes, providing, respectively, the X (X_1 - X_2) and Y (Y_1 - Y_2) position of incident particles. The position calibrations were obtained using the known positions of the edges of the illuminated areas of the detectors during the experiment.

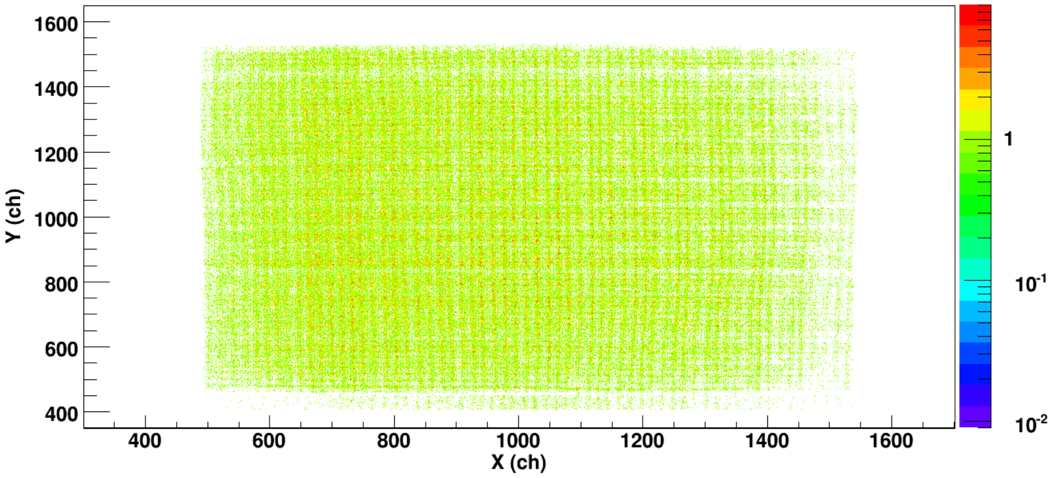

Figure 5.7: *Two dimensional plot of X versus Y of a fission PPAC for the* ^{48}Ca + ^{144}Sm *reaction.*

The position signals from the PPACs detectors were transformed event by event to polar and azimuthal angles (θ, ϕ). Uncorrelated events, as in case of X_1(Y_1) signals without the corresponding X_2(Y_2) ones and vice-versa, were eliminated. Figure 5.7 shows the 2D plot of X-position versus Y-position of one of the detectors for the ^{48}Ca + ^{144}Sm reaction, taking into account only correlated events detected by the two fission PPACs.

In the analysis only the fragments detected in coincidence between the two PPACs that fell inside the contours applied on ΔE *vs* TOF bidimensional plot were considered, as explained in section 3.4.4. In the picture 5.8 the ΔE *vs* TOF bidimensional plots (with relative graphical contours) for PPACs in coincidence in the ^{40}Ca + ^{152}Sm reaction (left-hand side) and the ^{48}Ca + ^{144}Sm one (right-hand side) are shown.

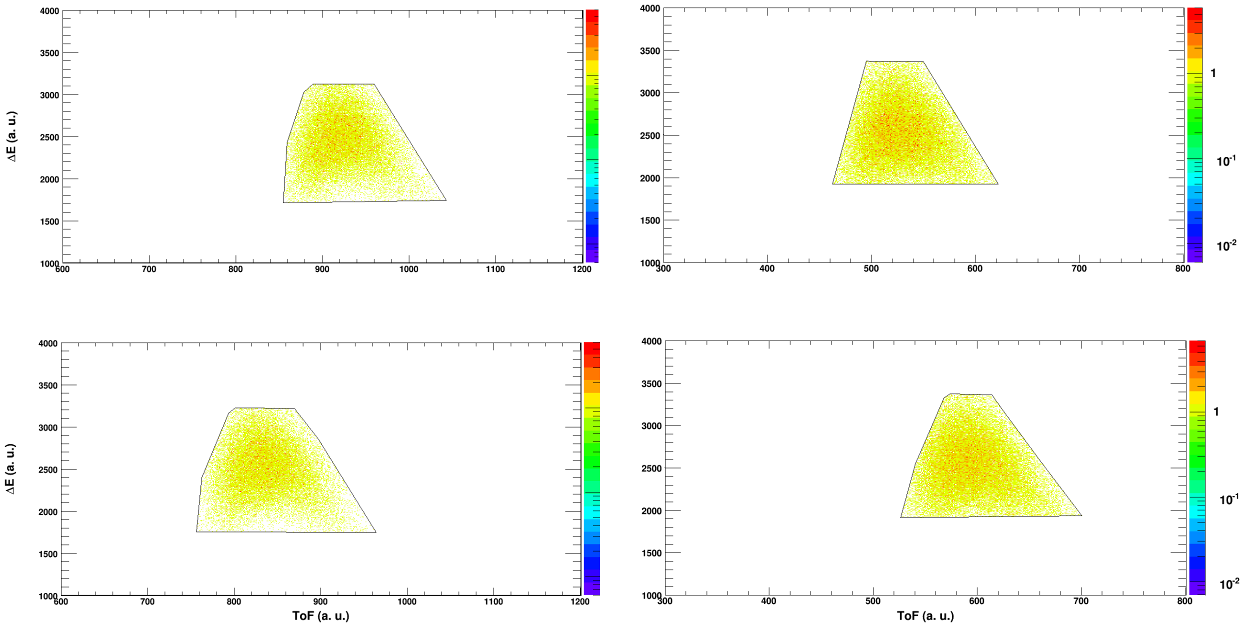

Figure 5.8: *ΔE vs TOF 2D plots for two fission PPAC detectors in the ^{40}Ca + ^{152}Sm reaction (left-hand side) and the ^{48}Ca + ^{144}Sm reaction (right-hand side). The graphical contours are used to select fission fragments. Here only coincidence events between the two PPACs, falling inside the relative contours, are shown.*

Once determined the position, θ and ϕ, of the detected coplanar ($| \phi_1 - \phi_2 | = 180° \pm 3°$) fragments, the fragment θ values were added to obtain the folding angle.

Fragment velocities in the laboratory frame ($\vec{v_1}$ and $\vec{v_2}$) were re-constructed using TOF, θ and ϕ informations. The energy loss correction of the fragments in the target was performed assuming that the interaction takes place at the midpoint of the target.

The center-of-mass velocities $\vec{v_{1cm}}$ and $\vec{v_{2cm}}$ and polar angles θ_{1cm} and θ_{2cm} of the fragments were then obtained from laboratory velocities using the kinematic expressions 5.10 and 5.13, deduced above. In this way it was possible to re-construct the angle between the two fragments in the center-of-mass reference frame, $\theta_{cm} = \theta_{1cm} + \theta_{2cm}$, for both reactions ^{40,48}Ca + ^{152,144}Sm . In a two-body collision, this distribution should be centered at 180°. However, deviations from binary kinematics due to emission of light particles perturbs the fission fragment vectors, resulting in a significant spread in θ_{cm}.

The experimentally observed laboratory velocities v_1, v_2 and laboratory polar angles θ_1, θ_2 of the two coincident fragments allowed to infer the fragment masses M_1, M_2 by applying the following relations derived from the mass and the linear-momentum balances in a two body reaction:

$$M_1 + M_2 \equiv A_{CN} = M_p + M_t \tag{5.14}$$

$$M_1 v_1 sin\theta_1 = M_2 v_2 sin\theta_2 \tag{5.15}$$

where M$_p$ and M$_t$ are the projectile and target masses, respectively. Rearranging the above equations, we can derive the expression for the two fragment masses M_1, M_2:

$$M_1 = \frac{A_{CN}\, v_2 sin\theta_2}{v_1 sin\theta_1 + v_2 sin\theta_2} \tag{5.16}$$

$$M_2 = \frac{A_{CN}\, v_1 sin\theta_1}{v_1 sin\theta_1 + v_2 sin\theta_2} \tag{5.17}$$

Using the above equations, we obtained the fragment masses for both reactions as shown in figure 5.9, using the experimental value of A_{CN}, deduced in section 5.1.1. The mass distributions observed in heavy ion induced fission reactions are generally of symmetric shape because the CN is generally formed with large excitation energy well above the fission barrier. The fragment shell effects observed in the mass distributions in the case of spontaneous and neutron or light heavy ion induced reactions at lower bombarding energies are not evident in the case of heavy ion induced reactions, due to washing out of the shell effects at high excitation energy and angular momenta brought into the fissioning composite system by the heavy ions. In general, an average increase in the width of the mass distribution is observed with the increase in the excitation energy of the fissioning nucleus [117, 118].

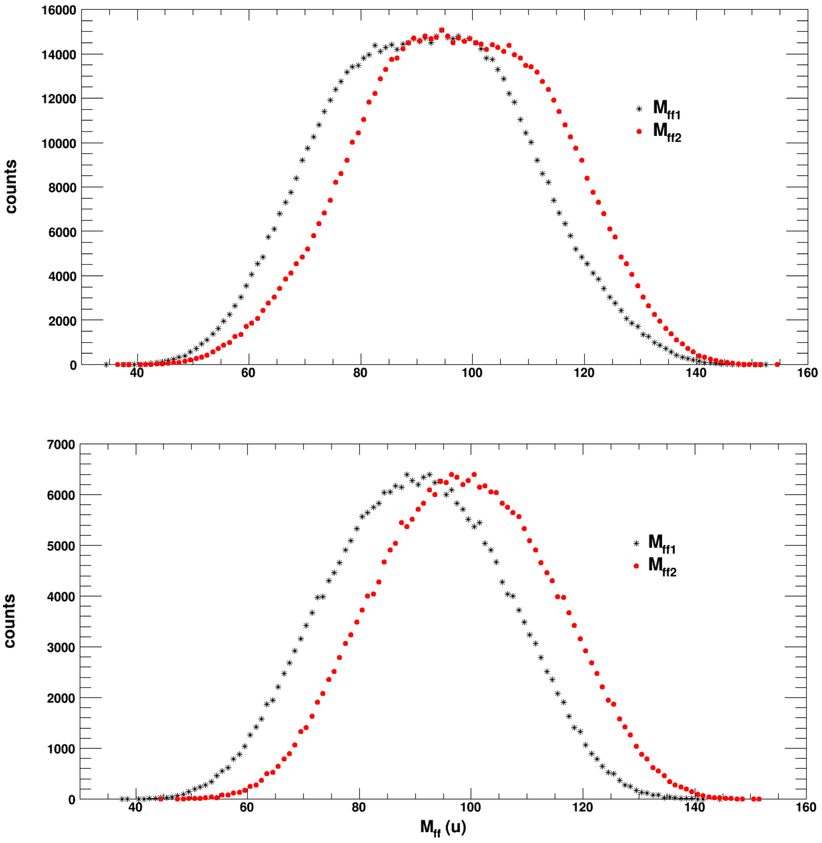

Figure 5.9: *Mass distribution of the complementary fission fragments for the* ^{40}Ca + ^{152}Sm *(top) and* ^{48}Ca + ^{144}Sm *(bottom) reaction.*

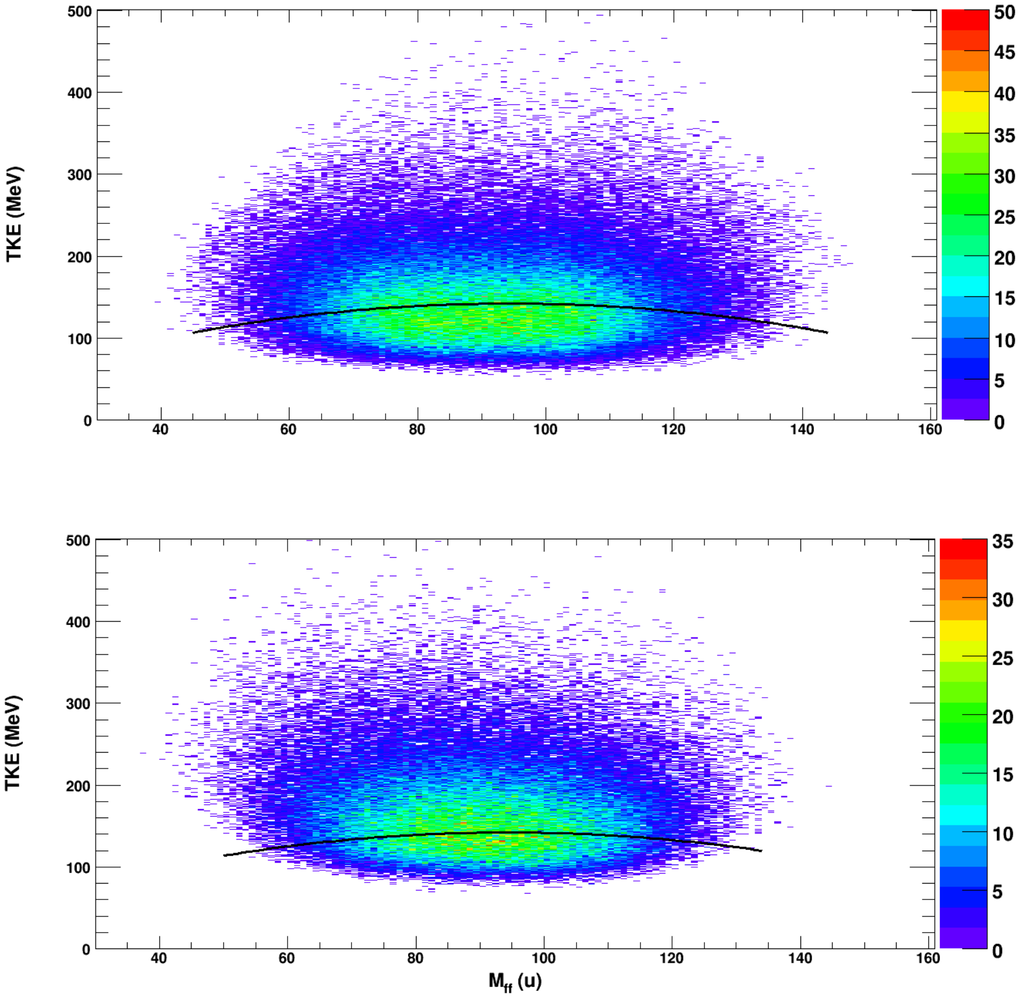

Figure 5.10: *Two-dimensional TKE–mass plots for the* ^{40}*Ca* + ^{152}*Sm (top) and* ^{48}*Ca* + ^{144}*Sm (bottom) reaction. The parabolic lines represent the expected TKE release in fission (see text).*

The mass distributions of fission fragments in heavy ion induced fission could provide information on the reaction mechanism involved in the fission process, due to admixture of fully equilibrated compound nuclear events and non-compound nuclear reactions like quasi-fission [117, 118]. In this case mass distributions would be expected to be broader than those for normal fission, because non-compound fission reactions are expected to have more asymmetric component arising due to incomplete equilibration in mass degree of freedom.

The experimental mass distributions present a gaussian shape with the following mean values: $M_1 = 91.3 \pm 10.$ and $M_2 = 97.7 \pm 10.0$ for the ^{40}Ca + ^{152}Sm reaction and $M_1 = 90.3 \pm 9.0$ and $M_2 = 98.7 \pm 9.0$ for the ^{48}Ca + ^{144}Sm reaction. These value are close to half of the mass of the CN, as in case of symmetric fission. It is important to notice that in our experiment, being interested mainly in fission symmetric events coming from fusion we have not detected all the mass partitions of the composite system, due to the geometrical coverage of the used PPACs. Therefore, we are not able to give informations about the FWHM of the mass distribution of the fissioning system. The FWHM of the observed mass distribution is determined by the geometrical dimensions of the detectors.

In picture 5.10 the total kinetic energy (TKE) released *vs* fission fragment mass distributions are shown for both systems. The lines describe the expected TKE released in fission, calculated according Viola systematics for symmetric fission and then scaled proportional to $M_1M_2/(M_1^{1/3} + M_2^{1/3})$ to take into account also mass asymmetric partitions. Our experimental data are concentrated in a region of large mass transfers in direction of symmetry, following the TKE systematics.

As mentioned before, by applying a condition on the 2D ΔE *vs* TOF plot of both fission PPACs, we can select a mass symmetric partition of the fission products. Figure 5.11 shows the ΔE *vs* TOF plots of the fission detectors couple in the ^{40}Ca + ^{152}Sm reaction (left-hand side) and in the ^{48}Ca + ^{144}Sm one (right-hand side), after considering a cut of low-TOF events, detected by the first PPAC detector ($\theta = 52,5°$, $\phi = 315°$) (top). In this way we are excluding high-velocity events in the first PPAC, in coincidence with those falling inside the graphical selection done for the second PPAC ($\theta = 52,5°$, $\phi = 135°$) of the couple. These events are related to less dissipative processes and/or more mass aymmetric partitions.

In the velocity distribution plot of the fragments, we selected only those fragments detected by the first PPAC with a velocity $v_1 \leq 2.2$ cm/ns for ^{40}Ca + ^{152}Sm system and $v_1 \leq 2.1$ cm/ns for ^{48}Ca + ^{144}Sm system. The conditioned velocity distributions are displayed in the figure 5.12. The most probable values of the fragment velocities, corrected for the energy loss in

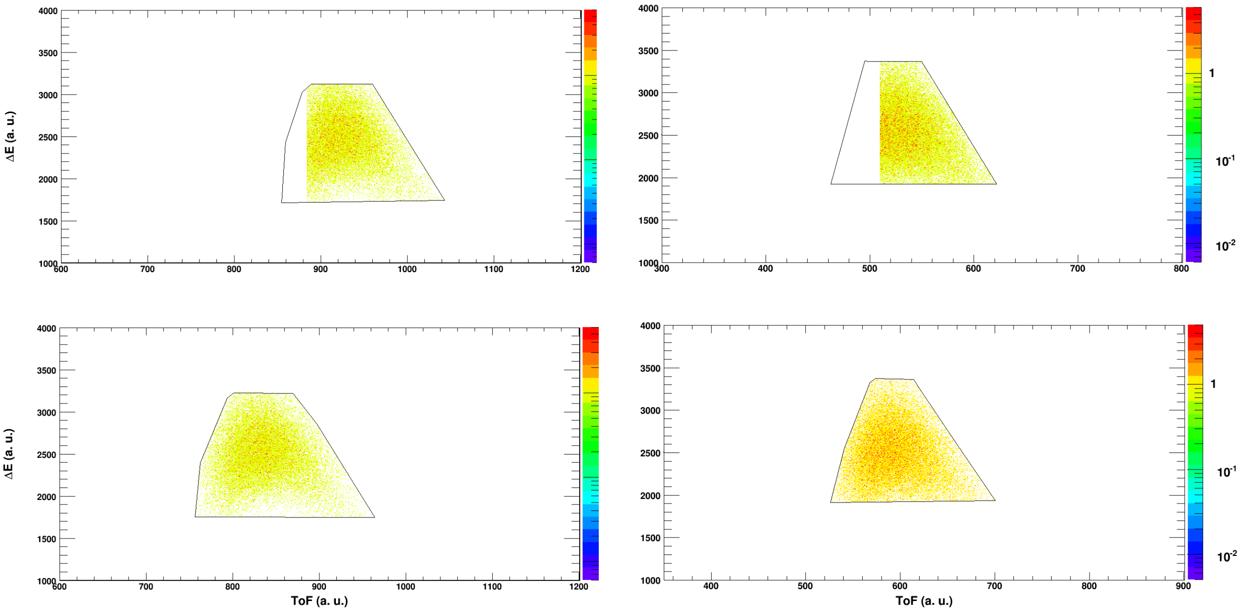

Figure 5.11: *2D* ΔE *vs TOF plots for two fission PPAC detectors in coincidence for the* ^{40}Ca + ^{152}Sm *reaction (left-hand side) and the* ^{48}Ca + ^{144}Sm *reaction (right-hand side) with their relative graphical contours. Here a selection on TOF is applied on the first PPAC (*$\theta = 52,5°$, $\phi = 315°$*) (top) in both systems, in order to favour mass symmetric partition.*

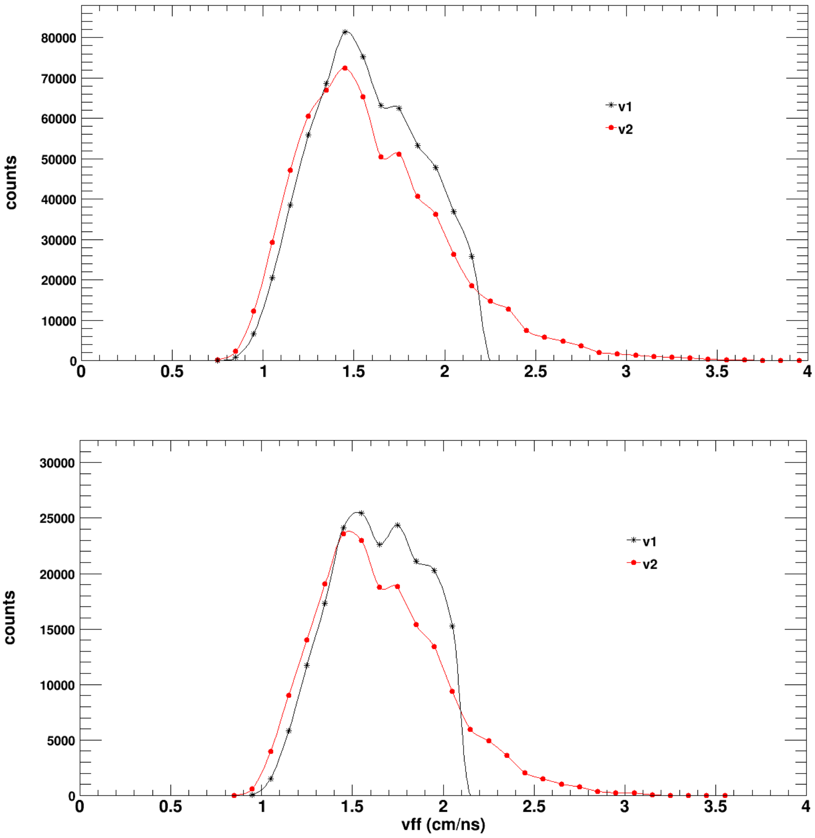

Figure 5.12: *Fission fragment velocity distributions in the laboratory frame for the* ^{40}Ca + ^{152}Sm *(top) and* ^{48}Ca + ^{144}Sm *(bottom) reaction. A cut on high values of velocity is applied to the* FF_1 *fission fragment, detetcted by the first PPAC, as explained in the text.*

the target, were used in the multiple-moving-source fits of the light charged particle spectra, described in section 5.1.1.

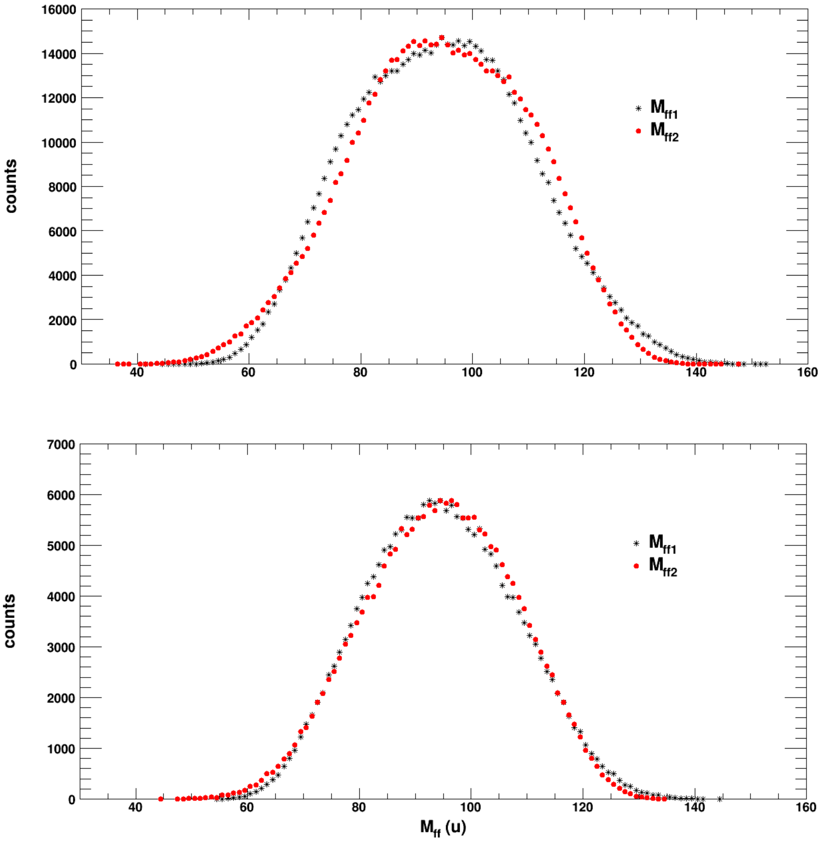

Figure 5.13: *Mass distribution of the complementary fission fragments for the* ^{40}Ca *+* ^{152}Sm *(top) and* ^{48}Ca *+* ^{144}Sm *(bottom) reaction, after conditioning the velocity of fission fragment,* FF_1*. In this way we selected mass symmetric fission events.*

Then we selected a mass symmetric splitting of the fissioning system with this cut on v_1 velocities, as shown in the deduced mass distributions in picture 5.13. The mean values of the mass distribution of both reactions are the following: $M_1 = M_2 = 94.5 \pm 10.0$ with a FWHM of 15.8 for the ^{40}Ca + ^{152}Sm reaction and $M_1 = M_2 = 94.5 \pm 9.0$ with a FWHM of 13.4 for the ^{48}Ca + ^{144}Sm reaction. These values are summarized together with the un-conditioned ones in the table 5.6. It is worthnoting that the FWHM of the shown mass distributions are very similar, however the FWHM for the ^{48}Ca + ^{144}Sm reaction is sligthly larger than that of the ^{48}Ca + ^{144}Sm reaction, because of the larger geometrical PPAC coverage for coincident events.

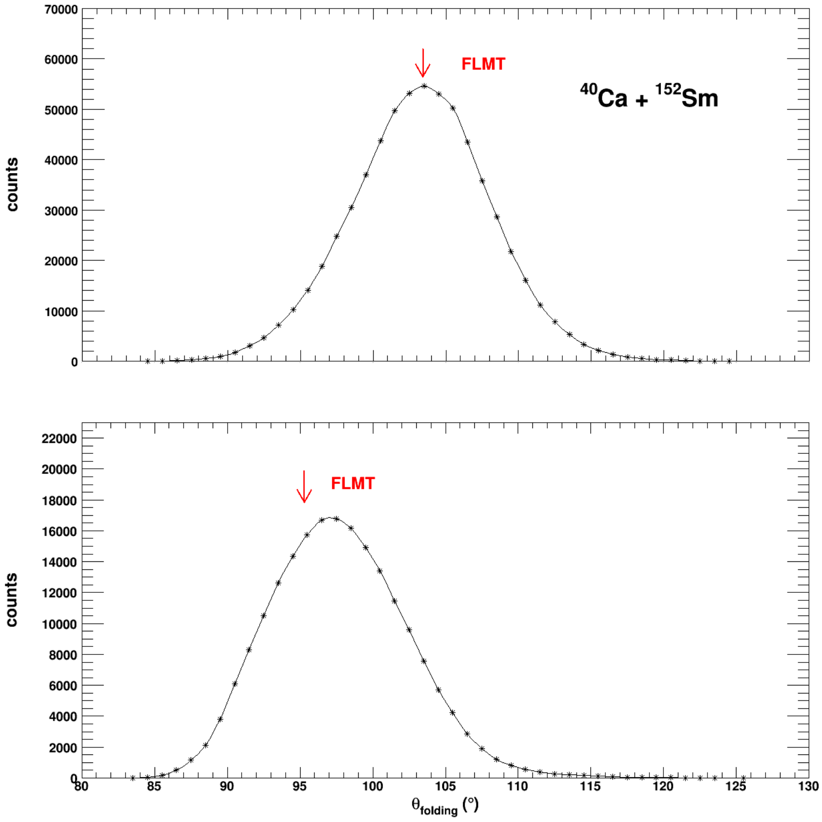

Figure 5.14: *$\theta_{folding}$ distribution for the ^{40}Ca + ^{152}Sm (top) and ^{48}Ca + ^{144}Sm (bottom) reaction. The arrows in the figure indicate the expected value of the folding angle for full linear momentum transfer.*

Figure 5.14 shows the typical folding angle distribution for mass symmetric events in the ^{40}Ca + ^{152}Sm (top) and ^{48}Ca + ^{144}Sm (bottom) reactions. The arrows in the above pictures indicate the most probable value of $\theta_{folding}$ angle expected in the case of full linear momentum transfer (FLMT): 103.2° and 95.3° for the ^{40}Ca + ^{152}Sm and ^{48}Ca + ^{144}Sm reaction, respectively.

The experimental folding angle distributions are slowly varying functions of the angle of emission of the fragment in laboratory frame, as expected,

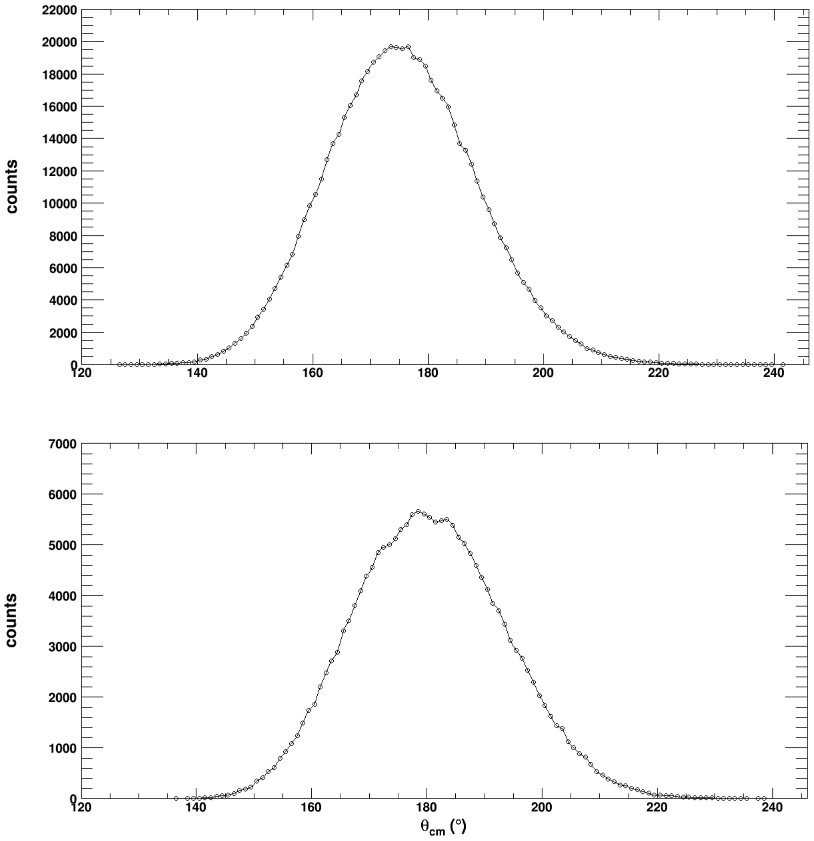

Figure 5.15: *Center-of-mass reference frame angle between the two complimentary fragments for the* ^{40}Ca *+* ^{152}Sm *(top) and* ^{48}Ca *+* ^{144}Sm *(bottom) reaction.*

with the following mean values: 103.3° ± 2.8° for the ^{40}Ca + ^{152}Sm reaction and 97.7° ± 2.8° and the ^{48}Ca + ^{144}Sm one, compatible within errors with the theoretical values. It is worthnoting that these distributions are dominated by quite full linear momentum transfer events. This is in agreement with the center-of mass velocity for fission events that we deduced from the laboratory fragment velocitie: 98% (96%) for the ^{40}Ca + ^{152}Sm (^{48}Ca + ^{144}Sm) reaction.

Figure 5.15 shows the θ_{cm} distribution for both reactions ^{40,48}Ca + ^{152,144}Sm in mass symmetric events. In a two-body collision, this distribution should be centered at 180°. However, deviations from binary kinematics due to emission of light particles perturbs the fission fragment vectors, resulting in a significant spread in θ_{cm}. The values of the folding angle and of θ_{cm} angle between the two coincident fragments are presented in the table 5.7.

Table 5.6: Parameters of the fission fragment mass distributions M_1, M_2 for the ^{40,48}Ca + ^{152,144}Sm reactions. In the first table there are the found parameters without any condition on the velocity, while in the second one all the displayed parameters were obtained with a cut on high-velocity of FF_1. This ensures us a symmetric partition of the fragments mass.

Reaction	v$_1$	M_1	M_2	FWHM
^{40}Ca + ^{152}Sm	no condition	91.3 ± 10.0	97.7 ± 10.0	17.4 ± 2.5
^{48}Ca + ^{144}Sm	no condition	90.3 ± 9.0	98.7 ± 9.0	15.4 ± 2.5

Reaction	v$_1$	M_1	M_2	FWHM
^{40}Ca + ^{152}Sm	$\leq$ 2.2 cm/ns	94.5 ± 10.0	94.5 ± 10.0	15.8 ± 2.5
^{48}Ca + ^{144}Sm	$\leq$ 2.1 cm/ns	94.5 ± 9.0	94.5 ± 9.0	13.4 ± 2.5

Table 5.7: $\theta_{folding}$, θ_{cm} in mass symmetric fission events for the ^{40,48}Ca + ^{152,144}Sm reactions.

Reaction	$\theta_{folding}$	θ_{cm}
^{40}Ca + ^{152}Sm	103.3° ± 2.8°	175.5° ± 8.9°
^{48}Ca + ^{144}Sm	97.7° ± 2.8°	180.6° ± 9.2°

After selecting the mass symmetric fission fragments, we can finally evaluate the DD emission for those events and compare to the fusion–evaporation case, discussed in the previous chapter.

5.3 γ–rays in mass-symmetric fission events

The evaluation of the pre–equilibrium particle emission in fission events, presented in section 5.1.1, demonstrated that the CN was formed in both reactions with the same average excitation energy in fission events.

After the mass reconstruction of the fission fragments, we were able to select a certain mass partition of the fragments and to evaluate the γ–ray spectra and in coincidence with these events. In our case the detection system was optimized to detect mainly mass symmetric fission fragments.

Therefore we can compare properly the results of both reactions, being confident that any difference should be ascribed to the only different parameter between the two reactions, namely the initial charge asymmetry.

γ–ray - fission events were selected with a triple coincidence between γ–rays detected by MEDEA detetctor (discriminated in the way described in 3.4.3) and mass symmetric fission fragments detected by the two 52.5° PPAC detectors.

5.3.1 γ–ray spectra

In figure 5.16 the center-of-mass double differential γ-ray multiplicity of the two reactions (up) for mass symmetric fission events is displayed. The solid (dashed) line in the top of the figure represents the charge asymmetric ^{40}Ca+^{152}Sm (charge symmetric ^{48}Ca+^{144}Sm) reaction. The difference between the data of the two reactions, shown in the bottom panel of the same figure, evidences an excess of γ-rays in the more charge asymmetric reaction, concentrated in the energy range E_γ = 9-16 MeV.

As for evaporation events, since we have selected the same CN, with the same excitation energy and angular momentum, such a difference in the γ-ray spectra between the two reactions should be due to the entrance channel charge asymmetry effects, namely to the DD γ decay.

This excess can be reproduced with a lorentzian curve folded by the experimental apparatus response function (solid line in the bottom of the figure) with a centroid energy $E_{DD} = 11$ MeV and a width $\Gamma_{DD} = 3.5$ MeV, as in case of fusion-evaporation. We notice that the DD energy spectrum has similar, within statistical uncertainties, characteristics in evaporation and in mass symmetric fission events. This outcome indicates also that the considered events originate, to a large extent, from fusion-fission reactions although some contribution from quasifission events, corresponding to larger partial waves, cannot be excluded.

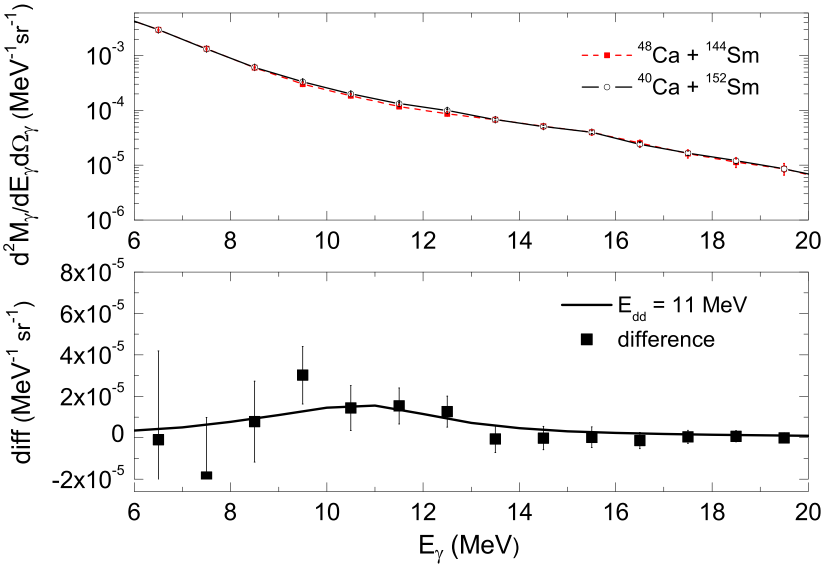

Figure 5.16: *(Top) Center-of-mass γ–ray spectra in coincidence with mass symmetric fission fragments for the charge symmetric reaction $^{48}Ca + ^{144}Sm$ reaction (red dashed line) and for the charge asymmetric $^{40}Ca + ^{152}Sm$ reaction (black solide line) and their difference (bottom). The solid line in the bottom panel is described in the text.*

The bremsstrahlung component was not subtracted from the fission data: however, as mentioned previously, it accounts for 19% of the total yield at E_γ=20 MeV, 5% of the total yield at E_γ=15 MeV and for 2% at E_γ=10 MeV. Therefore its influence on the results in the energy region of interest is small.

By integrating over the energy range between 8 and 16 MeV and over solid angle the γ–ray excess in mass symmetric fission events and by taking into account the response function of the experimental set up [109] the DD yield was found equal to $(11.0 \pm 3.5)*10^{-4}$, with the quoted errors being only statistical, since a negligible contribution of $\pm$ $3.8*10^{-5}$ due to BaF_2 efficiency error.

Chapter 6

Discussion of the results

6.1 Comparison to other systems

As proved in the previous chapters, the difference between the γ–ray spectra of the charge asymmetric reaction, ^{40}Ca + ^{152}Sm , and the charge symmetric one, ^{48}Ca + ^{144}Sm , is related to the γ decay of the DD mode. Its observation in both the evaporation and fission events, confirms its pre–equilibrium nature. It is worth noting that the γ–rays originating from its decay, displayed in 4.7 and 5.16, can be described by a lorentzian curve, folded by the experimental setup response function, with the same centroid energy E_{DD} = 11 MeV and the same width Γ_{DD} = 3.5 MeV, for both measured processes. The centroid energy E_{DD} was found to be lower than that of the statistical GDR (E_{GDR} = 13.5 MeV), implying a deformation of the composite system at the moment of the prompt dipole radiation. This outcome is in agreement with expectations [7,27] and with our previous works [23–25].

By integrating over the energy range between 8 and 16 MeV and over solid angle the γ–ray excess in evaporation and mass symmetric fission events and by taking into account the response function of the experimental set up, we have found that the DD absolute γ–ray multiplicities are comparable within statistical uncertainties: $(9.7 \pm 1.2)*10^{-4}$ and $(11.0 \pm 3.5)*10^{-4}$ for evaporation and mass symmetric fission, respectively.

In order to have the DD γ yield integrated from 8 to 21 MeV, and to compare with other data, integrated in that energy range, we can make use of the

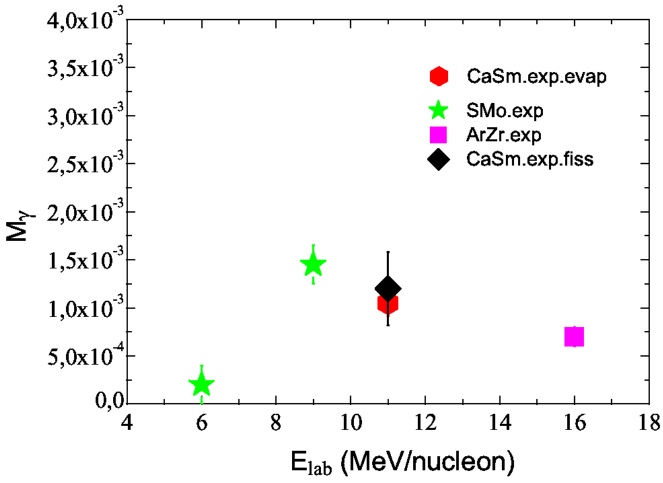

Figure 6.1: *Dynamical Dipole γ yield found for the ^{192}Pb composite system created through the reactions $^{40,48}Ca$ + $^{152,144}Sm$ (black and red symbols) compared to those obtained for the ^{132}Ce composite system formed from the $^{32,36}S$ + $^{100,96}Mo$ (green stars) and $^{36,40}Ar$ + $^{96,92}Zr$ entrance channels at different incident energies; see the text for more details.*

lorentzian curve, folded by the experimental set up response function, that reproduces our data and recover the factor between the two integrals: from 8 - 16 MeV to 8 - 21 MeV. In this case, the DD yield becomes: $(11.05 \pm 1.4)*10^{-4}$ and $(12.0 \pm 4.0)*10^{-4}$ for evaporation and mass symmetric fission, respectively. These values are compared to those found for composite systems in the ^{132}Ce mass region at different incident energies [23–26] (see section 1.4.1 for a detailed discussion) in the figure 6.1. In this figure is shown the DD γ yield observed in the present system in evaporation (red symbol) and fission events (black losange) and the DD yield observed in reactions leading to A≈132 composite systems at different incident energies and with different projecile-target combinations: ^{32,36}S + ^{100,96}Mo at 6 and 9 MeV/nucleon (*green stars*) and ^{36,40}Ar + ^{96,92}Zr at 16 MeV/nucleon (*purple square*). As we can see from the figure, for the A≈132 composite system the maximum DD yield was observed at an incident energy of 9 MeV/nucleon.

However, the comparison between the existing data on the DD yield for different composite systems is not straightforward, because the entrance channels have different initial dipole moments and mass asymmetries. The DD yield for the ^{40,48}Ca + ^{152,144}Ca systems is close to that for the ^{32,36}S + ^{100,96}Mo system, where the maximum DD yield was observed, although the initial dipole moments are very different. This observation could be a possible signature of the fact that the heavy mass of the colliding ions in the ^{40,48}Ca + ^{152,144}Ca reactions counterbalance the higher initial dipole moment as TDHF calculation predict [7]. However, this point should be further investigated in the future, from both a theoretical and an experimental point of view. More data on the DD γ yield and relative angular distribution, taken in a systematic way, are necessary to disentangle the interplay of the various reaction parameters on the DD features while theoretical investigation should be done to reproduce the experimental findings.

6.2 BNV calculations

In order to describe the evolution of the DD mode in connection to the reaction dynamics and to the symmetry energy, calculations for the ^{40}Ca+^{152}Sm reaction at 11 MeV/nucleon were performed within the *Boltzmann-Nordheim-Vlasov* (BNV) transport model framework, based on a collective bremsstrahlung approach [27, 29].

Within this model, in a microscopic approach based on semiclassical transport equations, where mean field and two-body collisions are treated in a self-consistent way (for details see [6]), it has been studied how a collective dipole oscillation develops in the entrance channel. The evolution of the dinuclear system on the fusion path, including the isovector degrees of freedom, is described by the behavior of the one-body distribution function, $f(\mathbf{r}, \mathbf{p}, \mathbf{t})$, as ruled by the self-consistent mean field, built from simplified Skyrme forces.

In this theoretical analysis, a dissipative reaction is described as developing through three main phases [9]:

- an *approaching phase* when the two partners overcome the Coulomb barrier still keeping their own response;
- a *dinuclear phase* when the conversion of relative motion energy in

thermal motion starts to take place, mainly due to nucleon exchange. The composite system is not thermally equilibrated and manifests, as a whole, a large amplitude dipole collective motion;

- the *CN formation*, when a thermally equilibrated nucleus decaying with consequent statistical particle/radiation emissions.

The second (*dinuclear*) phase can be characterized by pre–equilibrium collective dipole radiation emission with a contribution that can be estimated by applying a direct bremsstrahlung approach [27,29,119]. The total photon emission probability from the dipole mode oscillations can be expressed by the bremsstrahlung formula as ($E_\gamma = \hbar\omega$):

$$\frac{dP}{dE_\gamma} = \frac{2e^2}{3\pi\hbar c^3 E_\gamma}\left(\frac{NZ}{A}\right)^2 \left|X''(\omega)\right|^2 \tag{6.1}$$

where $X''(\omega)$ is the Fourier transform of the acceleration $X''(t)$ associated with the distance between the centers-of-mass of protons (R_p) and neutrons (R_n), $X(t) = R_p - R_n$, and $A = N + Z$ is the composite system mass. Thus following the time evolution of the dipole mode along the fusion dynamics it is possible to evaluate, in absolute values, the contribution of the pre–equilibrium dipole radiation to the photon yield [27,29,119].

In the simulations the pre–equilibrium dipole photon emission probability for the almost charge symmetric system ^{48}Ca + ^{144}Sm was found to be so small than it can be neglected.

The potential part of the symmetry energy, $E_{sym}/A(pot)$:

$$\frac{E_{sym}}{A} = \frac{E_{sym}}{A}(kin) + \frac{E_{sym}}{A}(pot) \equiv \frac{\epsilon_F}{3} + \frac{C(\rho)}{2\rho_0}\rho \tag{6.2}$$

is tested by employing two different density parametrizations of the isovector term of the nuclear effective interaction (Iso-EOS): i) $\frac{C(\rho)}{\rho_0} = 482 - 1638\rho$, ($MeV fm^3$), for "Asysoft" EoS, where $E_{sym}/A(pot)$ has a weak density dependence close to the saturation, with an almost flat behavior below ρ_0; ii) a constant coefficient, $C = 32 MeV$, for the "Asystiff" EoS choice, where the interaction part of the symmetry term displays a linear density dependence [29]. As shown in details in [120,121] these choices represent two classes of widely used effective interactions, that still require some confirmation from new independent observables. The isoscalar section of the EoS is the same in both cases, corresponding to a compressibility around $220 MeV$.

From PACE2 calculations, we expect that the maximum impact parameter corresponding to fusion–evaporation events is equal to b$_{max-evap}$ = 1.82 fm and b$_{max-evap}$ = 1.67 fm for the ^{40}Ca + ^{152}Sm and ^{48}Ca + ^{144}Sm system, respectively. In the case of fusion–fission, the process is related to higher values of the impact parameter, b$_{max-fus-fis}$ = 3.22 fm for the ^{40}Ca + ^{152}Sm reaction and b$_{max-fus-fis}$ = 2.93 fm for the ^{48}Ca + ^{144}Sm one.

Therefore, BNV calculations were performed for the charge asymmetric system at impact parameters of b = 0, 2, 4 and 6 fm that means for central but also more peripheral collisions, as our data correspond to central collisions for evaporation events, but in case of mass symmetric fission events, some contribution from quasifission (b > 3-4 fm) cannot be excluded.

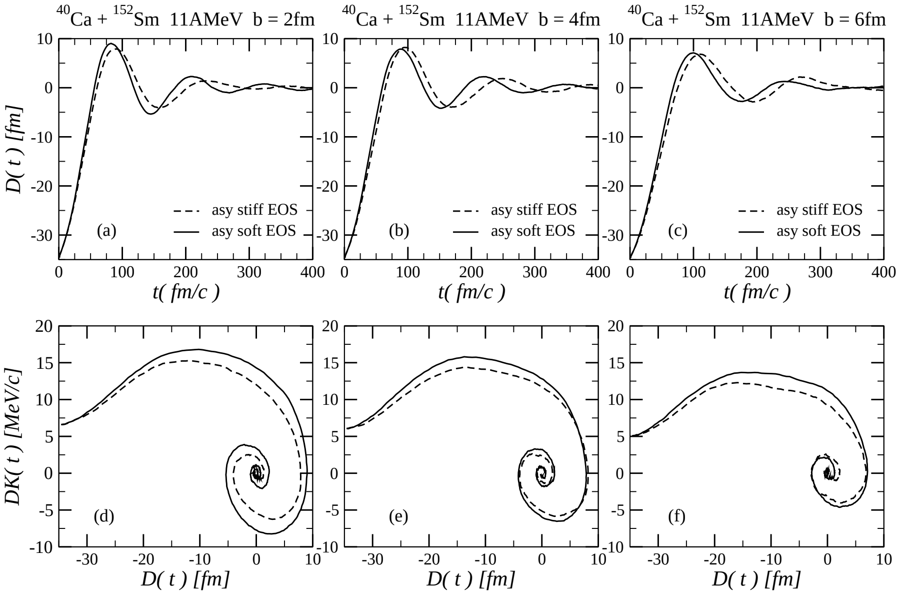

Figure 6.2: *(a), (b), (c) The time evolution of dipole mode in r-space D(t) for b = 2, 4 and 6 fm. (d), (e), (f) Dipole phase-space correlation DK(t) vs D(t) for b = 2, 4 and 6 fm. Solid lines correspond to Asysoft EOS and the dashed lines to Asystiff EOS.*

t = 0 is chosen as the starting point of the dinuclear dynamics, at the beginning of the *touching configuration*. At each time step it is possible to evaluate the mean dinuclear dipole moment in coordinate and momentum space: $D(t) = \frac{NZ}{A}X(t)$ and $DK(t) = \frac{\Pi(t)}{\hbar}$, where $\Pi = \frac{NZ}{A}\left(\frac{P_Z}{Z} - \frac{P_N}{N}\right)$ is the conjugate momentum of X(t) [9, 27]. In the expression of $\Pi(t)$, P_Z and P_N refers to the centers of mass of protons and neutrons, respectively, in the p-space.

The time evolution of the dipole mode in r-space D(t) and the dipole phase-space correlation DK(t) vs D(t) can be followed in figure 6.2 for different impact parameters and two different choices of EOS, Asysoft (solid lines) and Asystiff (dashed lines).

The "spiral-correlation" in the bottom of the figure 6.2 denotes the collective nature of the mode. In fact, it corresponds to a coherent out-of-phase oscillation of the two dipoles, in r and p-space, in presence of some damping [7,27]. When the center of the spiral curve is reached, charge equilibration is finally achieved. The spiraling trend starts when the collective dipole response of the system is triggered. That occurs with some delay with respect to the touching configuration (t = 0), necessary for the creation of the dinuclear mean field and depending on the reaction dynamics.

In figure 6.3 we show the power spectra of the dipole acceleration (in c^2 units) at different impact parameters. Solid lines correspond to Asysoft EOS and the dashed lines to Asystiff EOS. The γ multiplicity is simply related to the dipole acceleration through eq. 6.1. We clearly observe a lower value of the centroid, as well as a reduced total yield, in the Asystiff case, due to the weaker restoring force for the dynamical dipole in the dilute neck region, where the symmetry energy is smaller [120]. Slightly wider distributions are obtained in the Asysoft case, due to the larger neutron evaporation, that damps the collective oscillation. Our data are in good agreement with the theoretical results concerning the centroid energy and the width for central collisions (b = 2 fm), namely $E_{DD,th}\sim$ 10 MeV and $\Gamma_{DD,th}\sim$4 MeV while $E_{DD,exp}$ = 11 MeV and $\Gamma_{DD,exp}$ = 3.5 MeV. The total contribution from the dynamical dipole is calculated by integrating over the energy in the resonance region for each impact parameter and summing over the impact parameters leading to fusion with the corresponding geometrical weights. The γ–ray multiplicity obtained in this way for the pre-equilibrium dipole mode is $3.15(4.20) * 10^{-3}$ for the Asystiff (Asysoft) case in the impact parameter window b = 0-2 fm and $3.08(4.04) * 10^{-3}$ for b = 1-3 fm, in the Asystiff (Asysoft) case. We should compare the first value with the experimental γ–ray multiplicity found in evaporation events, while the second one should be compared with the fission experimental γ–ray multiplicity. We see that the γ–ray multiplicity obtained with BNV calculations is similar for evaporation and fission events, however, it is larger than the experimental one: further investigation thus is necessary in order to shed light on the origin of the observed discrepancy between data and theory.

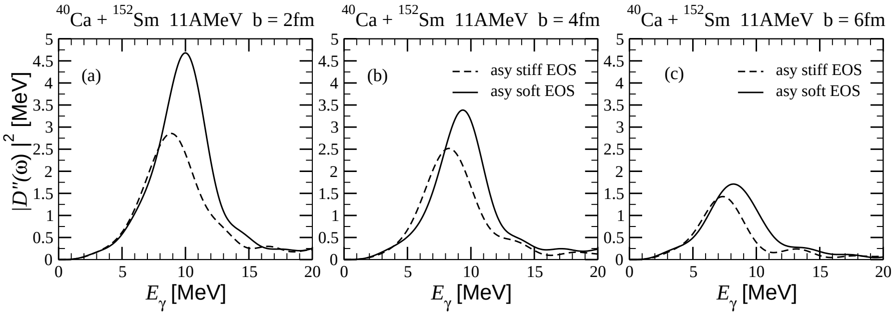

Figure 6.3: *Power spectra of the dipole acceleration (in c^2 units) at different values of the impact parameter, b. Solid lines correspond to Asysoft EOS and the dashed lines to Asystiff EOS.*

Furthermore, calculations were performed to obtain the angular distribution of the DD γ–rays with respect to the beam direction according to the method descibed in [29]. In figure 6.4 the following observables are displayed: (a) time dependence of the rotation angle of the DD axis at different impact parameters; (b), (c) and (d): time evolution of the DD emission probability P(t) calculated at b = 2, 4, 6 fm; (e) weighted angular distributions of the DD for the chosen impact parameters. For the latter quantities, the calculations were performed also for different symmetry term choices: dashed lines for the Asystiff case while the solid lines for Asysoft one.The Iso-EOS effects on the rotation angle are negligible.

From the above figures, we can see that, according to the calculations, the largest contribution to the prompt γ-yield is given by the first collective oscillations on a time interval between 50 and 150 fm/c, while the dinucleus has performed a rotation from 25° to 40°, for b = 2 fm. Therefore, since the rotation of the symmetry is rather small in central events, the predicted angular distribution of the DD is anisotropic, while for collisions corresponding to larger impact parameters, we observe that the DD axis rotates more (see panel (a)) and the corresponding angular distribution becomes flatter. The experimental angular distribution of the DD in evaporation events is in agreement with that calculated at b = 2 fm.

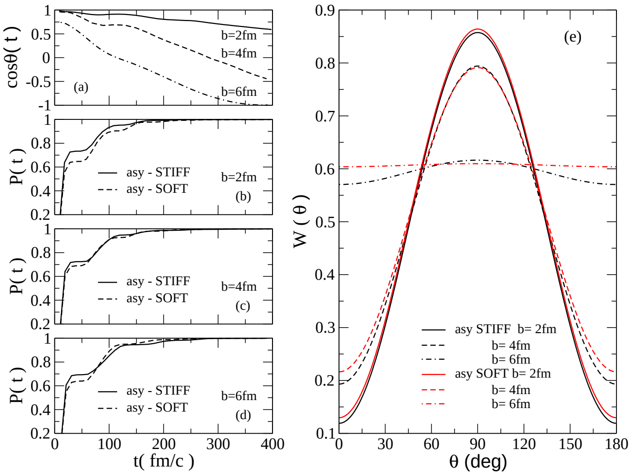

Figure 6.4: *(a) Time dependence of the rotation angle at different impact parameters b. (b), (c) and (d): Time evolution of the DD emission probability P(t), for b = 2, 4 and 6 fm. (e) Weighted angular distributions for b = 2, 4 and 6 fm centralities for different symmetry term choices. Dashed lines for the Asystiff choice and solid lines for Asysoft one.*

In summary, the performed BNV calculations for central collisions give characteristics of the DD that are in good consistency with the experimental results concerning the centroid energy, the width and the angular distribution with respect to the beam direction (for evaporation events). However, the theoretical energy-and impact parameter-integrated DD yield overpredicts the data for both dependences of the symmetry term.

Conclusions and perspectives

In this thesis, we present the first investigation of the Dynamical Dipole (DD) mode in both fusion-evaporation and fission reactions leading to the formation of a composite system in the mass region of ^{192}Pb, heavier than those studied up to now.

For this purpose, we performed two reactions, ^{40}Ca + ^{152}Sm and ^{48}Ca + ^{144}Sm at incident energies of 440 and 485 MeV, respectively, at the Laboratori Nazionali del Sud (LNS, Italy). The reactions formed the same compound nucleus (CN) at the same excitation energy E* and and with the same spin distribution. The only different parameter between the two reactions is the entrance channel charge asymmetry. The same excitation energy of the composite system was ensured through an analysis of the light charged particle double differential multiplicity for both evaporation and fission events.

The chosen observable was the multiplicity of the γ–rays detected in coincidence with the evaporation residues and with the two coincident fission fragments. The charge symmetric reaction γ–ray spectrum for evaporation events was fitted by the theoretical one obtained in the framework of the statistical model decay code CASCADE [57] and by taking into account the nucleon-nucleon bremsstrahlung component. The data were reproduced well in the whole energy region of interest by using the following parameters in the CASCADE code: a CN mass of ^{189}Tl, E*= 220 MeV, as obtained by the charged particle spectra analysis, and a level density parameter $a = \frac{A}{10}\,MeV^{-1}$. The GDR strength function was taken to be a lorentzian curve with centroid energy E$_{GDR}$ = 13.5 MeV, width Γ_{GDR} = 12 MeV, and strength S$_{GDR}$ = 1 TRK = 100% of the E1 energy-weighted sum-rule strength throughout the calculation.

For fission events, the mass and the velocity vectors of the two coincident fragments were reconstructed from their TOF and their x and y position in the PPAC detectors, allowing us to select different mass partitions. The detection system was optimized to detect mainly mass symmetric fission fragments. In that way, fusion-fission events were considered, without excluding however the contribution of some quasifission events.

The difference between the γ–ray multiplicity spectra of the two reactions exhibited an excess of γ–rays in the more charge asymmetric reaction, concentrated in the energy range E_γ=8-14 MeV, for both fusion–evaporation and mass symmetric fission. This excess cannot be ascribed to differences in the statistical GDR in the CN formed in the two reactions, being identical all the reaction parameters, except for the entrance channel charge asymmetry. Therefore, it was related to the entrance channel charge asymmetry effects and it was attributed to the DD decay. This excess was reproduced with a lorentzian curve folded by the experimental apparatus response function with a centroid energy $E_{DD} = 11$ MeV and a width $\Gamma_{DD} = 3.5$ MeV for both processes. The centroid energy E_{DD} was found to be lower than that of the statistical GDR ($E_{GDR} = 13.5$ MeV) in the CN, implying a large deformation of the composite system at the moment of the prompt dipole radiation.

An important signature of the DD mode decay is related to the γ–ray angular distribution for evaporation events that displayed an anisotropic behaviour around 90° with respect to the beam direction. This behaviour is compatible with an emission from a dipole oscillation along an axis that has performed a small rotation with respect to the beam axis. This observation confines the DD γ-emission time scale at the beginning of the reaction and confirms its pre-equilibrium character. These results are in agreement with our previous results [23–26] and with theoretical predictions [9, 27].

By integrating over the energy range and over solid angle the γ–ray excess in evaporation and mass symmetric fission events and by taking into account the response function of the experimental set up, we found that the DD absolute γ–ray multiplicities are comparable within statistical uncertainties in both classes of events: $(11.05 \pm 1.4)*10^{-4}$ and $(12.0 \pm 4.0)*10^{-4}$ for evaporation and mass symmetric fission, respectively.

BNV calculations based on a collective bremsstrahlung analysis of the reaction dynamics were performed for our system. The DD features were reproduced well by the calculations for what concerns the centroid energy, the width and the angular distribution with respect to the beam direction (for evaporation events). However, the theoretical DD yield overpredicts the data, calling for further investigation to find the origin of such a discrepancy.

As explained at the beginning of this work, the DD prompt γ radiation could favour the formation of superheavy elements by lowering the composite system excitation energy in charge-asymmetric heavy-ion hot fusion reactions. In the present thesis, it has been demonstrated that the DD survives in composite systems heavier than those studied so far, although with a γ yield that is not reproduced by BNV calculations. The outcome of a nuclear collision to form a super-heavy element is a very complicated process, as the survival probability of the composite system against quasifission and fission depends on many reaction parameters. The major experimental challenge is to find optimal beam-target combinations and kinematic conditions that would lead to the formation, at reasonable rates, of the species of interest. From the theoretical point of view, in order to predict evaporation residue cross sections of super-heavy elements in charge asymmetric reactions, we need a realistic model that follows the dynamical evolution of the system in the multi-dimensional potential energy landscape through quasi-fission or formation of the CN and its subsequent evaporation and fission, including the pre–equilibrium dipole γ–ray emission in the early stages of the collision. Such a model however, in order to have a real predictive power, should be able to reproduce all the experimental findings on the DD features. Therefore, from an experimental point of view, new experiments are needed to provide a comprehensive understanding of the DD excitation as a function of the different reaction parameters and to constraint the existing theoretical models.

By using the prompt DD radiation as a probe and radioactive beams new possibilities for the investigation of the symmetry energy at sub-saturation density are foreseen [29]. While by employing stable beams it is more difficult to draw a conclusion about the density dependence of the symmetry energy due to the experimental errors and to the small difference in the DD yield according to the different theoretical prescriptions, radioactive beams [29] are expected to maximize the difference of the DD yield between the different prescriptions of the symmetry energy dependence on density and to allow an experimental discrimination [29, 122].

Acknowledgments

First I would like to thank Professor Cosimo Signorini for having welcomed me in Padua and for his useful suggestions during this work.

I am deeply grateful to Dr. Dimitra Pierroutsakou, for teaching me a lot of physics and for her constant support and advice during these years.

Of course, I have to thank Dr. Brunella Martin who introduced me to this project and Dr. Rosetta Silvestri who worked with me in the early stages of the analysis.

I thank all the members of the MEDEA collaboration, who allowed to realize this experiment. In particular, I really appreciated the fruitful discussions with Dr. Rosa Alba and Dr. Domenico Santonocito during the analysis. Moreover, I am grateful to the theoretical group of Catania and Dr. Virgil Baran for performing the calculations presented in this thesis.

I spent nice moments with my colleagues in Padua and, especially, during the measurements in Legnaro. In particular, I warmly thank Dr. Marco Mazzocco and his contagious laughter.

I will never forget the incredible experience of *flamenco*: *Gracias chicas*!

I have to thank my friends for all the good moments we spent together and also for their patience and support: Sara, Marco, Crì, Domenico, Sabine, Andrea, Laura and Marco. Thanks to Odra and Assu, with whom I shared my stay in Padua: I'll miss our home at Terranegra!

There are no words to say thank to my “sister”, she knows well how her presence is fundamental to me.

Last but not least, grazie alle “colonne portanti”, la mia famiglia e Gennaro, che mi hanno coccolato e sostenuto in questi anni trascorsi tra Padova e Napoli.

Bibliography

[1] K.A. Snover, *Ann. Rev. Nucl. Part. Sci.* **36**, (1986) 545

[2] J.J. Gaardh⊘je, *Ann. Rev. Nucl. Part. Sci.* **42**, (1992) 483

[3] D. Santonocito et Y. Blumenfeld, *Eur. Phys. J.* **A30**, (2006) 183

[4] Ph. Chomaz et al., *Nucl. Phys.* **A563**, (1993) 509

[5] P.F. Bortignon et al., *Nucl. Phys.* **A583**, (1995) 101c

[6] V. Baran et al., *Nucl. Phys.* **A600**, (1996) 111

[7] C. Simenel et al., *Phys. Rev. Lett.* **86**, (2001) 2971

[8] C.H. Dasso, H. Sofia and A. Vitturi, *Eur. Phys. J.* **A12**, (2001) 279

[9] V. Baran et al., *Nucl. Phys.* **A679**, (2001) 373

[10] A. S. Umar and V. E.Oberacker, *Phys. Rev.* **C76**, (2007) 047602

[11] A. S. Umar and V. E.Oberacker, *Phys. Rev.* **C85**, (2012) 017602

[12] H. L. Wu et al., *Phys. Rev.* **C81**, (2010) 047602

[13] Y. G. Ma et al., *Phys. Rev.* **C85**, (2012) 024618

[14] L. Campajola et al., *Z. Phys.* **A352**, (1995) 352

[15] M. Sandoli et al., *Z. Phys.* **A357**, (1997) 67

[16] M. Sandoli et al., *Eur. Phys. J.* **A6**, (1999) 275

[17] D. Pierroutsakou et al., *Eur. Phys. J.* **A16**, (2003) 423

[18] M. Papa et al., *Phys. Rev.* **C68**, (2003) 034606

[19] M. Papa et al., *Phys. Rev.* **C72**, (2005) 064608

[20] F. Amorini et al., *Phys. Rev.* **C69**, (2004) 014608

[21] S. Flibotte et al., *Phys. Rev. Lett.* **77**, (1996) 1448

[22] M. Cinausero et al., *Il Nuovo Cimento* **111**, (1998) 613

[23] D. Pierroutsakou et al., *Eur. Phys. J.* **A17**, (2003) 71

[24] D. Pierroutsakou et al., *Phys. Rev.* **C71**, (2005) 054605

[25] B. Martin, D. Pierroutsakou et al., *Phys. Lett.* **B664**, (2008) 47

[26] D. Pierroutsakou et al., *Phys. Rev.* **C80** (2009), 024612

[27] V. Baran et al., *Phys. Rev. Lett.* **87**, (2001) 182501

[28] A. Corsi et al., *Phys. Lett.* **B679**, (2009) 197-202

[29] V. Baran et al., *Phys. Rev.* **C79** (2009), 021603 (R)

[30] M. Gell–Mann, *Phys. Lett.* **8**, (1964) 214

[31] G.C. Baldwin e G.S. Klaiber, *Phys. Rev.* **71**, (1947) 3

[32] H. Steinwedel e J.H.D. Jensen, *Z. Naturforsch* **5A**, (1950) 413

[33] A. Bohr, B. Mottelson, "*Nuclear structure*", Benjamin, New York (1975)

[34] M. Goldhaber e E. Teller, *Phys. Rev.* **74**, (1948) 1046

[35] W.D. Myers, W.J. Swiatecki et al., *Phys. Rev.* **C15**, (1977) 2032

[36] S.G Nilsson, I. Ragnarsson "Shapes and Shells in Nuclear Structure", Cambridge University Press

[37] R.A. Broglia et al.,*Prog. Part. Nucl. Phys.* **28**, (1992) 517

[38] Y. Alhassid et al., *Nucl. Phys.* **A469**, (1987) 205

[39] M. Danos, *Nucl. Phys.* **5**, (1958) 23

[40] J. Wambach, *Contemporary Phys.* **32**, (1991) 291

[41] L. Landau, *Sov. Phys. JETP* **3**, (1956) 920

[42] B.L. Berman et al., *Rev. Mod. Phys.* **47**, (1975) 713

[43] Y. Alhassid and B. Bush, *Nucl. Phys.* **A509**, (1990) 461

[44] Y. Alhassid and B. Bush, *Nucl. Phys.* **A531**, (1991) 1

[45] G.F. Bertsch et al., *Rev. Mod. Phys.* **55**, (1983) 287

[46] P. Ring e P. Schuck, "The Nuclear Many–Body Problem", Springer–Verlag

[47] D.M. Brink, *Nucl. Phys.* **4**, (1957) 215

[48] P.Axel, *Phys. Rev.* **126**, (1962) 671

[49] F.S. Dietrich et al., *Phys. Rev.* **C10**,(1974) 795

[50] J.O. Newton et al., *Phys. Rev. Lett.* **46**, (1981) 1383

[51] H. Sagawa e G.F. Bertsch, *Phys. Lett.* **B146**, (1984) 138

[52] M. Barranco et al., *Phys. Lett.* **B154**, (1985) 96

[53] E. Lipparini e S. Stringari, *Nucl. Phys.* **A482**, (1988) 205c

[54] F. Garcias et al., *Z. Phys. A-Atomic Nuclei* **337**, (1990) 261

[55] D. Pierroutsakou et al., *Nucl. Phys.* **A600**, (1996) 131

[56] J.J. Gaardh$\oslash$je et al., *Phys. Rev. Lett.* **56**, (1986) 1783

[57] F. Puhlhofer, *Nucl. Phys.* **A280**, (1977) 267; M. N. Harakeh extended version (private communication)

[58] D.R. Chakrabarty et al., *Phys. Rev.* **C36**, (1987) 1886

[59] A. Bracco et al., *Phys. Rev. Lett.* **62**, (1989) 2080

[60] A. Bracco et al., *Phys. Rev. Lett.* **74**, (1995) 3748

[61] P.F. Bortignon et al., *Nucl. Phys.* **A460**, (1986) 149

[62] P.F. Bortignon et al., *Nucl. Phys.* **A495**, (1989) 155c

[63] P.F. Bortignon et al., *Phys. Rev. Lett.* **67**, (1991) 3360

[64] F.V. De Blasio et al., *Phys. Rev. Lett.* **68**, (1992) 1663

[65] M. Gallardo et al., *Nucl. Phys.* **A443**, (1985) 415

[66] A. Smerzi et al., *Phys. Rev.* **C44**, (1991) 1713

[67] A. Smerzi et al., *Phys. Lett.* **B320**, (1994) 216

[68] E. Ramakrishnan et al., *Phys. Rev. Lett.* **76**, (1996) 20254

[69] A. Bracco et al., *Nucl. Phys.* **A519**, (1990) 47c

[70] J.J. Gaardh∅je, *Nucl. Phys.* **A488**, (1988) 261c

[71] D. Kusnezov et al, *Phys. Rev. Lett.* **81**, (1998) 542

[72] J.J. Gaardh∅je et al., *Phys. Rev. Lett.* **59**, (1987) 1409

[73] J. Kasagi et al., *Nucl. Phys.* **A538**, (1992) 585c

[74] J. Kasagi e K. Yoshida, *Nucl. Phys.* **A569**, (1994) 195c

[75] T. Suomijärvi et al., *Phys. Rev.* **C53**, (1996) 2258

[76] Ph. Chomaz, *Nucl. Phys.* **A569**, (1994) 203c

[77] Ph. Chomaz, *Phys. Lett.* **B347**, (1995) 1

[78] Y. Alhassid and B. Bush, *Phys. Rev. Lett.* **65**, (1990) 2527

[79] V. Butsch et al., *Phys. Rev.* **C41** , (1990) 1530

[80] J.M. Lattimer, M. Prakash, *Phys. Rep.* **442** (2007), 109

[81] R. Brun et al., *CERN Report No. CERN-DD/EE/84-1* (unpublished, 1986)

[82] W.J. Swiatecki, *Phys. Scr.* **24**, (1981) 113

[83] M. Thoennessen et al., *Phys. Rev. Lett.* **70**, (1993) 4055

[84] M. Thoennessen et al., *Phys. Rev.* **C51**, (1995) 3148

[85] S. Hofmann, G. Mnzenberg, *Rev. Mod. Phys.* **72**, (2000) 733

[86] K. Morita et al., *J. Phys. Soc. Jpn.* **76**, (2007) 043201

[87] Y.T. Oganessian et al., *Phys. Rev.* **C74**, (2006) 044602

[88] S. Hofmann et al., *Eur. Phys. J.* **A32**, (2007) 251

[89] C. Simenel et al., *Phys. Rev.* **C76**, (2007) 024609

[90] Y. Aritomo, T. Wada, M. Ohta, and Y. Abe, *Phys. Rev.* **C59**, (1999) 796

[91] A. Gavron. *Phys. Rev.* **C21**, (1980) 230

[92] W.R. Leo, "Techniques for Nuclear and Particle Physics Experiments", Springer–Verlag

[93] G.F. Knoll, "Radiation Detection and Measurement", 2^{nd} edit., J. Wiley&Sons

[94] D.H. Perkins, "Introduction to High Energy Physics", Addison – Wesley

[95] M.P. Kelly et al., *Phys. Rev. Lett.* **82**, (1999) 3404

[96] E. Migneco et al., *Nucl. Instr. and Meth. in Phys. Res.* **A314**, (1992) 31

[97] R. Brun et al., *Nucl. Phys.* **A389**, (1997) 81; see also http://root.cern.ch.

[98] A. Del Zoppo et al., *Nucl. Instr. and Meth. in Phys. Res.* **A327**, (1993) 363

[99] T. Matulewicz et al., *Nucl. Instr. and Meth.* **A274**, (1989) 501

[100] D.Bazin, M.Lewitowicz, O.Sorlin, O.Tarasov, *Nucl. Instr. and Meth.* **A482**, (2002) 314

[101] M.P. Kelly et al., *Phys. Rev.* **C56**, (1997) 3201

[102] E. Holub et al., *Phys. Rev.* **C28**, (1983) 252

[103] R. Alba et al., *Phys. Lett.* **B322**, (1994) 38

[104] H. Nifenecker e J.A. Pinston, *Annu. Rev. Nucl. Part. Sci.* **40**, (1990) 113

[105] R. Ortega, D. dEnterria, G. Martinez, *Eur. Phys. J.* **A28**, (2006) 161

[106] B.A. Remington et al., *Phys. Rev. Lett.* **57**, (1986) 2909

[107] R. Heuer et al., *Z. Phys.* **A330**, (1988) 315

[108] R.J. Vojtech et al., *Phys. Rev.* **C40**, (1989) R2441

[109] G. Bellia et al., *Nucl. Instr. and Meth. in Phys. Res.* **A329**, (1993) 173

[110] M. E. Rose, *Phys. Rev.* **91**, 610 (1953)

[111] M. Tsang et al., *Phys. Rev. Lett.* **52**, (1984) 1907

[112] M. Tsang et al., *Phys. Rev.* **C42**, (1990) R15

[113] M. Tsang et al., *Phys. Rev.* **C44**, (1991) 2065

[114] D. Prindle et al., *Phys. Rev.* **C48**, (1993) 291

[115] Th. Keutgen et al., *Phys. Rev.* **C70**, (2004) 014611

[116] V.E. Viola, K. Kwiatkowski and M. Walker, *Phys. Rev.* **C31**, (1985) 1550

[117] W. Q. Shen et al., *Phys. Rev.* **C36**, (1987) 115

[118] J. Tōke et al., *Nucl. Phys.* **A440**, (1985) 317-365

[119] T. Papenbrock and G.F. Bertsch, *Phys. Rev. Lett.* **80**, (1998) 4141

[120] V. Baran, M. Colonna, V.Greco, M. Di Toro, *Phys. Rep.* **410**, (2005) 335

[121] Bao-An Li, Lie-Wen Chen, Che Ming Ko, *Phys. Rep.* **464**, (2008) 113

[122] M. Di Toro, M. Colonna, C. Rizzo, V. Baran, *Int. Jour. Mod. Phys.* **E17**, (2009) 110